Kristianne Nilsen-Nygaard Hjelseng

Chemical and morphological insights on the initial lithiation and delithiation of SiO$_2$ anodes for Lithium-ion Batteries

Master's thesis in Chemical Engineering and Biotechnology
Supervisor: Maria Valeria Blanco
Co-supervisor: Weicheng Hua, Ann Mari Svensson
June 2023

NTNU
Norwegian University of
Science and Technology

Kristianne Nilsen-Nygaard Hjelseng

Chemical and morphological insights on the initial lithiation and delithiation of SiO$_2$ anodes for Lithium-ion Batteries

NTNU
Norwegian University of
Science and Technology

Preface

This thesis describes the work carried out in the course TMT4900 Materials Chemistry and Energy Technology, written at the Norwegian University of Science and Technology (NTNU), Department of Material Science and Engineering, during the spring of 2023. The work has been supervised by Adj. Assoc. Professor Maria Valeria Blanco as the main supervisor, and PhD candidate Weicheng Hua and Professor Ann Mari Svensson as co-supervisors. I hereby declare that this project has been done independently and in accordance with the regulations at NTNU.

Some of this work resembles the work the author conducted during the fall of 2022 in the specialisation project "Improving the performance algae-derived SiO_2 anodes by optimizing electrode/electrolyte interphase". Specifically, the theory Section 2 shares many similarities. The data presented in Section 4.3.1 is from a cell made during the specialisation project, that was still cycling when this thesis was conducted [1].

PhD candidate Weicheng Hua conducted the electrolyte preparation. The XPS measurements were made by Jakob Vinje, Senior Engineer at NTNU NanoLab. Except for this, all the experiments and analyses described in this thesis were executed by the author of this master thesis.

Acknowledgements

Lastly, I want to express my gratitude to my boyfriend, Thomas, for his unwavering support, love, and patience throughout this journey. I would also like to thank my friends and family for being by my side, sharing the highs and lows of this final year.

Abstract

Lithium-ion batteries (LIBs) dominate the battery market of portable electronics and have a widespread application in the booming market of automotive and stationary energy storage. The state-of-the-art cathode materials for high-energy LIB cells are the layered lithium nickel cobalt manganese oxides, while graphite is still the state-of-the-art anode material. However, in view of the growing energy demand for energy storage, higher energy-density electrode materials are required.

In the last years, SiO_2 has attracted a lot of interest as an anode candidate for LIBs. SiO_2 has a favourable high theoretical capacity (1965 mAhg^{-1}) compared to graphite (372 mAhg^{-1}) and, unlike graphite, it can be extracted from sustainable sources. However, the dynamics of the chemical reactions occurring during SiO_2 lithiation and delithiation, especially during initial electrochemical cycling, is complex and not fully understood, and this hinders the development of improved SiO_2 anodes that can outperform state-of-the-art negative electrodes.

This project aims to investigate chemical and morphological changes in SiO_2 anodes produced from diatomaceous earth, which is a sustainable source for nanostructured SiO_2, during early lithiation and delithiation stages. For this, SiO_2 electrodes were fabricated and cycled to selected potentials upon lithiation and delithiation. Depth profile of chemical compositions at the selected potentials was determined by X-ray photoelectron spectroscopy (XPS, 1486.6 eV) coupled with Ar$^+$ ion sputtering. Morphological analysis of the electrodes performed by focused ion beam and scanning electron microscopy (FIB/SEM) allowed to evaluate microstructural changes upon lithiation and delithiation.

Anodes containing ball-milled amorphous diatomaceous earth SiO_2 as active material, carbon black as a conductive additive and water-soluble Na-alginate binder were assembled in half-cells using lithium hexafluorophosphate as an electrolyte salt, fluoroethylene carbonate as an electrolyte additive, and Lithium foil as the counter electrode. Cells were initially cycled between 2 V (Li$^+$/Li) and 0.002 V (Li$^+$/Li) at 50 mAg^{-1}, and the potential was held for 48 h

and 24 h after each lithiation and delithiation cycle, respectively. In the initial 4 cycles, half-cells show a marked increase of SiO$_2$ reaction towards Li-ions, and the capacity increases cycle after cycle until reaching a stable value of 1172 mAhg^{-1}. Therefore, these initial 4 cycles are called "activation cycles". Importantly, cells showed a specific capacity of about 1000 mAhg^{-1} after 200 cycles, hence retaining most of the initial capacity value. XPS depth profile analysis showed a slow reaction of SiO$_2$ with Li-ions to produce lithium silicates, lithium oxide and electroactive silicon during the two initial cycles, and it was demonstrated that at cycle number 4, all the SiO$_2$ was converted to lithium silicates and silicon, therefore proving that the "activation cycles" constitute an essential step to make full use of the SiO$_2$. Depth profile analysis also revealed that lithium silicates are formed at the outer layer of the SiO$_2$ particles, which corroborates previous findings of other authors. FIB/SEM cross-section results showed significant porosity loss after the first lithiation cycle, and crack formation at the electrode level after the first delithiation.

Further research should extend the present voltage-dependent XPS analysis to high-resolution transmission electron microscopy (HR-TEM) and atom probe tomography (APT) investigations to determine the spatial distribution of SiO$_2$ reaction products upon lithiation/delithiation reactions with the aim of gaining a full understanding of the role of lithium silicates, lithium oxide and silicon on the electrode specific capacity and stability.

Sammendrag

Litium-ion batterier (LIB-er) dominerer batterimarkedet for bærbare elektroniske enheter og har en utbredt anvendelse i det voksende markedet for bilindustrien og stasjonær energilagring. De mest vanlige katodematerialene for LIB-celler med høy energitetthet er litiumnikkelkoboltmanganoksyder, mens grafitt er fortsatt det mest vanlige anodematerialet. Men med tanke på den økende etterspørselen for energilagring, er det behov for elektrodematerialer med høyere energitetthet.

De siste årene har SiO_2 vekket stor interesse som en mulig anode for LIB-er. SiO_2 har en høy teoretisk kapasitet (1965 mAhg^{-1}) sammenlignet med grafitt (372 mAhg^{-1}) og kan, i motsetning til grafitt, utvinnes fra bærekraftige kilder. Imidlertid er dynamikken i de kjemiske reaksjonene som oppstår under litiering og delitiering av SiO_2, spesielt i begynnelsen av elektrokjemiske sykluser, kompleks og er ikke fullstendig forstått. Dette hindrer utviklingen av forbedrede SiO_2-anoder.

Formålet med denne oppgave har vært å undersøke kjemiske og morfologiske endringer i SiO_2-anoder laget av kiselalger, som er en bærekraftig kilde av nanostrukturert SiO_2, i løpet av tidlig litiering og delitiering. For å undersøke dette ble SiO_2-elektroder produsert og syklet til utvalgte potensialer under litiering og delitiering. Dybdeprofilene for kjemisk sammensetning ved de valgte potensialene ble bestemt ved bruk av røntgen fotoelektron spektroskopi (XPS, 1486.6 eV) kombinert med Ar$^+$-ion sputtring. Morfologisk analyse av elektrodene utført ved hjelp av fokusert ionestråle og skanning elektronmikroskop (FIB/SEM) gjorde det mulig å evaluere mikrostrukturelle endringer ved litiering og delitiering.

Anoder av kulemalte kiselalger SiO_2, som aktivt materiale, karbon svart som en ledende tilsetning og vannløselig Na-alginatbindemiddel ble montert i halvcelle konfigurasjon ved hjelp av litiumheksafluorfosfat som elektrolyttsalt, fluoretylenkarbonat som elektrolytttilsetning, og litiumfolie som mot-elektrode. Cellene ble først syklet mellom 2 V (Li$^+$/Li) og 0.002 V (Li$^+$/Li) ved 50 mAg^{-1}, og potensialet ble holdt i 48 timer og 24 timer etter hver litierings-

og delitieringssyklus, henholdsvis. I de første 4 syklusene viser halvcellene en økning av SiO$_2$-reaksjonen med Li-ioner, og kapasiteten øker syklus etter syklus til den når en stabil verdi på 1172 mAhg^{-1}. Derfor kalles disse første 4 syklusene "aktiveringssykluser". Knappecellene har en spesifikk kapasitet på omtrent 1000 mAhg^{-1} etter 200 sykluser og beholdt dermed mesteparten av den opprinnelige kapasiteten. XPS-dybdeprofilanalysen viste en langsom reaksjon av SiO$_2$ med Li-ioner for å danne litiumsilikater, litiumoksid og elektroaktivt silisium i løpet av de to første syklusene. Det ble også vist at ved syklus nummer 4 ble all SiO$_2$ konvertert til litiumsilikater og silisium, noe som beviser at "aktiveringssyklusene" utgjør et essensielt trinn for å utnytte SiO$_2$ fullt ut. Dybdeprofilanalysen viste også at litiumsilikater dannes på utsiden av SiO$_2$-partiklene, noe som bekrefter tidligere funn fra andre forfattere. Resultatene fra FIB/SEM viste betydelig tap av porøsitet etter den første litieringssyklusen og sprekkdannelse på elektroden etter den første delitieringen.

Videre forskning bør utvide den nåværende spenningsavhengige XPS-analysen til undersøkelser med høyoppløsnings transmisjons elektron mikroskopi (HR-TEM) og atom sonde tomografi (APT) for å bestemme den romlige distribusjonen av SiO$_2$-reaksjonsprodukter ved litierings- og delitieringsreaksjoner med mål om å oppnå en fullstendig forståelse av rollen til litiumsilikater, litiumoksid og silisium på elektrodens spesifikke kapasitet og stabilitet.

Acronyms

AM Active material. 35, 37, 75

BSE Backscattered electrons. 29

CB Carbon black. 16, 35, 52, 75

CE Coulombic efficiency. 9, 15, 21, 81

CE Counter electrode. 36

CV Cylic voltammetry. xxi, 31, 38, 39, 43, 47, 49, 82, 108

DC Differential capacity. xxi, 31, 38, 39, 46, 49, 81, 86, 108

DE Diatomaceous earth. 16

DEC Diethyl carbonate. 19

DFT Density-functional theory. 3, 14

DI water Deionised water. 34, 35

DMC Dimethyl carbonate. 19, 39, 87

EC Ethylene carbonate. 19

EMC Ethyl methyl carbonate. 19

FEC Fluoroethylene carbonate. 21

FIB Focus ion beam. vii, 29, 41, 43, 92

HAXPES Hard X-ray photoelectron spectroscopy. 28, 68, 91, 93

HF Hydrofluoric acid. 20

HOMO Highest occupied molecular orbital. 18

LIB Lithium-ion battery. vii, 2, 5, 12, 18, 20, 30, 86

LiBF$_4$ Lithium tetrafluoroborate. 20

LiFSI Lithium bis(fluorosulfonyl)imide. 20

LiPF$_6$ Lithium hexafluorophosphate. 20

LUMO Lowest unoccupied molecular orbital. 18

M molarity. 36

NTNU Norwegian University of Science and Technology. iii

OCV Open circuit voltage. 7, 38

PC Propylene carbonate. 19

PHS Pumped hydro storage. 2

ppm parts per million. 37

PSD Particle size distribution. xix, 34, 45

rpm revolutions per minute. 33, 35

SE Secondary electrons. 29

SEI Solid electrolyte interphase. 2, 15, 17, 21, 23, 73, 83, 91

SEM Scanning electron microscopy. vii, 41, 43, 90, 92

VC Vinylene carbonate. 21

Contents

Figures

Tables

Chapter 1

Introduction

1.1 Background and motivation

Population growth and vast technological development result in huge energy consumption. Indeed, the demand for energy at the global level is predicted to increase 30% by 2035 due to a rapid increase in population and economic growth [2]. Most of this energy comes from fossil fuels that are both limited in resources and emit large amounts of greenhouse gasses. Hence, there is an imperious need to develop green energy strategies for a sustainable future without any negative environmental and societal impacts. Green energy can be defined as the energy source, which has zero or minimal environmental impact, as more environmentally benign and more sustainable, and is produced from solar, hydro, biomass, wind, geothermal, etc. This type of green energy reduces the negative effects of fossil energy resources and the overall emission from electricity generation [3]. Therefore the motivation to develop renewable energies has never been so important and the goal is the transfer from fossil fuels towards renewable sources of energy.

Although renewable energy sources are environmentally friendly and sustainable, they have one major drawback, as they cannot consistently produce energy throughout the day or year. This is where energy storage becomes crucial. Energy storage systems allow surplus energy to be stored when renewable sources are producing excess energy and then release it when demand exceeds supply. Energy storage enhances the efficiency of energy systems by balancing power grids and saving surplus energy, which enables the integration of more renewable energy sources into electricity systems. Additionally, energy storage also helps to ensure a stable and reliable supply of electricity, making it an essential component of a sus-

tainable and safe energy future. Although the EU's main energy storage reservoir is pumped hydro storage (PHS), the number of projects involving batteries is growing, and lithium-ion batteries (LIBs) represent most of the electrochemical storage projects [4].

LIB technology has dominated the rechargeable battery market since its first commercialisation in 1991 [5]. This is due to the higher gravimetric and volumetric energy densities it can offer in comparison to other rechargeable systems like Ni-Cd and lead-acid [6]. However, for the next-generation batteries, there is a need to increase the energy density and decrease the cost, while not increasing the size of the device. Other essential aspects are the sustainability and non-toxic character of the material used to produce battery components. Indeed, the magnitude of the forthcoming market demand for LIBs makes the sustainable supply of non-toxic and high-performance battery components an essential need.

Today, the commercial anode material in LIB is graphite, with a limited theoretical capacity of 372 mAhg^{-1} [6]. There are two types of graphite used in state-of-the-art LIBs, natural graphite (NG) and synthetic graphite (SG) [7]. SG is produced by heating unsaturated carbon often derived from petroleum, and using a coke-based precursor, giving a higher purity and thermal stability than NG. NG is extracted from the Earth´s crust through mining processes. Both graphite types need to undergo a high temperature (>3000°C) graphitisation step that requires substantial energy consumption [7]. As a consequence, the production of NG and SG has a wide range of environmental impacts, the mining of the NG can cause dust emission, whereas the purification process for battery-grade anodes requires high quantities of reagents including hydrofluoric acid and sodium hydroxide. These reagents can be harmful to both the environment and human health. Also, the high energy demand during heating leads to the usage of the cheapest power sources like coal and oil, which generates a higher overall carbon footprint. Additionally, its low lithium storage capacity cannot satisfy the requirements of electric vehicles and electronic devices for the battery.

A number of materials with higher theoretical capacity have therefore been investigated for the next-generation LIB anode. Silicon (Si) has a theoretical capacity of 3590 mAhg^{-1} (for the Li$_{15}$Si$_4$ phase at room temperature), which is about ten times higher than for graphite material [8]. Nevertheless, practical applications of silicon anodes are hindered by the huge volume change of 300% during lithiation and delithiation. The large volume change results in particle pulverisation that makes the solid electrolyte interphase (SEI) crack and consequently, the electrolyte is consumed continuously. Therefore it has not been successfully commercialised yet.

Another option for next-generation LIBs is silica (SiO_2) as an anode material. This is due to its high abundance in the Earth's crust, high reversible capacity (1961 mAhg^{-1}) and low discharge potential [9]. The natural abundance of SiO_2 makes it highly suitable for large-scale commercial applications. Density-functional theory (DFT) calculations show that during electrochemical cycling, SiO_2 undergoes reversible and irreversible reactions, that lead to the generation of Si, as well as $Li_2Si_2O_5$, Li_2SiO_3, Li_4SiO_4 and Li_2O [10]. It has been hypothesised that upon further cycling, it is the Si that reacts reversibly and contributes towards the majority of the reversible capacity. While, the other product would provide structural support to the anode, by serving as a buffer and mitigating the huge volume expansion in the Si lithiation/delithiation process. As a result, the SiO_2 anode cycling lifetime is prolonged compared to the Si anode. However, the proposed lithiation and delithiation reactions of SiO_2 have not been clearly evidenced experimentally. The main reason for this is that SiO_2 electrochemical cycling involves the occurrence of multiple reactions and leads to the production of low amounts of several short-range ordering reaction products, which are not possible to detect by standard laboratory techniques, such as X-ray diffraction (XRD).

Interestingly, some hints of the SiO_2 lithiation/delithiation reactions can be observed from surface studies of Si anodes having a native SiO_2 layer at the outer surface of the particles [11]. Studies on Si nanowire anodes having a 1 to 3 nm SiO_2 layer at their surface were performed by X-ray photoelectron spectroscopy (XPS), which is a surface sensitive technique [12]. Results reported that SiO_2 signal disappears upon anode lithiation. Also, electrode morphology was found to display a voltage-dependent behaviour, in which a thick layer containing large particles is formed upon lithiation, and partially dissolves and forms cracks upon delithiation. Other studies have investigated the SEI by its evolution as a function of voltage, by stopping at specific potentials and analysing the chemical composition by XPS [13]. Ruffo et al. combined this technique with different sputtering times, creating an XPS depth profile of the SEI on silicon nanowire electrodes [14]. Thereby, these methods could also be used to give information about the SiO_2 lithiation and delithiation reactions as well as the formation of the SEI.

1.2   Aim of the work

The main goal of this work is to identify chemical changes in SiO_2 anodes during early lithiation and delithiation stages, together with microstructural changes occurring at the electrode

level. For this, SiO$_2$ electrodes were carefully lithiated and delithiated at selected potentials and a thorough XPS characterisation at different electrode depths was performed. A complementary analysis by FIB/SEM was performed to evaluate microstructural changes on the cycled electrodes. These results will provide valuable insights on the dynamics of chemical reactions occurring at the interface and the porosity changes occurring in the interior of the electrode, which will serve for the design of improved SiO$_2$-based negative electrodes.

Chapter 2

Theory

2.1   Lithium Ion Batteries

A battery is a device that converts chemical energy into electrical energy [15]. It consists of one or several electrochemical cells. An electrochemical cell consists of two electrodes, a negative (anode) and a positive (cathode) with a current collector, they are separated by a separator and an electrolyte solution that facilitates the flow of ions. When the cell is connected to an external circuit, the chemical reactions that occur inside the cell result in a flow of electrons, creating a potential difference between the electrodes and generating an electric current. Batteries are divided into primary and secondary cells [15]. Primary cells irreversibly transfer chemical energy into electrical energy, which means they are non-rechargeable. On the contrary, secondary cells are reversible and can be recharged. This means that the chemical reactions can be reversed by supplying electrical energy to the cell and the battery can be used again. A LIB is a secondary cell, and here the ion that is transferred back and forth between the anode and the cathode is lithium. The separator is placed between the anode and cathode as a physical barrier to prevent them from coming in contact and short-circuiting. The separator is a thin, porous membrane that allows the lithium-ions to go through during charge and discharge. The current collector is a conductive material, usually a metal that has the purpose of transferring electrons between the electrode and the external circuit. Aluminium and copper are normally used as current collector materials for the cathode and anode, respectively. A schematic of a LIB is shown in Fig. 2.1.
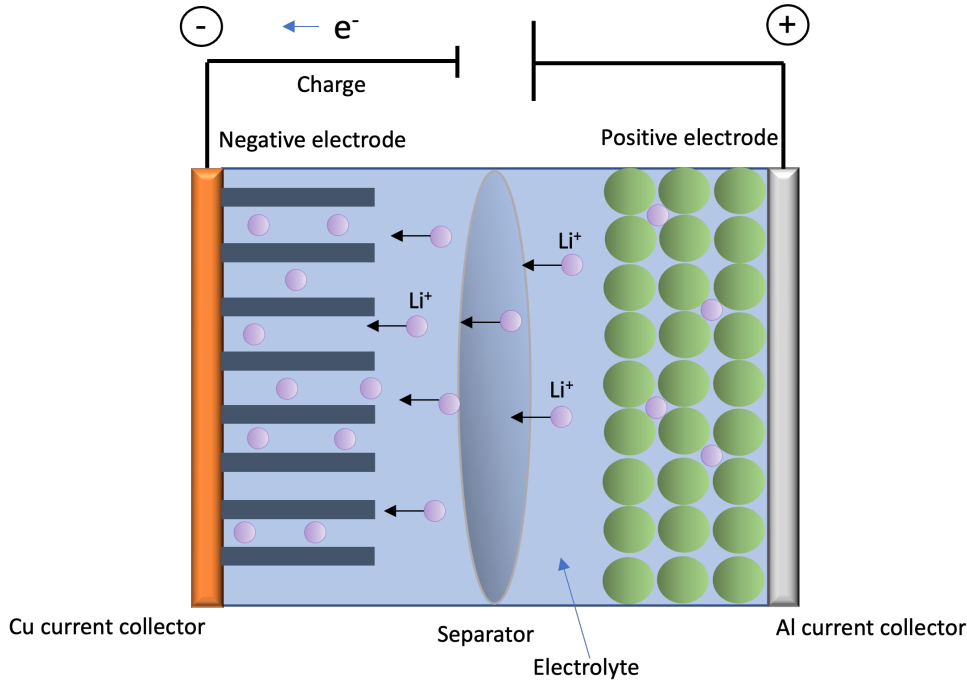
Figure 2.1: Schematic illustration of a LIB with a graphite anode. The directional flow of electrons and lithium-ions during charge is illustrated [1].

2.1.1 Principle of a secondary lithium-ion battery

A LIB contains charge carriers in the form of Li^+-ions. During the charging process, these ions move from the cathode to the anode through an electrolyte that is both electronically isolating and ion-conducting. Conversely, during discharge, the lithium ions flow in the opposite direction, from the anode to the cathode. The incorporation of lithium into an electrode is termed lithiation, and the removal of lithium from an electrode is termed delithiation.

For a LIB with a graphite anode and a $LiCoO_2$ cathode, the electrochemical reaction can be expressed as follows, taking into account the charge and discharge reactions:

Anode:

$$6C + xLi^+ + xe^- + \; \rightleftharpoons Li_xC_6 \tag{2.1.1}$$

Cathode:

$$LiCoO_2 \rightleftharpoons Li_{1-x}CoO_2 + xLi^+ + xe^- \tag{2.1.2}$$

The total reaction is:

$$LiCoO_2 + 6\,C \underset{Discharge}{\overset{Charge}{\rightleftharpoons}} Li_{1-x}CoO_2 + Li_xC_6 \tag{2.1.3}$$
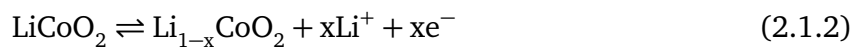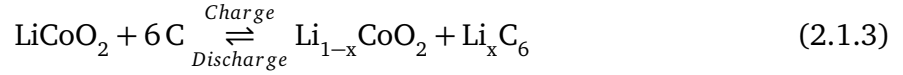
During discharge, at the anode, the oxidation reaction takes place, and this oxidation entails the release of x electrons through the outer circuit and x lithium-ions. Here, x is in the range of 0 and 1. At the cathode a reduction reaction occurs, capturing x electrons released from the anode and reducing the lithium-ions to $LiCoO_2$.

2.2   Battery terminology

Cell voltage (V)

Cell voltage, V, is defined as the potential difference between the two electrodes. When no net current is applied, this voltage is referred to as the open circuit voltage (OCV).

The OCV, V_{OC}, of a cell is therefore defined by the difference between the electrochemical potentials μ_C and μ_A of the cathode and anode [16]:

$$V_{OC} = \frac{(\mu_A - \mu_C)}{e}, \tag{2.2.1}$$

where e is the electron charge (1.602×10^{-19} C).

Capacity (Q)

The capacity, Q, of a battery is a measure of the total amount of charge that can be stored in the cell [16], and is given by the equation:

$$Q(I) = \int_0^{\Delta t} I\,dt = \int_0^Q dq, \tag{2.2.2}$$

where I is the current (Ampere) applied through the battery, t is the time (seconds) while the current is delivered, and Q is the capacity (Coulomb). It is more common to refer to capacity in Amphere-hours (Ah) ($1Ah = 3600C$).

The theoretical capacity, Q_{th} of an electrode can be calculated by the equation:

$$Q_{th} = \frac{nF}{M_w},$$
(2.2.3)

where n is the number of transferred electrons, F is the Faraday´s constant (96485 Asmol^{-1}) and M_w is the molecular weight (gmol^{-1}) of the active material [17].

Energy (W)

The total amount of energy, W, given in Watts hour, in a fully charged cell is given by the relation [16]:

$$W = \int_0^{\Delta t} IV(t)\,dt = \int_0^Q V(q)\,dq,$$
(2.2.4)

here, V is the cell voltage (Volt), t is the time (seconds), I is the current applied through the battery (C/Ah) and Q is the capacity (A). The energy is usually given in energy density (Whdm^{-3}) or in specific energy (Whg^{-1}).

Energy density

The amount of energy stored in a battery, W, is given by eq. (2.2.4). However, energy density describes the amount of energy stored in a battery per volume or mass. Thus the amount of energy per litre (WhL^{-1}), also called the volumetric energy density, is described by the equation:

$$\text{Volumetric energy density} = \frac{W}{vol}$$
(2.2.5)

And the amount of energy per mass (Whkg^{-1}), also called the gravimetric energy density is given by the equation:

$$\text{Gravimetric energy density} = \frac{W}{wt}$$
(2.2.6)

Power (P)

The power output of the battery, P_{out}, describes how fast the battery delivers Li-ions and electrons, therefore the power is dependent on the kinetics of the redox reaction. The power is defined by the equation:

$$P_{out} = V_{dis}I_{dis},\tag{2.2.7}$$

where V_{dis} is the voltage given by eq. (2.2.8) and I_{dis} is the electrical current delivered by the battery during discharge [15]. The power is usually given in power density (Wdm^{-3}) or specific power (Wkg^{-1}).

When the battery is discharged, an internal resistance in the battery, R_b to the ionic current $I_i = I$ lowers the output voltage V_{dis} from the V_{OC} by a polarisation $\eta = I_{dis}R_b$. But when the battery is charged the resistance increases the voltage to charge the battery V_{ch} by an overvoltage of $\eta = I_{ch}R_b$ [16]. This gives the equations below:

$$V_{dis} = V_{OC} - I_{dis}R_b\tag{2.2.8}$$

$$V_{ch} = V_{OC} + I_{ch}R_b\tag{2.2.9}$$

Battery lifetime and battery efficiency

The cycle life of a battery is commonly defined as the number of cycles a cell can perform until its capacity drops to 80% of its initial capacity [18]. The coulombic efficiency (CE) is a measure of the irreversible loss of lithium inventory and is given by the charge capacity over the discharge capacity:

$$CE = 100 \cdot \frac{Q_{dis}}{Q_{ch}}\tag{2.2.10}$$

C-rate

The C-rate is used to express the charge or discharge current in order to normalise the data against the capacity that depends on the battery [15]. A charge of *nC* rate means a full charge in 1/n hours. Therefore 1C means that the battery is fully charged in 1 hour. If the battery has a capacity of 50 Ah, this gives a charge current of 50 A.

2.3   Cell components

A battery consists of two electrodes (anode and cathode) and an electrolyte. In this thesis, half-cells were composed of an SiO$_2$ anode and lithium metal as the counter electrode. The different cell components for the half-cells will be discussed in this section.

2.3.1   Anode materials

The negative electrode also called anode has a set of requirements it should fulfil [15];

1. It must be light and accommodate as much lithium as possible to optimise the gravimetric capacity.
2. Its redox potential with respect to Li$^+$/Li must be as low as possible at any Li-concentration. The reason is that this potential is subtracted from the redox potential of the cathode material to give the overall voltage of the cell (eq. 2.2.1), and lower cell voltage means lower energy (eq. 2.2.4).
3. It must possess good electronic and ionic conductivities since the faster motion of lithium ions and electrons provides a higher power density to the cell.
4. It must not be soluble in the solvents of the electrolyte and not react with the lithium salt.
5. It must be safe, i.e. avoid any thermal runaway of the battery, a criterion that is not independent of the previous one but deserves special attention. This is especially important for transportation such as electric vehicles and planes.
6. It must be cheap and environmentally friendly.

Anode materials are classified according to their lithiation/delithiation mechanisms. The classifications are intercalation, alloying and conversion anodes. The different types will be discussed below.

Intercalation anodes

Intercalation anodes involve the insertion of a guest ion/molecule, e.g. Li^+ into a host lattice without altering the basic structure of the host lattice [15]. This means that these anodes do not experience a huge volume expansion when the lithium enters the electrode. The most common intercalation anode material is graphite, and here the lithium is reversibly intercalated between the graphite layers [19]. The reversible lithiation reaction with graphite is given by:

$$C_6 + Li^+ + e^- \rightleftharpoons LiC_6 \tag{2.3.1}$$

This reaction has a maximum reversible theoretical specific capacity of 372 mAhg^{-1} [20]. Graphite has a low insertion voltage ($\sim$ 0.2-0.05 V vs Li^+/Li), and good Li-ion and electrical conductivity. The material is cheap, non-toxic and abundant in nature. It is because of these properties that graphite is still widely used in current devices.

Conversion anodes

The second type of negative electrode material is referred to as conversion anode and it contains a transition metal, TM, coupled with an anion, X [21]. The conversion mechanism has the general reaction:

$$TM_yX + nLi^+ + ne^- \rightleftharpoons yTM + Li_nX, \tag{2.3.2}$$
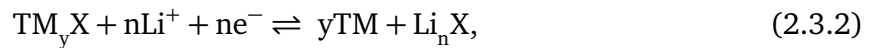
where n is the formal oxidation state of X. Examples of TM are Fe, Mn, Ni, Co and Cu and examples of X are O, S and P. In this type of anode, lithium is stored with high specific capacity through a reversible redox reaction between Li^+ and transition-metal cations.

Alloying anodes

The last type of anode is based on the alloying reaction between lithium and the anode material:

$$M + xLi^+ + xe^- \rightleftharpoons Li_xM \tag{2.3.3}$$

where typical examples of M are Si, Ge, Sn, Pb, Bi, Sb, As and P [22]. Generally, these materials have much higher Li-ion storage capacity than intercalation anodes. However, the

practical use of these alloying anodes has been hindered by the huge volume change during alloying/de-alloying process. The resulting large strain can lead to electrode pulverisation and capacity loss during cycling [19].

2.3.2   Si anodes

As mentioned above, Si is an alloying anode and has been intensively studied as one of the most promising materials for high-energy LIBs for replacing state-of-the-art graphite anodes. When looking at the requirements for a good negative electrode material mentioned in Section 2.3.1 it fulfils most of them [23]:

1. High gravometric capacity of 4200 mAhg^{-1} for Li$_{4.4}$Si, which is 10 times higher than for graphite.
2. The redox potential is low (~ 0.4 V vs Li$^+$/Li).
3. Second most abundant element in the crust of the earth, non-toxic and eco-friendly.

Lithiation mechanism of Si

The lithiation mechanism between Si and Li$^+$ is not fully understood, even though the research on this anode material for LIB has been popular. A number of Li$_x$Si compounds have been identified during lithiation, and their formation depends on both cycling speed and lithiation cut-off potential [24]. An overview of a proposed reaction mechanism by Ogata et al. is found in Table 2.1.

Challenges of Si anodes

Si as an anode material has some challenges like huge volume expansion ($\sim 300\%$) during lithiation/delithiation, which induces large stresses on the Si lattice. This leads to crack formation and particle pulverisation, which causes significant capacity fade on the anode due to electrode collapse [23]. Additionally, the prime Si source in the Earth´s crust is crystalline silica SiO$_2$ (quartz), and to gain pure grade Si, a chemical or thermal reduction is necessary. These methods require a lot of energy and cost [25]. A more economical and environmentally friendly alternative could therefore be SiO$_2$ instead as the anode material.

Table 2.1: Lithiation and delithiation mechanism of Si [24]. Amorphous and crystalline phase are denoted by a and c, respectively. The over-lithiated phase is described by δ (in the range 0.2 - 0.3).

Cycle/Stage	Reaction	Potential [V]
1$^{\text{st}}$ lithiation		
	$c-Si \rightarrow a-Li_xSi \rightarrow c-Li_{3.75}Si \rightarrow c-Li_{3.75+\delta}Si$	0.10
$\geq$ 2$^{\text{nd}}$ lithiation		
2	$a-Si \rightarrow a-Li_{2.0}Si$	0.30-0.25
3	$a-Li_{2.0}Si \rightarrow a-Li_{3.5}Si$	0.10
4	$a-Li_{3.75}Si \rightarrow c-Li_{3.5}Si$	0.05
5	$c-Li_{3.75}Si \rightarrow c-Li_{3.5+\delta}Si$	0.03
Delithiation		
1	$c-Li_{3.5+\delta}Si \rightarrow c-Li_{3.5}Si + c-Li_{3.5-\delta}Si$	0.05-0.15
2	$a-Li_{3.5}Si \rightarrow a-Li_{2.0}Si$	0.27
3	$c-Li_{3.5}Si \rightarrow a-Li_{1.1}Si$	0.43
4	$a-Li_{2.0}Si \rightarrow a-Si$	0.50

2.3.3 SiO$_2$ anodes

SiO$_2$ is proposed as a promising active material for LIBs negative electrodes, due to its high abundance and high reversible capacity (1961 mAhg^{-1}) [9]. Interestingly, SiO$_2$ reaction with Li-ions would result in the formation of different chemical species, such as silicon, lithium silicates and lithium oxide. The lithiation storage mechanism in SiO$_2$ is not clarified yet, but according to the literature, the electrochemical reactions that can take place are [26][27][10]:

$$5SiO_2 + 4Li^+ + 4e^- \rightleftharpoons 2Li_2Si_2O_5 + Si \qquad (2.3.4)$$

$$3SiO_2 + 4Li^+ + 4e^- \rightarrow 2Li_2SiO_3 + Si \qquad (2.3.5)$$

$$2SiO_2 + 4Li^+ + 4e^- \rightarrow Li_4SiO_4 + Si \qquad (2.3.6)$$

$$SiO_2 + 4Li^+ + 4e^- \rightarrow 2Li_2O + Si \qquad (2.3.7)$$
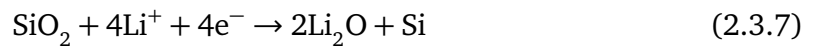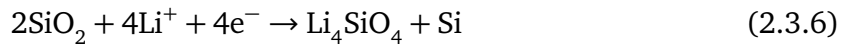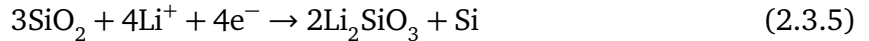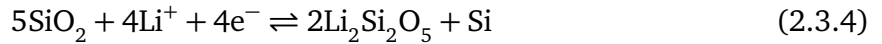
Upon further cycling, it is the Si that reacts reversibly and contributes to the majority of the reversible capacity. While the formation of Li$_2$Si$_2$O$_5$, Li$_4$SiO$_4$, Li$_2$SiO$_3$ and Li$_2$O species, most of which are thought to be electrochemically inert towards Li-ions, would provide structural support to the anode by mitigating the volume expansion of electroactive Si domains

upon lithiation/delithiation processes [10]. This makes SiO$_2$ a promising material to develop anodes with higher cycling stability compared to Si.

Lithiation potentials of SiO$_2$

Density-functional theory (DFT) calculations can be used to predict lithiation potentials for the products formed during lithiation of SiO$_2$. An overview of theoretically calculated lithiation potentials can be found in Table 2.2, and an overview of reported potentials for the lithiation and delithiation of SiO$_2$ from experimental works are given in Table 2.3. As it can be observed from the presented tables, the reported potentials and the theoretically calculated potentials differ. It is well known that the experimental formation potential depends on various factors, but it is mainly affected by the kinetics of lithium insertion [28]. Importantly, reaction kinetics is affected by different factors, such as particle size, crystallinity and electrode composition. This could make the experimental potentials lower than the values predicted by thermodynamics since large overpotentials are observed.

Table 2.2: Theoretical capacity and theoretical potential of formation for the different SiO$_2$ lithiation products at 25°C [10].

Reaction	Product	Theoretical capacity [mAhg^{-1}]	Theoretical potential [V]
Eq. 2.3.4	Li$_2$Si$_2$O$_5$	693	1.30
Eq. 2.3.5	Li$_2$SiO$_3$	483	1.26
Eq. 2.3.6	Li$_4$SiO$_4$	676	1.15
Eq. 2.3.7	Li$_2$O	1109	0.68

In a study reported by Chang et al., the lithiation and delithiation potential of different reactions were studied from commercially available SiO$_2$. In that work, authors claim that Li$_2$Si$_2$O$_5$ and Li$_{15}$Si$_4$ are reversible phases and are repeatedly formed and decomposed into SiO$_2$ and Si [29]. However, there is no consensus in the literature about the reversible character of lithium silicate reactions towards Li-ions.

Table 2.3: Experimental lithiation and delithiation potentials of different Si compounds for SiO_2 anodes reported in literature.

Reaction	Potential [V]
1st lithiation:	
$5SiO_2 + 4Li^+ + 4e^- \rightarrow 2Li_2Si_2O_5 + Si$	0.27 [29]
$2SiO_2 + 4Li^+ + 4e^- \rightarrow Li_4SiO_4 + Si$	0.24 [29]
$SiO_2 + 4Li^+ + 4e^- \rightarrow 2Li_2O + Si$	0.72 [30]
$4Si + 15Li^+ + 15e^- \rightarrow Li_{15}Si_4$	0.00 [29]
1st delithiation:	
$Li_{15}Si_4 \rightarrow 15Li^+ + 4Si + 15e^-$	0.34 [29]
$2Li_2Si_2O_5 + Si \rightarrow 5SiO_2 + 4Li^+ + 4e^-$	0.39 [29]

Challanges of SiO$_2$ anodes

During lithiation, it has been observed that SiO_2 undergoes a lower volume change compared to Si, which can expand up to 300% [31]. However, the volume expansion and shrinkage can damage the SiO_2 structure during extended cycles. This can lead to electrode pulverisation and the re-formation of a solid electrolyte interphase (SEI), which continuously consumes lithium ions and electrolytes. The SEI formation is also associated with the electrical resistance of the active material, wherein increasing the SEI thickness leads to an increase in electrical resistance and slows the diffusion of Li-ions into the active material [32]. The SEI will be further introduced in section 2.4.

Furthermore, SiO_2 has poor electrical conductivity, which negatively impacts electron transport at the electrode, leading to reduced performance of the anode [33]. Additionally, SiO_2 exhibits low initial CE, which might come from the many lithium silicates and lithium oxide that are formed upon lithiation. It is also essential that silica has nanostructures, since this facilitates lithium movement across the interphase and also helps to accommodate volume fluctuations upon electrochemical cycling. Another disadvantage is that activating the SiO_2 material towards Li-ions is difficult, and to get a good electrochemical performance it needs an electrochemical activation pretreatment to trigger its reaction towards lithium ions [34].

Diatomaceous earth

One natural source of SiO$_2$ is found in diatomaceous earth (DE), which consists of fossil remains of microalgae (diatoms) mostly found in soil and oceans [35]. The diatoms are unicellular algae, where the shell, called frustule, displays a nano-to-microporous structure made of SiO$_2$. DE is characterised by unique properties such as high porosity, low weight, small particle size, high surface area, chemical inertness and low thermal conductivity. This material is therefore paving the way for numerous applications, including a promising source of nanostructured SiO$_2$ for LIBs anodes [36]. Yan et al. looked at hollow porous SiO$_2$ nanocubes and found out that the hollow nanostructure accommodated the large volume change and alleviate the structural strain during Li$^+$ insertion and extraction, as well as allowed rapid access of Li-ions during charge/discharge cycling [37]. Additionally, the formation of reversible and irreversible lithium silicates in the anode is one of the factors that determine the capacity, and the fast transport of lithium ions in hollow porous silica nanocubes is beneficial to the formation of Li$_2$O and Si [37]. This contributes to the high reversible capacity. As diatoms also have a porous 3D structure, it could behave similarly.

2.3.4   Conductive additives

To enhance the electronic conductivity of anodes, conductive additives are commonly integrated into the composition to promote efficient electron transport from the current collector to the active material [38]. Carbon black (CB) nanoparticles, graphene nanosheets, carbon nanotubes, and carbon nanowires are examples of carbon-based conductive additives. Among these, CB is a commonly used additive due to its ability to form a conductive network within the electrode, facilitating the efficient transportation of electrons from the current collector to the active material.

However, in the case of Si-based anodes, a significant issue leading to battery failure is the electrical disconnection that can occur between CB particles, Si nanoparticles, and current collectors due to the considerable swelling and contraction that occurs during charging and discharging cycles [38]. This issue can cause significant mechanical stress, leading to the breakdown of the anode material and ultimately leading to battery failure. Therefore, it is crucial to develop strategies that can effectively mitigate this problem to improve the performance and lifetime of Si-based anodes in batteries.

2.3.5   Binder

The binder is an important component which accounts for a small proportion of anode composition. The main purpose of the binder is to make sure that there is good contact between the active material, the conductive additives and the current collector [15]. Also, binders play an important role in maintaining good electrical conductivity and stable SEI formation, which affects battery performance.

2.3.6   Electrolyte

Liquid electrolytes consist of a mixture of lithium salt in organic solvents and in some cases the addition of additives. The electrolyte acts as a lithium-ion transport medium between the two electrodes and has a strong impact on the electrochemical performance of the battery. Furthermore, the electrolyte composition plays a crucial role in determining the nature and stability of the SEI. The electrolyte must satisfy several requirements such as [39]:

1. Retention of the electrode/electrolyte interphase during cycling when the electrode particles are changing their volume.
2. A Li^+-ion conductivity $\sigma_{Li} > 10^{-3} S/cm$ over the temperature range of battery operation.
3. An electronic conductivity $\sigma_e < 10^{-10} S/cm$, meaning almost electronic insulator.
4. A transference number $\sigma_{Li}/\sigma_{total} \approx 1$, where σ_{total} includes conductivities by other ions in the electrolyte as well as $\sigma_{Li} + \sigma_e$.
5. Chemical stability over ambient temperature ranges and temperatures in the battery under high power.
6. Chemical stability with respect to the electrodes, including the ability to form rapidly a passivating SEI layer where kinetic stability is required because the electrode potential lies outside the electrolyte window.
7. Safe materials, i.e., preferably non-flammable and non-explosive if short-circuited.
8. Low toxicity and low cost.

Meeting all these requirements is an important challenge, and therefore much research effort is being dedicated to the design of improved electrolyte formulations.

Electrolyte stability

An electrolyte's thermodynamic stability, also known as the electrochemical window, can be determined by the energy gap, E_g, between its lowest unoccupied molecular orbital (LUMO) and its highest occupied molecular orbital (HOMO) [40]. The redox potential of both electrode materials should fall within the window in order to avoid the reductive and oxidative degradation of the electrolyte. Meaning that $eV_{OC} = \mu_A - \mu_C \leq E_g$ as illustrated in Figure 2.2.
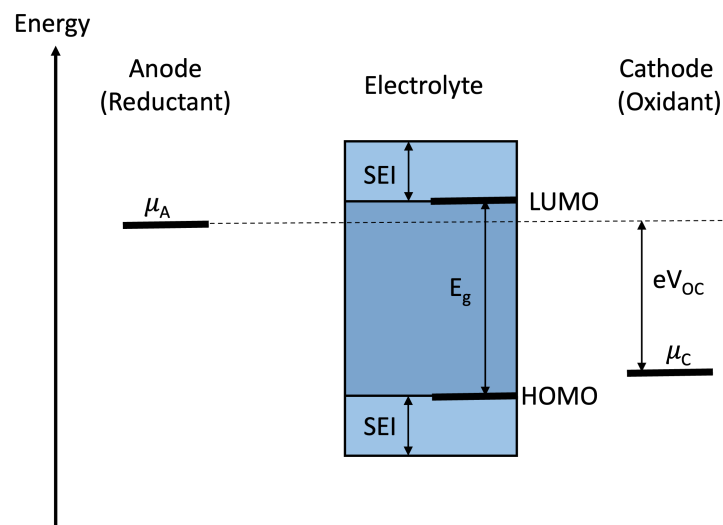
Figure 2.2: Schematic illustration of the electrochemical window, E_g, of an electrolyte.

Solvent
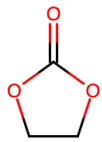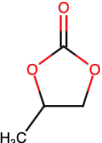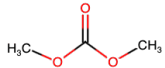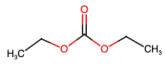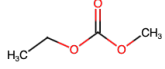
An aprotic non-aqueous solvent is usually used in LIBs. This is because it is more stable than solvents like e.g. ethanol. There are multiple requirements the solvent has to meet for a LIB working at ambient temperature [15]:

1. High dielectric constant, ε, so that it is able to dissolve salts at sufficient concentrations.
2. High fluidity (low viscosity, η) so that ion transport is facile.
3. Inert to all cell components.
4. Liquid within a wide temperature range, i.e., low melting point (T_m) and high boiling point, T_b.
5. Should be safe (high flash point, T_f), non-toxic, and low cost.

Most of the solvents used for LIBs are a mixture of cyclic and linear carbonates such as

ethylene carbonate (EC) and dimethyl carbonate (DMC). This mixture has shown to enhance both the solubility of salt and the mobility of ions, simultaneously [41]. Other common solvents are propylene carbonate (PC), diethyl carbonate (DEC) and ethyl methyl carbonate (EMC). The physicochemical properties of these solvents are listed in Table. 2.4.

Table 2.4: Main solvents used in non-aqueous liquid electrolytes for LIBs. Melting point, boiling point, viscosity, dielectric constant, flash point and mass density are given [20].

Solvent	Structure	T_m[°C]	T_b[°C]	$\eta(cP)$(25°C)	ε(25°C)	T_f(25°C)	$\rho[gcm^{-3}]$
EC		36.4	248	1.90 (40 °C)	89.78	160	1.321
PC		-48.8	242	2.53	64.92	132	1.200
DMC		4.6	91	0.59 (20 °C)	3.107	18	1.063
DEC		-74.3	126	0.75	2.805	31	0.969
EMC		-53	110	0.65	2.958	23	1.006

Lithium salt
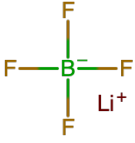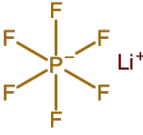
A lithium salt must be chosen with a solution in order to make the electrolyte. The lithium salts typically used in LIBs are given in Table. 2.5. A solvent mixed with a lithium salt (solute) should meet the following requirements for a LIB at ambient temperature [15]:

1. Complete dissociation in the solvent at a fairly high concentration.
2. Lithium should be able to move with high mobility.
3. The anion should be stable against oxidation reaction at the cathode.
4. The anion should be inert to the solvent.
5. Both anion and cation should remain inert towards all cell components, i.e., separator, electrode substrate, current collectors and cell packaging materials.
6. The solute should be non-toxic and stable against overheating of the battery etc. during abuse or short-circuiting.

The most commonly used lithium salt is lithium hexafluorophosphate (LiPF$_6$). The fluorinated inorganic anions, like PF$_6{}^-$, are especially favoured because of their superior dissolution and dissociation properties in non-aqueous media and their excellent abilities to passivate positive electrode surfaces [42]. LiPF$_6$ prevails as the industry standard in state-of-the-art lithium-ion cells, whereas lithium tetrafluoroborate (LiBF$_4$) has only limited applications in a few special lithium-ion cells designed for high-temperature purposes. One major drawback with LiPF$_6$ is that it is extremely sensitive to traces of water and alcohol. Water and alcohol lead to the formation of hydrofluoric acid (HF), which will corrode the Si particles [43].

Lithium bis(fluorosulfonyl)imide (LiFSI) on the other hand has good stability towards hydrolysis and does not form HF [15]. It also has the advantage of high ionic conductivity and better high-temperature stability than LiPF$_6$ [44]. Unfortunately, the price is more expensive than LiPF$_6$ and it is highly corrosive to the aluminium current collector in full cells [43].

Table 2.5: Main salts used in non-aqueous liquid electrolytes for LIBs and their characteristics. Molecular weight, melting point, decomposition point in solution, reported aluminium corrosion and conductivity in different solvents are given [20][45].

Li-salt	Structure	M_w	T_m	T_{dec}	Al corrosion	$\sigma[mScm^{-1}](1.0M@25°C)$		
		$[gmol^{-1}]$	[°C]	[°C]		in PC	in EC/DMC	in EC:EMC
LiBF$_4$		93.9	293	>100	No	3.4	4.9	
LiPF$_6$		151.9	200	~80	No	5.8	10.7	
LiFSI		187.1	145	>100	Yes			9.73

Electrolyte additive

One of the promising strategies to overcome the low reversibility of the anode is to use electrolyte additives. These additives can increase the stability of the SEI. It has been shown that some additives have the capability to form flexible SEI on Si, which can withstand its volume changes [46][47]. One of the most studied additives for Si anodes in LIBs is fluoroethylene carbonate (FEC). This is because of its positive effect on capacity reversibility [48]. Another additive, vinylene carbonate (VC) is also commercialised for LIBs because of its ability to increase the CE and thermal stability of graphite [49]. The chemical structure of VC and FEC are shown in Fig. 2.3. VC has also been shown to be used for Si anodes. In a study, it was found that VC additive used for nano-Si anodes outperforms FEC in terms of lifetime and efficiency because of the formation of a very flexible surface film, which survives the large volume changes of Si without surficial crack propagation [48]. However, the surface film showed high resistance for Li$^+$ migration as a rate-determining step, likely due to the absence of defects in the film structure turning VC unfavourable for high-power applications. In contrast, the FEC-derived SEI shows less flexibility and reversibility compared to VC but offers remarkable conductivity for Li$^+$-ions, which are excellent requirements for high power applications [48].

(a) VC   **(b)** FEC
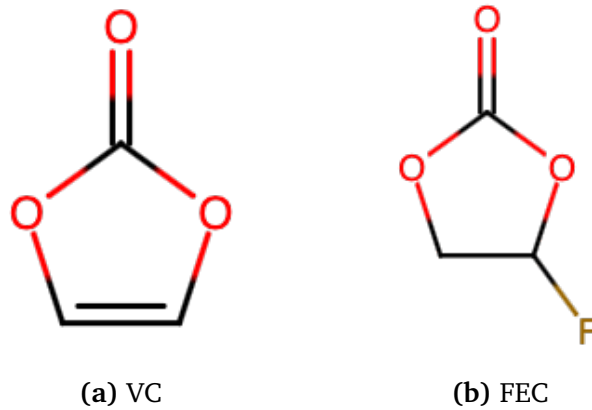
Figure 2.3: Molecular structure of VC on the left and FEC on the right.

Solvent and additive decomposition

Some of the reduction reactions of the cyclic EC and the linear DEC alkyl carbonate solvent are listed below [50].

The reduction reactions of **EC**;

$$2EC + 2e^- + 2Li^+ \rightarrow (CH_2OCO_2Li)_2 + CH_2{=}CH_2 \tag{2.3.8}$$

$$EC + 2e^- + 2Li^+ \rightarrow Li_2CO_3 + CH_2{=}CH_2 \tag{2.3.9}$$
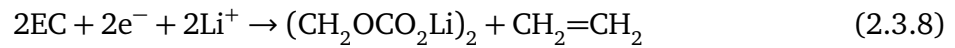
The reduction reactions of **DEC**, here R $= C_2H_5$;

$$ROCO_2R + e^- + Li^+ \rightarrow ROLi + RC \cdot O_2 \tag{2.3.10}$$

$$2\,ROCO_2R + 2e^- + 2Li^+ \rightarrow 2ROCO_2Li + R{-}R \tag{2.3.11}$$

$$ROCO_2R + 2e^- + 2Li^+ \rightarrow Li_2CO_3 + R{-}R \tag{2.3.12}$$
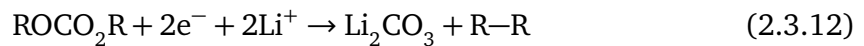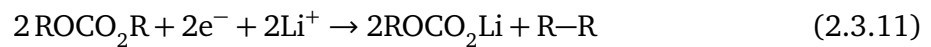
The main components found in the SEI as a result of solvent degradation from EC and DEC are lithium carbonate (Li$_2$CO$_3$), lithium alkyl-carbonates (ROCO$_2$Li) and alkoxides (ROLi).

As it was previously mentioned, the electrolyte additives VC and FEC improve the performance of the battery. Researchers believe that one key aspect of their favourable SEI formation is because of their decomposition into organic species [20]. In theory, FEC and VC would yield very similar reduction products, where the main difference is that the component LiF

is only present with FEC [51]. Decomposition products for both FEC and VC include Li_2CO_3, Poly(VC), $Li_2C_2O_4$ and HCO_2Li [51].

Reduction potentials of common electrolyte solvents and additives

Table 2.6 provides a summary of the reduction potential for popular electrolyte solvents and additives. It is important to acknowledge that experimental results may differ from the values listed in the table, owing to factors such as variations in the active material, electrolyte compositions, cell design and experimental conditions such as temperature.

Table 2.6: Experimental reduction potential of common electrolyte solvents and additives.

Solvent/additive	E_{red} (vs Li^+/Li) [V]	Reference
EC	0.65	[52]
EC/DEC	1.3	[53]
FEC	1.47	[48]
VC	1.05/1.25	[52]/[48]

2.4   Solid electrolyte interphase

The SEI is generated on the anode of LIBs during the first few cycles [54]. This electrode/electrolyte interphase was first introduced by Peled et al in 1979 [55] and its formation occurs when the electrochemical potential of the electrodes lies outside the electrochemical window of the electrolytes. Importantly, this layer is relatively stable after some cycles and then works as a passivation layer. The passivation layer is a Li^+-ion conductor and an electron insulator, which inhibits further electrolyte decomposition to improve the cycle life of the LIBs [56]. A schematic of the SEI formation is shown in Fig. 2.4.

The following requirements should be met by an ideal SEI for LIBs: [15];

1. Electron transference number, $t_e = 0$.
2. High ionic conductivity.
3. Uniform morphology and chemical composition.
4. Good adhesion to the anode materials (C, Si, Sn, . . .) surface.
5. Good mechanical strength and flexibility.
6. Low solubility in electrolytes.
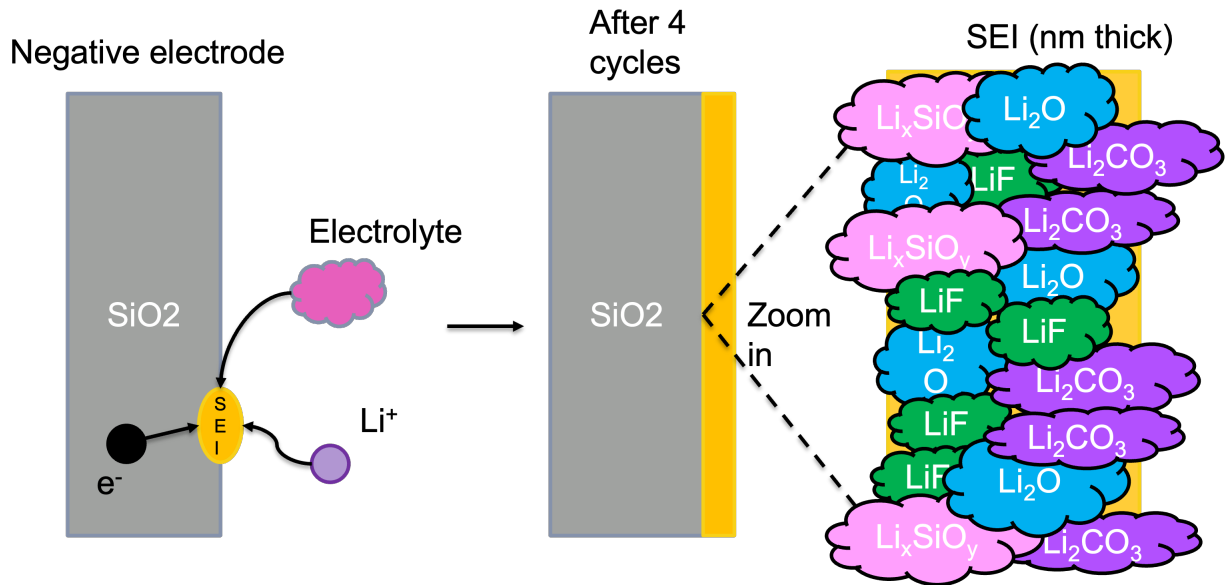
Figure 2.4: A schematic illustration depicting the formation of the SEI [1]. The initial SEI is formed during the charging process through reactions between the electrolyte, Li^+ ions, and electrons. The SEI is composed of several different components, and the figure illustrates components on SiO_2 anodes suggested by the literature.

SEI plays a critical role in the cyclability, rate capacity, irreversible capacity loss and safety of LIBs, and therefore a good control of its properties, such as chemical composition, thickness and structure, is highly desirable. However, for SiO_2 anodes, the relation between SEI properties and electrochemical cycling performance is still not well understood. This is due to the fact that the SEI layer is nanometric, amorphous air-sensitive and in-situally formed during electrochemical cycling. Poor understanding of the SEI has made it difficult to understand the physical and chemical properties of the SEI, for instance, ion transport, stability, and electrolyte reduction pathway, which are crucial for the battery performance [13].

It is generally understood that the SEI consists of a more inorganic part at the inner part of the SEI, while an outer more organic part at the SEI/electrolyte interphase [57]. The outer organic part consists mainly of semicarbonates, polymers or oligomers. While the inner part is more inorganic and consists of Li compounds like LiF and Li_2O [49]. Studies have reported that the inner layer also contains Li_xSiO_y with some Li_xSi_y [13]. Several studies argue that the lithiation of SiO_2 involves the conversion reactions shown in eq. (2.3.4), eq. (2.3.7) and eq. (2.3.6), which result in the formation of $Li_2Si_2O_5$, Li_2O and Li_4SiO_4. These products within the SEI will have a strong impact on the SEI properties, e.g. Li_4SiO_4 has been reported to

have a quite low ion conductivity. This can limit the Li$^+$-ion diffusion through the SEI, and therefore affect the charging rate of the battery.

2.5 Characterisation techniques

2.5.1 X-ray photoelectron spectroscopy (XPS)

XPS is a surface-sensitive analytical technique, where x-rays bombard the surface of a material and the kinetic energy of the emitted electrons is measured [58]. This technique stems from the approximation of the photoemission process, that is, if an x-ray photon interacts with a molecule, eg. LiF, it may cause the ejection of an electron (the photoelectron) from one of the LiF quantum energy levels (molecular orbitals) in that molecule, according to the Einstein photoelectric equation [59]:

$$KE = h\nu - BE \tag{2.5.1}$$

here $h\nu$ is the energy of the x-ray, BE is the binding energy of the electron in the specific orbital (the energy that is required to remove the electron) and KE is the kinetic energy of the emitted photoelectron. A schematic of this is shown in Fig. 2.5.
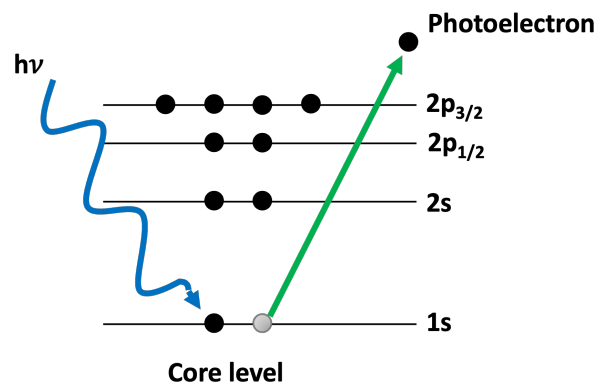
Figure 2.5: Illustration describing the emission of photoelectrons.

A high number of electrons is expected for energy levels corresponding to energy levels of elements present in the probed species. Any electron with a binding energy smaller than the x-ray source energy should be emitted from the sample and observed with the XPS technique. A survey scan from XPS will have peaks that correspond to the element and orbital from which

the photoelectrons were ejected. Survey scans detect a wide range of electron kinetic energies and are used to determine which elements are present in a sample. While high-resolution element scans detect electrons corresponding to specific orbitals (certain kinetical energy). Consequently, these scans enable a more comprehensive investigation, thereby facilitating the determination of the chemical environment surrounding the atoms within the sample. By conducting these detailed scans, a deeper understanding of the molecular interactions, bonding configurations, and chemical states of the sample's constituents can be attained.

The surface sensitivity of XPS is determined by how deep an electron can be generated and still escape without colliding with other electrons (inelastic collisions). The electrons that undergo at least one inelastic collision, lose energy and contribute to the background of the spectrum [58].

Depth profiling in XPS

Information beyond the natural probing depth can be obtained by combining XPS with sputter depth profiling using gas ions (usually Ar or Xe) [59]. The downside of this technique is that it is a destructive analysis. Specifically, the process can induce preferential sputtering of certain elements and chemical alterations within the sample. Notably, previous studies have indicated that the etching process can prompt the formation of Li_2O via the decomposition of SEI compounds like Li_2CO_3 [60].

Chemical shift

The core level peak position for an element can vary by more than 10 eV, and the position is dependent on the chemical environment. Variation in the elemental binding energies (the chemical shift) arises from differences in the chemical potential and polarisation of the compounds. These chemical shifts can be used to identify the chemical state of the material being analysed [61]. If the element is bonded to a more electronegative atom, the binding energy will be higher. For instance, in SiO_2, the Si atom is bonded to O, which is more electronegative than Si. As a result, the binding energy of the Si 2p core peak for SiO_2 is higher than for bulk silicon (Si-Si). However, for the silicates (Li_2SiO_3, Li_4SiO_4, $Li_2Si_2O_5$) formed during the lithiation of SiO_2, the binding energy will be very similar. Si have the same +4 oxidation state in all the products. This makes it difficult to distinguish the different components as they will have very similar binding energies, and could be a part of the same peak.

Charging effects

Insulating samples, like SiO_2, can charge during XPS analysis, which can cause unwanted peak shifts and distortion in peak shapes [62]. The emission of photoelectrons and Auger electrons can cause the sample to acquire a positive charge [58]. Samples that are conducting and semiconducting usually do not have this issue, since an electrical contact is normally made to the surface of the sample and the sample holder is grounded. This grounding allows the electrons lost due to emission to be replaced, and therefore the sample does not get positively charged. For the insulating samples, this is not possible, and if the sample starts to charge positively, it becomes harder to remove the subsequent electrons, and the binding energy of the electron will increase, generating peaks to shift to a higher binding energy. Additionally, it can lead to peak broadening and more peaks or shoulders appearing in the spectrum. This can lead to difficulties in analysing the XPS data.

Binding energy of elements

The table below shows the binding energies for relevant elements and compounds for this experiment.

Table 2.7: Characteristic binding energies for C 1s, O 1s, F 1s, Si 2p and P 2p from literature.

Orbital	Chemical state	Binding energy [eV]	Reference
C 1s	Carbon Black	284	[63]
	C-C/C-H	284.8	[64][65]
	C-O	286	[64]
	O-C=O	288.5	[64]
	Li$_2$CO$_3$	289.8	[66]
O 1s	Li$_2$O	528.4	[63]
	Li$_4$SiO$_4$	530 - 530.5	[63]
	Li$_2$CO$_3$	531.5	[67]
	C=O	531.5 - 532	[68]
	SiO$_2$	532.9	[68]
	C-O	533	[68]
	O$-$F$_x$	535	[68]
F 1s	LiF	685	[69]
	PF$_6^-$	687.8	[70]
Si 2p	Li$_x$Si	97.5	[63]
	Si	99.4	[71]
	Li$_x$SiO$_y$	101.3	[72]
	SiO$_x$/Si	103.3	[73]
	SiO$_2$	103.5	[71]
	SiO$_x$F$_y$	105 - 106	[72]
P 2p	PF$_6^-$	137	[72]

2.5.2 Hard X-ray photoelectron spectroscopy (HAXPES)

HAXPES is based on the same principle as XPS, however, utilising synchrotron radiation sources for high-resolution photoelectron spectroscopy in a kinetic energy range up to 10–15 keV, enables non-destructive, bulk-sensitive XPS measurements with considerably increased information depth of several tens of nanometers [74]. Additionally, tuning the kinetic energy of the photoelectrons enables a tool for depth profiling the chemical composition of buried interfaces without damaging the sample. The non-destructive depth profiling approach is advantageous over destructive sputtering techniques utilised in XPS, because the latter can change the chemical composition of the interface due to elements-specific sputter rates as previously mentioned.

2.5.3 Scanning electron microscopy (SEM)

The scanning electron microscope is one of the most versatile instruments available for the examination and analysis of the microstructure morphology [75]. It consists of an electron gun,

condenser lens, aperture, scan coils, objective lens and a detector. The electron gun generates an electron beam that is focused and scanned across the surface of the sample. This produces an image by collecting and processing the signals emitted from the sample surface. Common signals that are detected are backscattered electrons (BSEs) with high energy, secondary electrons (SEs) with low energy and excited x-rays [76].

Backscattered electrons

A fraction of the incident high-energy electrons hitting the sample will be scattered by angles greater than π, and these electrons have a finite probability of escaping the surface of the sample. The amount of BSEs depends on the average atomic number of the specimen and increases with increasing atomic number. The BSE signal is able to resolve local variations in mass density, resulting in the generation of atomic number contrast [76]. The atomic number contrast is useful since it offers the possibility of distinguishing between different phases and can give some information about the composition. The BSEs can additionally give information about the topology.

Secondary electrons

Most of the electron current emitted from a sample excited by an incident electron beam comes from SEs released from the sample's surface. The contrast effects in the SE image are due to surface topography, including the local curvature of the surface and the angle of incidence of the electron probe. The SE is primarily used to get 3D-like images, which give information about the topography.

2.5.4 Focused ion beam (FIB)

A FIB can be used to mill, cut or image samples with high precision [77]. The technique works by focusing an ion beam of high-energy ionised atoms, focusing them onto the sample for the purpose of imaging, etching or milling the surface of a material. These ions have a high relative mass allowing them to remove surface atoms from their position and produce SEs from the surface. Usually, FIB systems utilise a liquid-metal ion source such as Gallium (Ga) to produce Ga^+. By using an electric field, the ions are then pulled out and focused into a beam. The ion beam is then passed through apertures and is scanned over the sample surface.

2.6   Electrochemical characterisation techniques

2.6.1   Galvanostatic cycling

Characterisation of LIBs involves the galvanostatic (maintaining a constant current) charge and discharge during numerous cycles. Galvanostatic cycling is used in order to evaluate the active materials performance under practical operation conditions [78]. The technique essentially corresponds to battery cycling under galvanostatic mode. Here, the working electrode is submitted to a constant current, I, and voltage, V, versus time is recorded between minimal and maximal voltage values. The current is reversed when the maximum/minimum voltage is obtained. As the current is applied the potential increases/decreases before the potential stabilises as an electrochemical reaction happens or the current is reversed. The cycle is repeated multiple times in order to get electrochemical information.

The primary knowledge obtained from this technique is the capacity of the electrode as a function of rate, the change of the potential as a function of the state of charge, the cyclability, the thermodynamic reversibility and the estimation of the ohmic drop [78]. Fig. 2.6 shows a characteristic plot of the potential as a function of the capacity for a half cell.
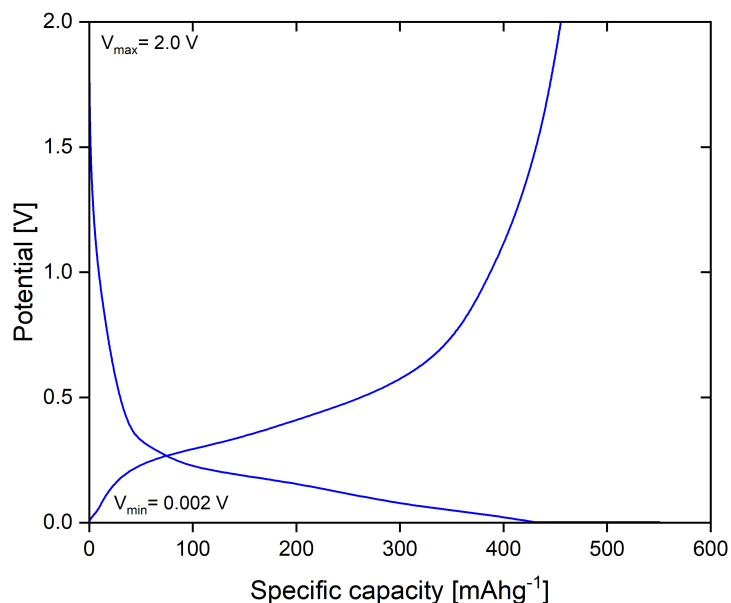
Figure 2.6: Schematic of galvanostatic cycling. The maximum and minimum voltage is 2.0 V and 0.002 V, respectively.

2.6.2   Differential capacity (DC)

A DC plot, as shown in Fig. 2.7, can be used to gain insight into reactions happening in a galvanic cell during galvanostatic cycling [79]. The main presentation of DC is given by the derivative of the electrode charge with respect to the voltage (dQ/dV) vs voltage (V). The peaks in these curves are associated with phase transitions of the electrode material. The peaks that emerge during delithiation are referred to as anodic peaks, whereas the peaks that arise during lithiation are known as cathodic peaks. The potential at which a peak is located can be used to determine the presence of an electrochemical reaction. However, it can be difficult to distinguish individual reactions because multiple reactions could be taking place at the same potential, resulting in convoluted peaks.
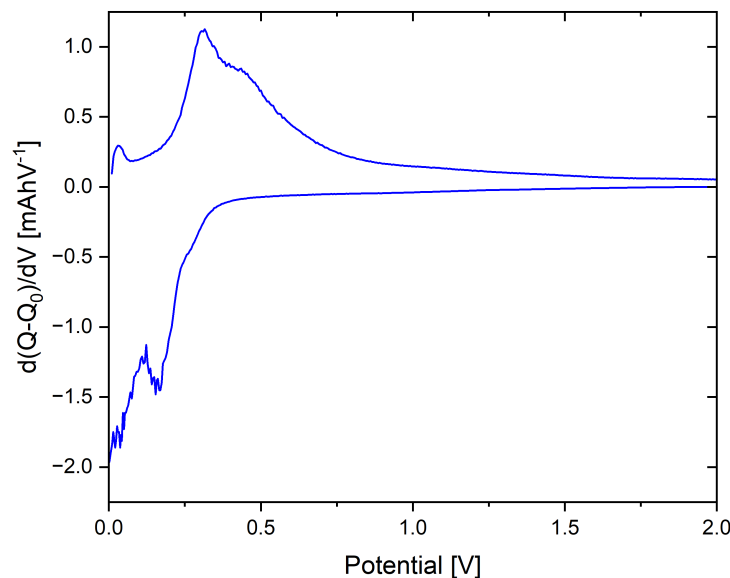
Figure 2.7: Differential capacity plot from galvanostatic cycling.

2.6.3   Cyclic voltammetry (CV)

In CV, the potential is varied at a constant rate between a lower and upper limit and the resulting current is measured against potential. This electrochemical technique is commonly used to investigate the reduction and oxidation processes of molecular species [80]. This method involves applying a potential to a sample while monitoring the current that flows through the system. The current (I) is recorded as a function of the applied potential. Fig. 2.8 shows a

typical voltammogram, here the x-axis is the applied potential, while the y-axis is the resulting current passed. The most useful information that can be obtained from voltammograms is the anodic and cathodic peak currents, which indicate electrochemical reactions in the material. If the redox reactions are reversible, the anodic and cathodic peaks will have a similar shape.

The scan rate of the experiment controls how fast the applied potential is scanned, and is given in mVs^{-1}. An increased scan rate leads to an increased current observed, which can be useful when investigating electrochemical reactions by CV [80].
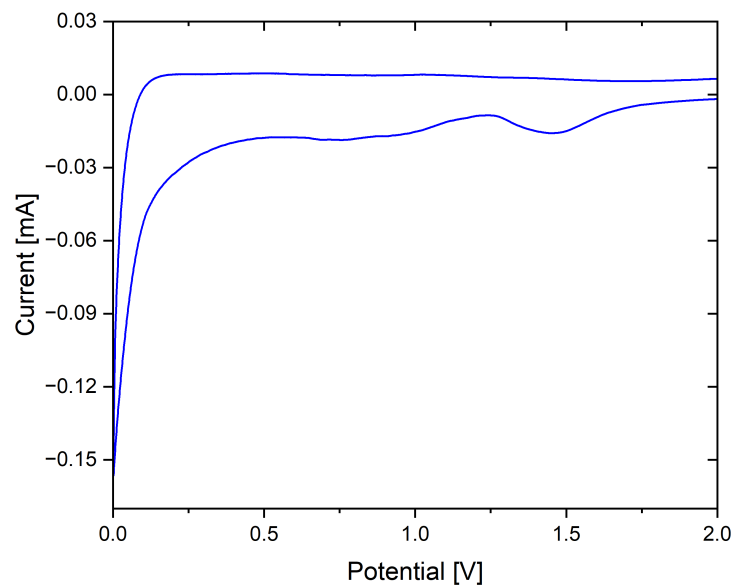
Figure 2.8: Schematic of a voltammogram.

Chapter 3

Experimental

Overview

This section provides a comprehensive account of the experimental procedures, techniques and equipment employed in this study. The experimental investigation can be classified into seven distinct stages. Firstly, the reduction of diatom particle size was carried out via ball milling. Secondly, the binder was prepared, and electrodes were produced via a slurry and tape casting. The third stage involves electrolyte preparation. Then the fourth stage involved cell assembly. Following that, the fifth section explains the electrochemical characterisation, by galvanostatic cycling and cyclic voltammetry. Then the sixth stage involves compositional characterisation by XPS. Finally, the morphological characterisation of the electrodes was performed before and after cycling.

3.1 Ball milling of active material

The diatoms were milled in order to increase their surface area and increase the compaction density of the anode [81]. Planetary milling (PM100, Retch) was conducted in a Tungsten Carbide (WC) jar (125 mL) with WC balls (40 g, 3 mm diameter) at 20:1 ball to diatoms ratio. Ethanol (6 ml) was added to the jar. The SiO_2 powder (Diatomaceous earth, 2g, Sigma-Aldrich) was wet milled for 3 hours at 400 rpm. This was done by alternating between 10 minutes of clockwise rotation, followed by a 5-minute rest period, and then 10 minutes of counterclockwise rotation. The alternating of the rotation was done to improve the homo-

geneity of the milling. This sequence was repeated until the desired endpoint was reached. Once the milling was complete, the resulting sludge solution was collected into a glass beaker using a plastic pipette and spatula. Any remaining sludge solution on the walls of the milling chamber was rinsed with ethanol and also collected into the glass beaker. Subsequently, the sludge solution was subjected to a drying oven at a temperature of 120 °C for a duration of 2 hours. After the drying process, the diatom cake was crushed using a mortar and pestle and then transferred into a glass vial.
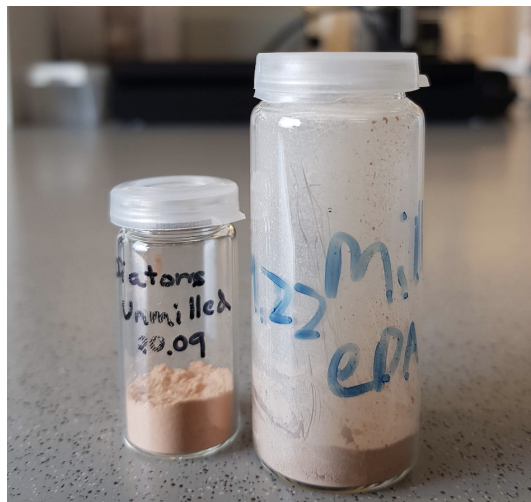
Figure 3.1: The left sample glass shows unmilled diatoms, while the right sample glass shows milled diatoms.

3.1.1   Laser diffraction

To evaluate the particle size of the diatoms, laser scattering (Partica LA-960, Horiba) was conducted on the milled and unmilled frustules. The measurements were performed in wet mode, by using a suspension of SiO$_2$ in deionised water (DI water). Some drops of the suspension were added to the instrument by a pipette until the transmission dropped below 95 %. To minimise the agglomerates, 5 minutes of sonification was conducted in the Partica before measurements. The instrument utilised laser diffraction with 405 nm LED (3 mW) and 650 nm (5 mW) laser diode to acquire volumetrically based particle size distribution (PSD) based on the refractive index of SiO$_2$ in water.

3.2   Slurry preparation and electrode casting

The binder was prepared by mixing Sodium Alginate (Alginic acid sodium salt, 0.5 g, Sigma-Aldrich) and DI water in a beaker at a mass ratio of 1:60. The beaker was then placed on a hot plate with a temperature of 60 °C and stirred for 3 hours at 500 rpm with a magnetic stirrer until the powder was fully dissolved. Aluminium foil was wrapped around the beaker while it was mixing. After the mixing the binder was kept in a fridge and not longer than 7 days. The actual binder composition is found in Appendix section A.1.1.

The slurry was prepared by adding active material (AM) and conducting additive (carbon black (CB)(C-NERGY C65, Timcal) to a retsch jar with a ball. This was placed in a shaker (Retch Mixer MM400) and mixed for 5 minutes at 25 Hz. Then the alginate binder was added to the jar and retched for 40 minutes at 25 Hz. The composition of the slurry was (75 wt% AM: 15 wt% CB: 10 wt% binder), and the actual slurry composition is found in Appendix section A.1.2. Next, the retch jar was put in the ultrasonic bath for 5 minutes to break up any agglomerates. After mixing, the slurry was tape casted (RK K Control Coater 101) onto a copper current collector (Gelon, 18 µm), by using the doctor blade number 4 and the slowest speed on the caster. Before tape casting, the copper foil was washed with Isopropanol to remove any dust. The cast was then air-dried under an evaporation fume hood overnight. When the cast had dried, 16 mm diameter electrodes were punched out with the copper electrode between two pieces of paper. An image of the dried and cut cast is shown in Figure 3.3. Electrodes were then weighted and placed in an aluminium tray. The loading of each electrode can be found in the Appendix section A.1.3.
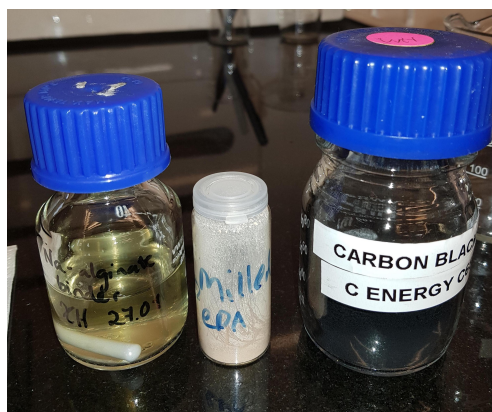
Figure 3.2: From the left alginate binder, silica powder and carbon black used in the slurry for tape casting.

(a) Electrode cast on copper foil after drying. **(b)** Electrode cast after punching out electrodes.

Figure 3.3: Anode cast.

3.3   Electrolyte preparation

One type of electrolyte was used in this project. The electrolyte decision was based on the specialisation work conducted the previous semester where LiPF$_6$ with FEC was shown to be one of the best-performing electrolytes for this system [1].

The electrolyte preparation was conducted in a glovebox (Labmaster Big glove box, MBRAUN). The electrolyte was prepared by mixing FEC (1 mL, Sigma-Aldrich) and LiPF$_6$ (1.0 M, 11.4 mL, EC:DEC 50/50 vol%, Sigma-Aldrich). This resulted in a 1.0 M LiPF$_6$ EC/DEC 1:1vol% 10 wt% FEC electrolyte. The flask used to store the electrolyte was dried beforehand in an oven at 60 °C overnight to remove any moisture.

3.4   Cell assembly

Coin cells of type CR2032 were assembled as half cells, with the electrode from the cast described in section 3.2 as the working electrode (WE) and lithium foil as a counter electrode (CE). LiPF$_6$ with FEC was used as electrolyte as described in section 3.3. The coin cell parts

were supplied by Horsen Corp. The cell assembly was conducted in a glove box (Labmaster Big glove box, MBRAUN) with argon atmosphere and a H_2O and O_2 level below 0.1 ppm.

Before transferring the cut electrodes to the glove box, they were heated at 120 °C under vacuum. To make the coin cell, the gasket was placed into the cell bottom, then the electrode was placed on top with the AM facing upwards and the copper foil touching the cell bottom. Afterwards, 25 µL of electrolyte was added in the centre of the electrode. Then a separator (Celgard 2400, 17 mm diameter) was placed on top, and an additional 25 µL of electrolyte was ejected on top of the separator. A 14 mm diameter lithium disk (99.9%) was brushed on both sides to ensure that any oxide layer was removed. Then the lithium disk was pressed against a stainless-steel spacer (CR2032, 0.3 mm thick, Hohsen Corp.). This lithium spacer was then put on top of the electrolyte with the lithium disk touching the electrolyte. Then a spring was centred onto the spacer and the cell cap was placed on top. The coin cell was then lightly pressed between a piece of paper in order to remove excess electrolyte. Finally, the cell was hermetically sealed using a crimping machine (Automatic Coin Cell Crimper, Hohsen Comp.). A schematic of the coin cell assembly and the different components in the cell is shown in Fig. 3.4.
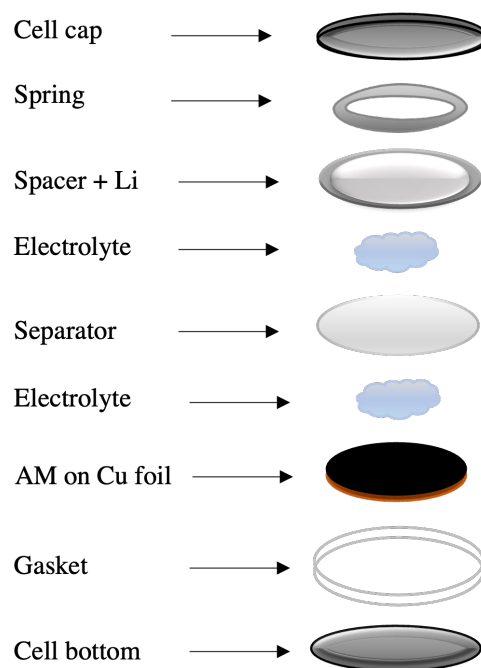
Figure 3.4: Schematic of coin cell assembly with the different components.

3.5 Electrochemical characterisation

3.5.1 Galvanostatic cycling

Half cells were cycled by applying a sequence of constant current and constant voltage steps, which altogether provide a slow but steady activation of the SiO$_2$ particles. Slow galvanostatic cycling at 50 mAg^{-1} with respect to the active material during the first lithiation step ensures a gradual formation of an SEI layer. The cells were first lithiated down to 2 mV with potentiostatic holding for 48 h. Subsequently, constant current delithiation was performed at 50 mAg^{-1} up to a voltage cut-off of 2 V followed by an immediate constant voltage holding step for 24 h, ensuring complete delithiation. This was repeated 3 times in order to fully activate the SiO$_2$ active material and reach a stable reversible capacity. The current used was 50 mAg^{-1} during these activation steps and for further cycling a current of 100 mAg^{-1} was used to evaluate the cycling performance of the anode. The cells were cycled in the galvanostat BioLogic BCS 805. EC-Lab was used to process the electrochemical data. From the DC plots, the potential values for XPS characterisation were selected.

Cells cycled for XPS

Dedicated half-cells were cycled until reaching voltage values selected from the DC plots during subsequent lithiation/delithiation cycles. For the first lithiation cycle, half-cells were galvanostatically cycled from OCV, typically 3.2-3.3 V to 1.1 V, 0.5 V, 0.2 V and 0.002 V. Once the selected desired potential was reached, a potentiostatic holding step was applied. For all the cells the potential hold was conducted for 48 hours. At that stage, it could be assumed that all cells reached steady-state conditions. A similar procedure was followed for half-cells in the first delithiation stage. In this case, the selected voltages were 0.2 V, 0.5 V and 1.1.V. For the second lithiation cycle, individual cells were stopped at 0.25 V, 0.15 V, 0.04 V and 0.002 V. In that way, each electrode potential could be related to the chemical composition of the anode during lithiation and delithiation [13].

3.5.2 Cyclic voltammetry

CV was additionally performed in order to get complementary data to know what potentials the cells were going to be stopped to investigate the SiO$_2$ reactions. Two different scan rates were used, 0.1 mVs^{-1} and 0.05 mVs^{-1}. The cells were cycled between 2.00 V and 0.002 V for

4 cycles. The cells were cycled in the galvanostat BioLogic BCS 805, and EC-Lab was used to process the electrochemical data.

3.5.3   Overview on cycled cells

Table 3.1: Overview of cycled cells and their corresponding analysis. L and D denote lithiation and delithiation, respectively.

Analyses	Cycle	L/D	Potential (vs Li^+/Li) [V]	Scan rate [mVs^{-1}]
Activation cycles (DC)	1 - 4	L&D	2.00 - 0.002	-
Extended cycles	1 - 200	L&D	2.00 - 0.002	-
CV	1 - 4	L&D	2.00 - 0.002	0.10
CV	1 - 4	L&D	2.00 - 0.002	0.05
XPS	1	L	1.1	-
XPS	1	L	0.5	-
XPS	1	L	0.2	-
XPS	1	L	0.002	-
XPS	1	D	0.2	-
XPS	1	D	0.5	-
XPS	1	D	1.1	-
XPS	2	L	0.25	-
XPS	2	L	0.15	-
XPS	2	L	0.04	-
XPS	2	L	0.002	-
XPS	4	D	2.00	-

3.6   Compositional characterisation - XPS

3.6.1   Cell dissasembly

Before characterisation with XPS the coin cells were disassembled in an argon-filled glovebox. After disassembly, the electrodes were rinsed in a fresh DMC bath and then dried. Then, 5 mm x 5 mm electrodes were cut with a scissor. The electrodes were stored in the glovebox until use, in order to minimise contamination.

3.6.2   XPS measurements

In-house XPS measurements were carried out at NTNU NanoLab with a Kratos Axis Ultra DLD. First, the cut electrodes were stuck to carbon tape on a sample holder as shown in Fig. 3.5 in the glovebox, and then placed in an airtight transfer arm. The transfer arm was taken to the XPS instrument and pumped to vacuum so that the electrodes were never exposed to ambient air. The XPS analysis was conducted using an Al Kα radiation source (hv = 1486.6 eV) under ultrahigh vacuum (10^{-9} Torr). The analysed area of the sample was 300 x 700 μm^2, with a probing depth of approximately 5 nm, and an exponential decay in the signal. The electrodes were etched using an Ar-ion beam for 0, 30, 60 and 90 seconds, to get a depth profile. Both survey spectra and high-resolution spectra of Si 2p, O 1 s, C1 s and F 1s were recorded at each etching time.

The binding energies of all elements were referenced to the C-C bonding energy at 284.8 eV. The spectra were analysed and fitted using the CasaXPS software. The spectra were analysed using a nonlinear Shirley background, and peak positions of elemental spectra were conducted using Gaussian-Lorentzien (70:30) curve fitting.

Figure 3.5: Image of the cut electrodes placed on the sample holder before being inserted in the XPS transfer arm.

3.6.3   Note on XPS calibration in CasaXPS

The high-resolution C 1s spectra were analysed by adding peaks for C-C, CB, C-O, O-C=O and Li$_2$CO$_3$. Then the peaks were analysed. To calibrate all the spectra to the right binding energy, the Spectrum Processing option of CasaXPS software was used. On the Calibration tab, C-C

binding energy was set to 284.8 eV. Then, the option of Select Regions and Components was chosen and it was applied by Row (1st Comp). Since the first component in Quantification Parameters is C-C, all the spectra were calibrated according to the C-C peak at 284.8 eV.

3.7 Morphological characterisation

3.7.1 FIB

A dual-beam FIB instrument (Helios NanoLab DualBeam FIB, FEI) was utilised to perform FIB cross-section analysis of the electrodes. To obtain the cross-section, a gallium-ion beam was employed to cut a square (20 μm x 20 μm x 10 μm) at a high beam current of 21 nA, acceleration voltage of 30 kV and tilt angle of 52°. Subsequently, one of the sides of the cross-section was polished with a low current of 2.7 nA and an acceleration voltage of 5 kV. This was conducted in an effort to minimise the effect of the ion beam on the morphology of the material.

3.7.2 SEM

To get high-resolution images of the morphology and cross-sections, the samples were placed into a field emission SEM (Apreo, FEI). The images of the cross-sections were captured at a working distance of 10 mm and an angle of 45 °. The acceleration voltage was 2 kV and a beam current of 13 pA. Both standard and immersion mode were used. FIB and SEM analysis was conducted on the electrodes listed in Table 3.2.

The images of the unmilled diatoms were also taken by the SEM. Here the acceleration voltage was 1 kV, the beam current was 6.3 pA and the working distance was 3-3.4 mm. Immersion mode was used.

Table 3.2: Cells for FIB and SEM measurements. The potential indicates the voltage at which the cell was stopped.

Cells	Potential (vs Li$^+$/Li) [V]
Pristine	-
1 lithiation	0.002 V
1 delithiation	1.1 V

Chapter 4

Result

4.1 Overview

This chapter presents experimental results divided into four main sections. The first section presents the diatomaceous earth used as active material in the electrode by SEM images and particle size distribution. The second section presents the results from the electrochemical characterisation of the SiO_2 anodes done by galvanostatic cycling and CV. These measurements served to identify the potentials at which changes in chemical species were expected. In the third section, the results of compositional analysis by XPS on different cells stopped at the selected potentials during the first lithiation/delithiation cycle, second lithiation and fourth delithiation cycle are shown. Lastly, the morphology of the pristine and cycled electrodes is presented by SEM and FIB cross-sections.

4.2 Characterisation of the active material

4.2.1 Microstructure of frustules

The microstructure of the unmilled diatomaceous earth is shown by SEM images in Fig. 4.1. The material exhibits a variety of structures and porous layers. The main structure of the frustules appears to have a cylindrical shell with periodic arrays of pores. Some of the frustules have a hole of around 5 μm on the top of the cylindrical shell. The height of the shells appears to be in the range of 20 μm - 5 μm. Furthermore, not all of the frustules appear intact, with some being fragmented or broken.

(a)　　　　　　　　　　　　　　　　　**(b)**

(c)　　　　　　　　　　　　　　　　　**(d)**

(e)　　　　　　　　　　　　　　　　　**(f)**
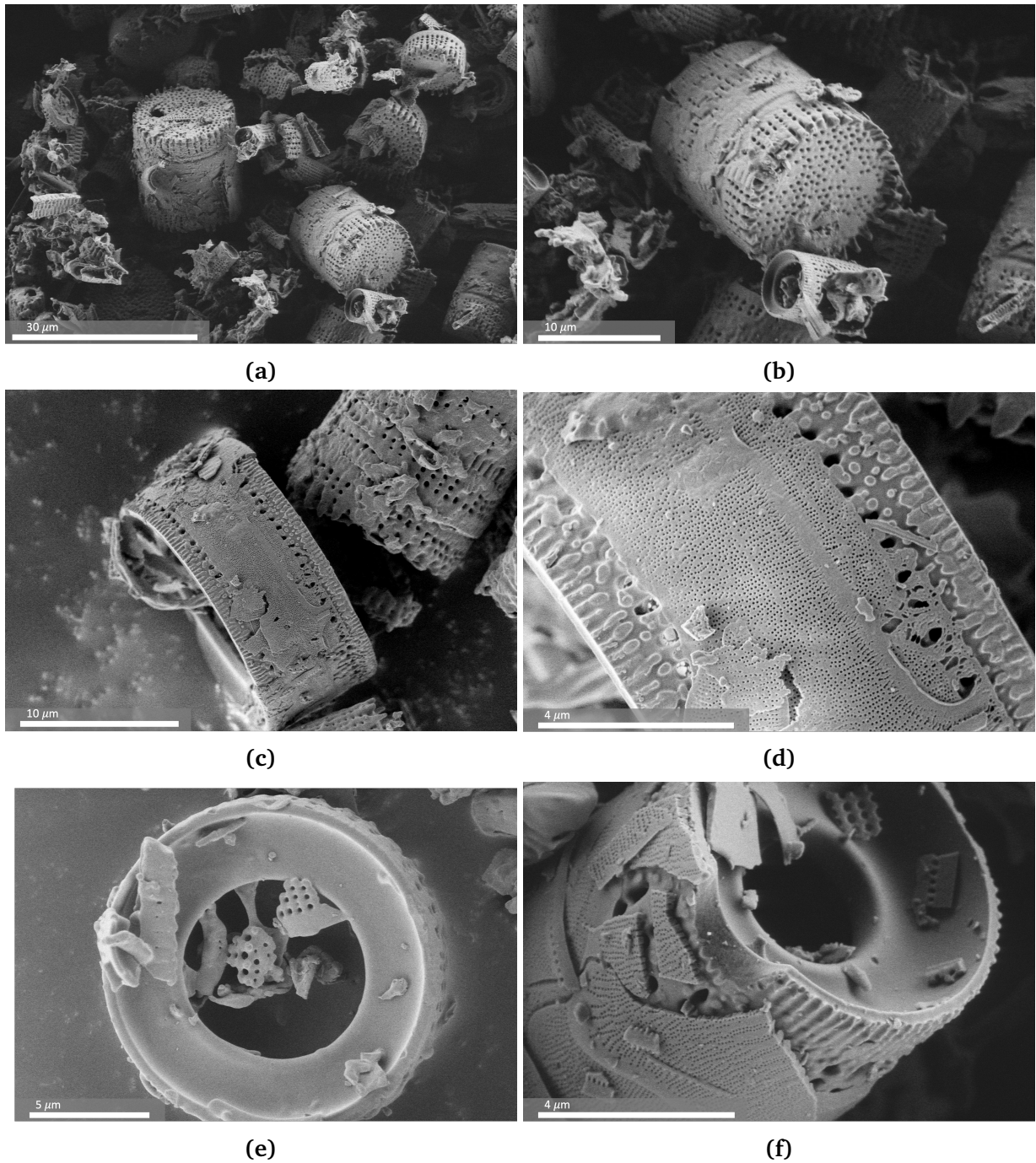
Figure 4.1: SEM images of the various structures of diatomaceous earth frustules.

4.2.2 Particle size distribution

The PSD of the milled SiO_2 determined by laser diffraction is depicted in Fig. 4.2. The unmilled particles had an average particle size of 17 μm and the milled particles had a particle size of 430 nm.
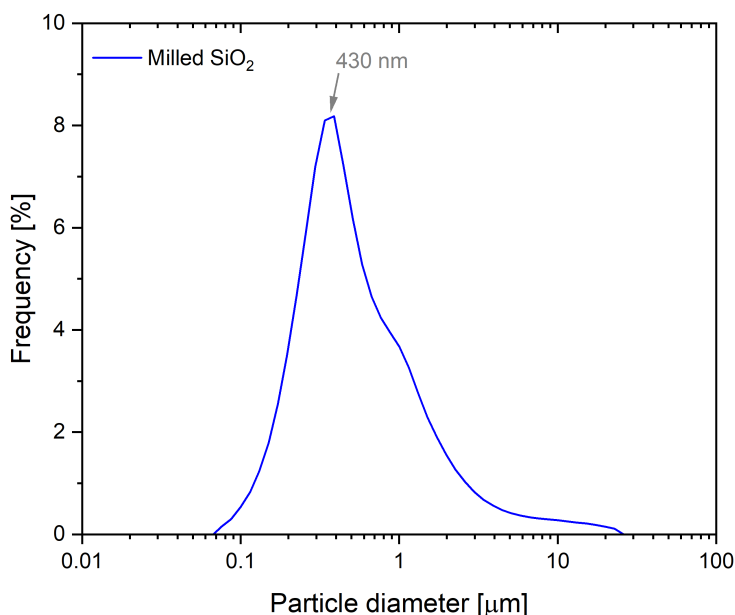
Figure 4.2: PSD of milled SiO_2 by laser diffraction.

4.3 Electrochemical characterisation

4.3.1 Cycling stability

The voltage profiles during galvanostatic cycling are presented in Fig. 4.3. The first four activation cycles are shown in Fig. 4.3a, and the extended cycling graphs are depicted in Fig. 4.3b. Noting that when the cells proceed into extended cycles, after the 4 activation cycles, the current was changed from 50 mAg^{-1} to 100 mAg^{-1}. For electrochemical performance data, the amount of active material in the electrode was 50%, and the loading is presented in Appendix A.1.3. In Table. 4.1 the specific discharge capacity corresponding to the four activation cycles and extended cycles are displayed. The specific capacity increases during the activation cycles. Further cycling at a higher current showed a relatively stable capacity trend, which remains above 1000 mAhg^{-1} in the range from 10 to 200 cycles.
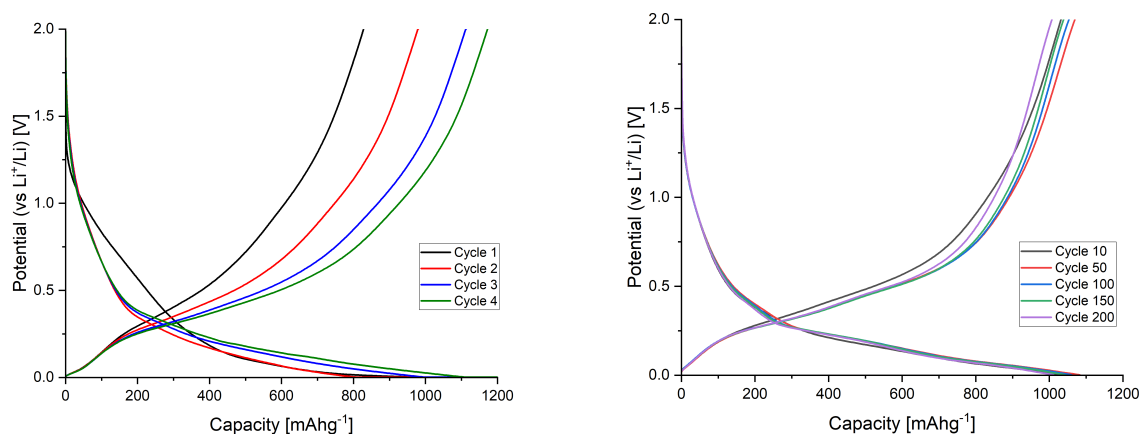
(a) Voltage profile of cycle 1, 2, 3 and 4 at a constant current of 50 mAg^{-1}.

(b) Voltage profile of cycle 10, 50, 100, 150 and 200 at a constant current of 100 mAg^{-1}.

Figure 4.3: Voltage profiles of activation cycles (1, 2, 3 and 4) and extended cycles (10, 50, 100, 150 and 200) during galvanostatic cycling between 2 V and 0.002 V.

Table 4.1: Overview of the specific discharge capacity corresponding to activation cycles and extended cycles. The activation cycles and extended cycles were cycled at a constant current of 50 mAg^{-1} and 100 mAg^{-1}, respectively.

Cycle number	1 [mAhg^{-1}]	2 [mAhg^{-1}]	3 [mAhg^{-1}]	4 [mAhg^{-1}]	10 [mAhg^{-1}]	50 [mAhg^{-1}]	100 [mAhg^{-1}]	150 [mAhg^{-1}]	200 [mAhg^{-1}]
Activation cycles	828	980	1113	1172	-	-	-	-	-
Extended cycles	-	-	-	-	1032	1069	1053	1039	1007

4.3.2　Differential capacity analysis

DC plots for the first four activation cycles are presented in Fig. 4.4. In the 1st cycle there are three anodic peaks (delithiation) observed at 0.029 V, 0.3 V and 0.45 V, and three cathodic peaks (lithiation) at 1.47 V, 0.83 V and 0.042 V. The peak at the lower potential (0.042 V) could be an indication of SiO$_2$ reaction [10][82]. The peak at around 1.47 V is usually attributed to the reduction of the additive FEC at the initial SEI formation [48]. And the peak at 0.83 V could be associated with the reduction of EC [52] Both of these peaks correspond to irreversible reactions and the peaks are not visible in the subsequent cycles. However, the cathodic peaks are now observed at the potentials 0.26 V, 0.17 V and 0.045 V. The two anodic peaks at 0.3 V and 0.45 V, and the two cathodic peaks at 0.045 V and 0.17 V are associated with Li$_x$Si delithiation and Si lithiation, respectively [83].
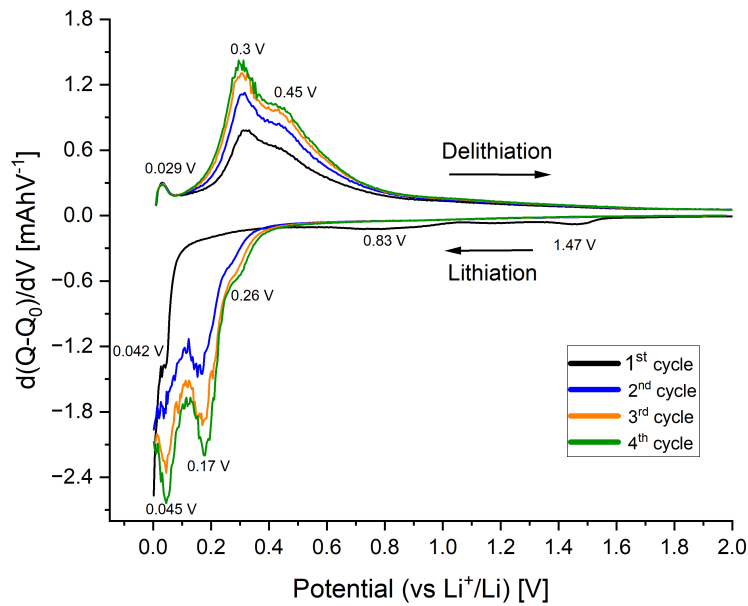
Figure 4.4: DC plot of the four activation cycles during galvanostatic cycling.

4.3.3 Cyclic voltammograms

CV curves as obtained from cycling of the SiO_2 electrode at a scan rate of 0.1 mVs^{-1} and 0.05 mVs^{-1} for the first four cycles between 2 V and 0.002 V and are shown in Fig. 4.5 and Fig. 4.6, respectively. In Fig. 4.5a, three distinct reduction peaks are observed in the cathodic branch during the first lithiation at 1.45 V, 0.73 V and 0.12 V. The lithiation curves for the second, third and fourth cycles have a similar trend, with no distinct peaks. In Fig. 4.5b, during the first delithiation three anodic peaks at 0.22 V, 1.06 V and 1.38 V are observed.

At an increased scan rate, 0.05 mVs^{-1}, shown in Fig. 4.6a, four cathodic peaks are observed at 1.45 V, 1.16 V, 0.73 V and 0.1 V. At the anodic curve four peaks are shown at 0.2 V, 0.5 V, 1.03V and 1.38 V, as shown in Fig. 4.6b.

(a) CV curves of the four activation cycles.

(b) Zoomed in delithiation curve.
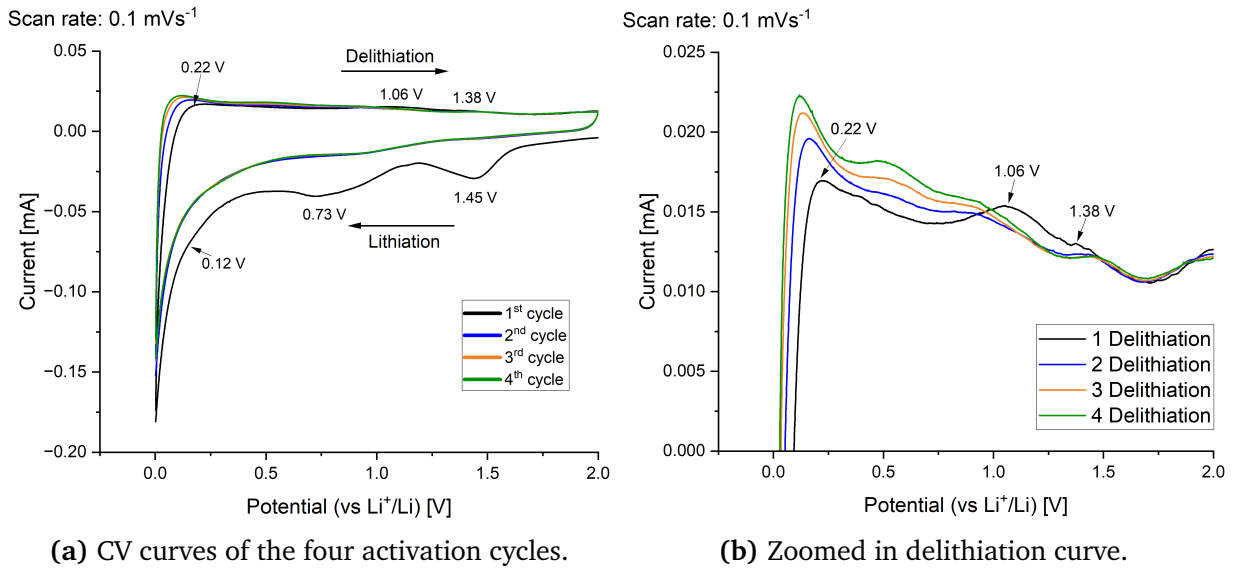
Figure 4.5: CV profiles at a scan rate of 0.1 mVs^{-1} between 2.0 V and 0.002 V. The arrows indicate the peak position with the corresponding potential value.

(a) CV curves of the four activation cycles.

(b) Zoomed in delithiation curve.
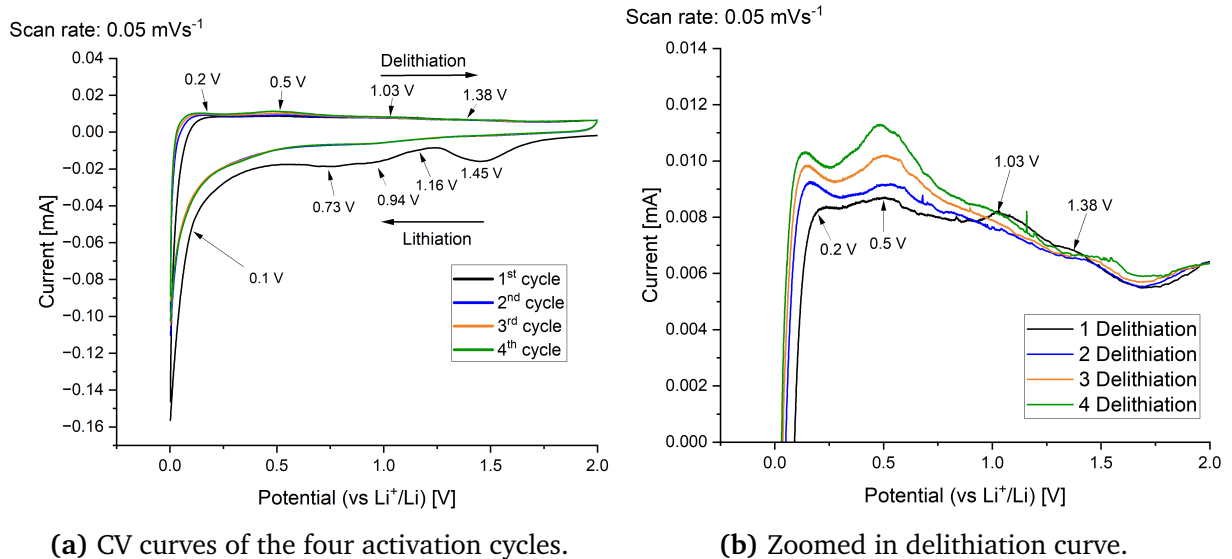
Figure 4.6: CV profiles at a scan rate of 0.05 mVs^{-1} between 2.0 V and 0.002 V. The arrows indicate the peak position with the corresponding potential value.

Combining DC and CV peaks

A summary of what potentials the peaks were located in the differential capacity and cyclic voltammetry plots is shown in Table. 4.2. From these results, the potential at which the cells would be stopped to investigate the SiO_2 reactions was decided.

Table 4.2: Summery of peak positions from the DC and CV plots at first lithiation and delithiation and the second lithiation.

Analysis	1st lithiation peaks [V]				1st delithiation peaks [V]				2nd lithiation peaks [V]			
DC	1.47	-	0.83	0.042	0.029	0.3	0.45	-	-	0.26	0.17	0.045
CV (0.1 mVs^{-1})	1.45	-	0.73	0.12	0.22	-	1.06	1.38	1.45	1.0	0.12	-
CV (0.05 mVs^{-1})	1.45	1.16	0.73	0.10	0.20	0.50	1.03	1.38	-	-	0.10	-

4.3.4 Current decay curves

Current decay curves for the 1st lithiation cycle of cells stopped at 1.1 V, 0.5 V, 0.2 V and 0.002 V are shown in Fig. 4.7. The goal is to study the electrode at a steady-state at a given potential, which is achieved after a substantial decay of the initial current. Cells stopped at 1.1 V, 0.5 V and 0.2 V show a rapid decrease in current, and have an end current below 10% of the initial current before the potential has been held for 48 hours. However, the cell stopped at 0.002 V showed a slow decrease in current and showed 10% of initial current after 48 hours. Because of this, the selected potential for the cells was held for 48 h. The decision on having the same holding time for all selected potentials was based on similar studies that had the same holding time for all cells [13].
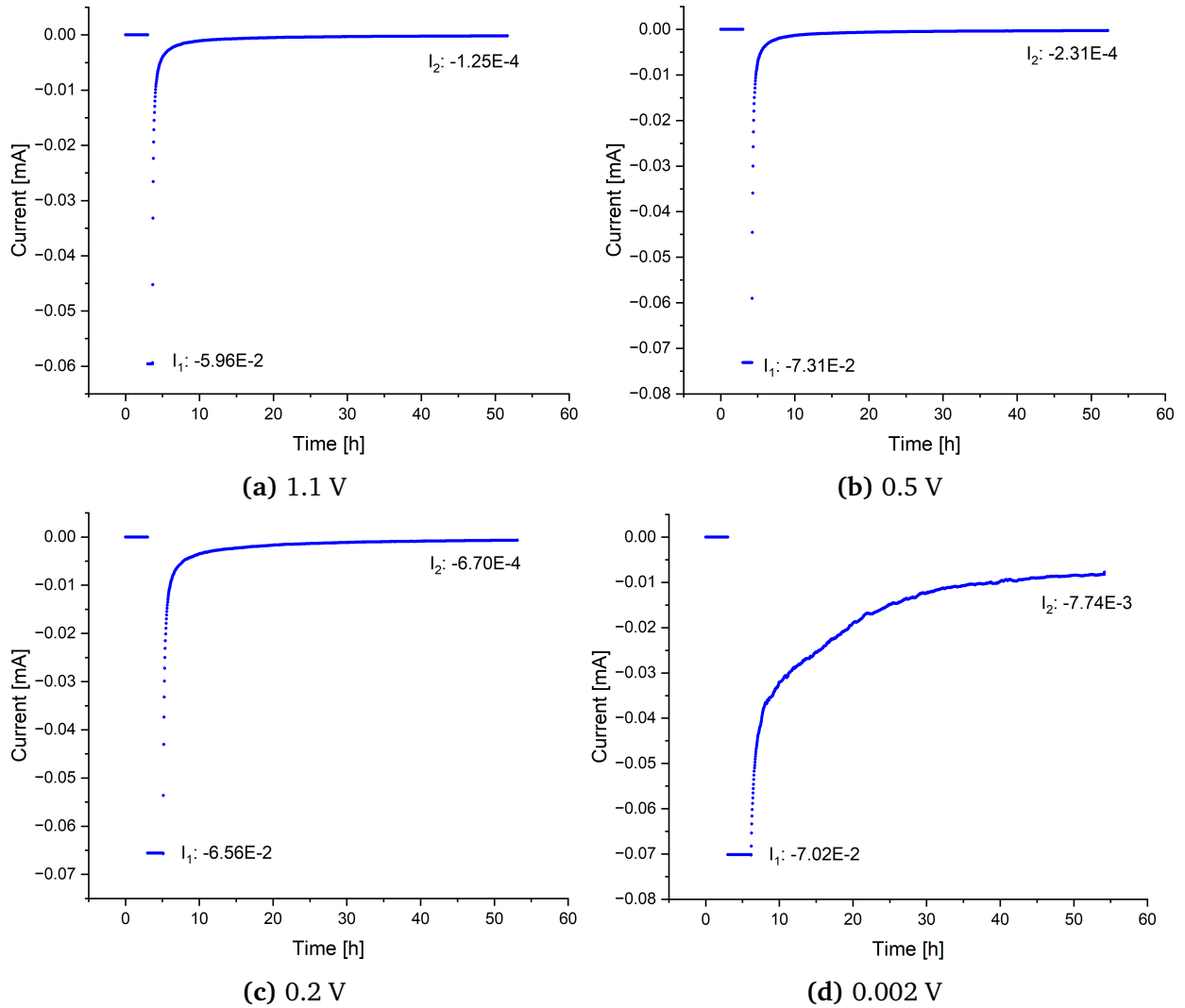
Figure 4.7: Current vs time plots for the 1st lithiation of the cells stopped at 1.1 V, 0.5 V, 0.2 V and 0.002 V. I$_1$ and I$_2$ are the measured currents at the start and end of the potential hold, respectively.

4.4 Compositional analysis

XPS measurements were performed in order to gain knowledge on voltage-dependent chemical changes in SiO_2 anodes during early lithiation/delithiation cycles, with the aim of tracking SiO_2 conversion to electroactive Si domains, lithium silicates and lithium oxide species. The voltage profiles of the initial and subsequent lithiation cycles, as well as the initial delithiation and fourth delithiation cycle, are depicted in Fig. 4.8. A circular marker displays the potential at which the cell was stopped and held for XPS measurements. This figure is included in the representation of the depth profile XPS plots. Depth profile characterisations were performed to gain information about the top and subsurface layers on the electrode. Section 4.4.1 displays XPS depth profiles of Si 2p, O 1s, C 1s and F 1s, at different states of charge and discharge. Section 4.4.2 depicts XPS spectra at the selected potentials at zero and 90 seconds etching. While section 4.4.3 presents the survey scans at different potentials.
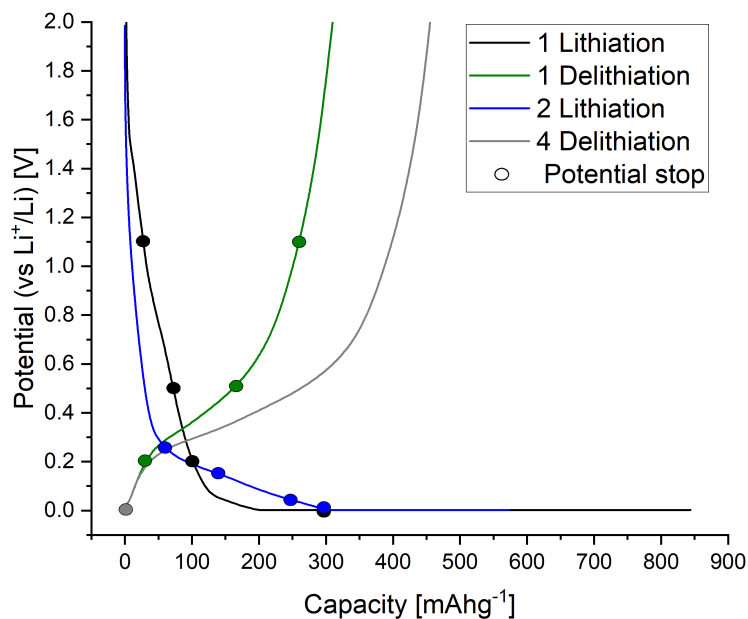
Figure 4.8: First lithiation/delithiation cycle, second lithiation and fourth delithiation cycle of the SiO_2 electrode cycled between 2 V and 0.002 V at 50 mAg^{-1}. The samples analysed by XPS are highlighted by coloured points.

4.4.1 High-resolution spectra with depth profile

The XPS depth profile plots are arranged in columns that correspond to the element of interest with corresponding fits (Si 2p, O 1s, C 1s and F 1s) and in rows corresponding to the etching time (0, 30, 60 and 90 seconds). The literature binding energies of all relevant compositions are shown in Table. 2.7. The main fitted peaks are coloured with the following colour coding: SiO$_2$ is purple, Li$_x$SiO$_y$ is green, Si blue, Li$_2$O is yellow, Li$_2$CO$_3$ is dark blue, C-C is grey, CB is black, LiPF$_6$ is dark green and LiF is light green. The LiPF$_6$ peak corresponds to the binding energy of the P-F bond.

First lithiation

Fig. 4.9a displays the voltage point during the first lithiation cycle at which the cell was halted, whereas Fig. 4.9b exhibits the initial specific capacity at 1.1 V, which was measured to be 31 mAhg^{-1}. After applying the potential hold for 48 h, the capacity increased to 65 mAhg^{-1}, as indicated in the same figure. Fig. 4.9c showcases the XPS spectra for Si 2p, O 1s, C 1s, and F 1s, and their corresponding fits, after the 48 h voltage hold at 1.1 V during the first lithiation cycle.

  The Si 2p spectra display a main peak corresponding to SiO$_2$. Although minor changes are observed in the spectra after etching, some weak signals from Li$_x$SiO$_y$ can be identified. The O 1s spectra also exhibit the highest signal that corresponds to SiO$_2$, with additional signals attributed to Li$_2$CO$_3$ visible after 30 seconds of etching. A signal from Li$_x$SiO$_y$ is also evident in the O 1s spectra. After etching, a weak signal from Li$_2$CO$_3$ can be seen in the C 1s spectrum. The F 1s spectra reveal two peaks, one assigned to LiF and another assigned to LiPF$_6$.

  Fig. 4.10a displays the voltage value during the first lithiation cycle at which the cell was halted, whereas Fig. 4.10b exhibits the initial specific capacity at 0.5 V, which was measured to be 61 mAhg^{-1}. After applying the potential hold for 48 h, the capacity increased to 95 mAhg^{-1}. Fig. 4.10c showcases the XPS spectra for Si 2p, O 1s, C 1s, and F 1s, and their corresponding fits, after the 48 h voltage hold at 0.5 V during the first lithiation cycle.

  The Si 2p and F 1s spectra at 0.5 V look very similar to the 1.1 V spectra. The main change is that the Li$_2$CO$_3$ peak has increased in both O 1s and C 1s spectra, but the peak is not dominant compared to SiO$_2$ or C—C peak. Additionally, the signal from Li$_x$SiO$_y$ is more prominent in the O 1s spectra compared to the Si 2p spectra.
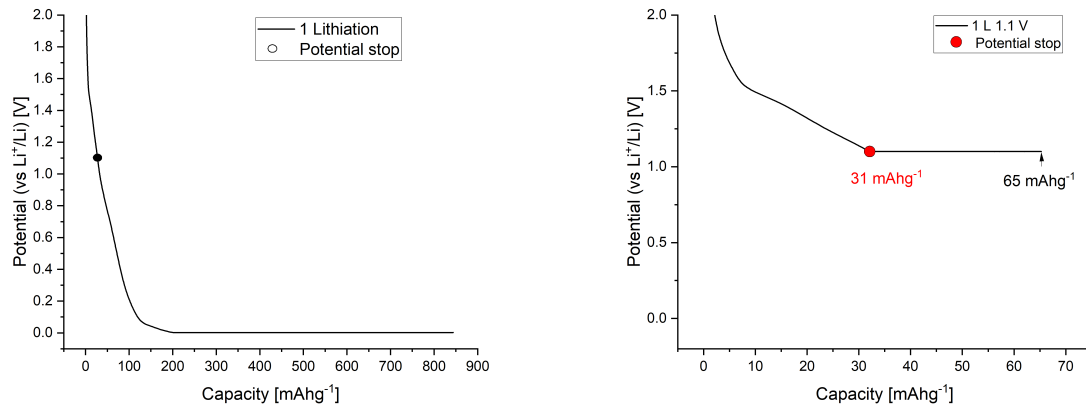
(a) Overview of first lithiation curve with the potential stop of the cell.

(b) Lithiation curve, the red dot indicates the potential stop, then holding step for 48 hours.
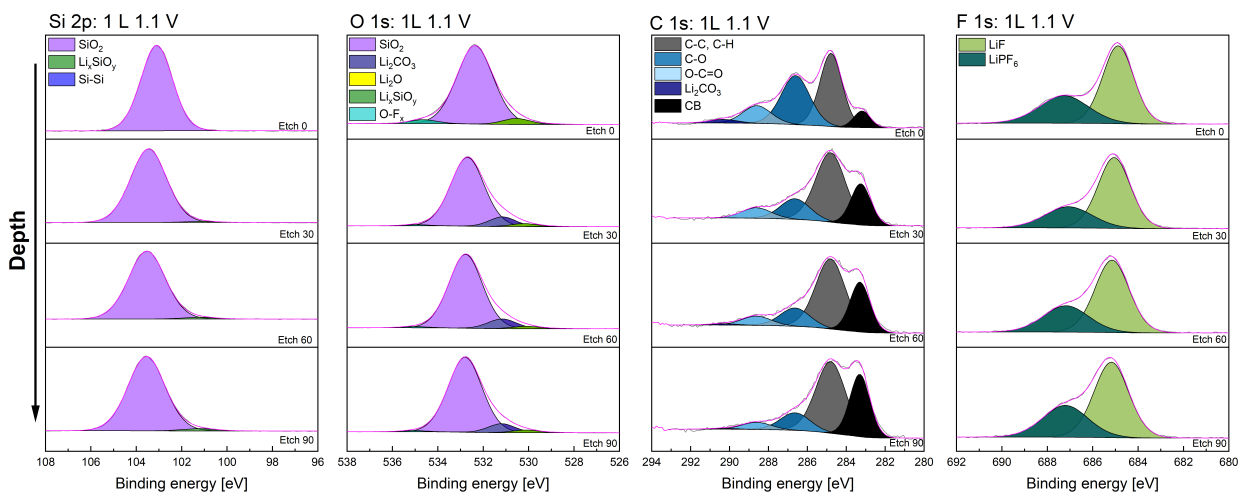
(c) XPS results from SiO$_2$ anode cycled until 1.1 V on the first lithiation cycle. Left to right: spectra of Si 2p, O 1s, C 1s and F 1s corresponding to etching times of 0, 30, 60 and 90 seconds (top to bottom).

Figure 4.9: First lithiation cycled cell stopped at 1.1 V.

(a) Overview of first lithiation curve with the potential stop of the cell.

(b) Lithiation curve, red dot indicates the potential stop, then holding step for 48 hours.

(c) XPS results from SiO$_2$ anode cycled until 0.5 V on the first lithiation cycle. Left to right: spectra of Si 2p, O 1s, C 1s and F 1s corresponding to etching times of 0, 30, 60 and 90 seconds (top to bottom).

Figure 4.10: First lithiation cycled cell stopped at 0.5 V.

Fig. 4.11a displays the voltage value of 0.2 V during the first lithiation cycle at which the cell was halted, whereas Fig. 4.11b exhibits the initial specific capacity at 0.2 V, which was measured to be 105 $mAhg^{-1}$. At this stage, the potential hold step of 48 h increased the capacity to 180 $mAhg^{-1}$. Fig. 4.11c showcases the XPS spectra for Si 2p, O 1s, C 1s, and F 1s, and their corresponding fits, after the 48 h voltage hold at 0.2 V during the first lithiation cycle.

The Si 2p spectra exhibit a similar trend to the previous potentials. While the O 1s and C 1s spectra show a Li_2CO_3 peak at all etching times, including 0 etching. The Li_xSiO_y peak has a similar shape as previous potentials. The CB peak is almost not visible at 0 etching and has an increasing but lower signal compared to previous potentials.

Fig. 4.12a displays the voltage value of 0.002 V of the first lithiation cycle at which the cell was stopped to perform XPS analysis. As it can be seen from Fig. 4.12, the initial capacity of 158 $mAhg^{-1}$ is increased to 726 $mAhg^{-1}$ after holding the potential for 48 h, which is a capacity increase of 5 times. Fig. 4.12c showcases the XPS spectra for Si 2p, O 1s, C 1s, and F 1s, and their corresponding fits, after the 48 h voltage hold at 0.002 V during the first lithiation cycle.

In this case, the signal-to-noise ratio corresponding to the Si 2p spectra is much lower compared with previous datasets. However, three main components can be identified. At the top layer (0 etch), the main peak corresponds to SiO_2 species, and a signal attributed to Li_xSiO_y and Si-Si can also be identified, although with a significantly lower peak area. Interestingly, a larger proportion of these two last components can be observed at increasing etching times. Within Li_xSiO_y and Si-Si, the signal of Li_xSiO_y shows a more significant increase after 90 seconds of etching time. In the O 1s spectra, the main signal corresponds to the Li_2CO_3 component, followed by SiO_2. Other chemical species present are Li_2O, Li_xSiO_y and $O-F_x$. Increasing etching times result in the disappearance of $O-F_x$ species, a decrease of SiO_2 signal and an increase of the signal corresponding to Li_xSiO_y and Li_2O. In the C 1s spectra, Li_2CO_3 species is increasing with etching time. The CB signal has the highest signal deepest in the sample.
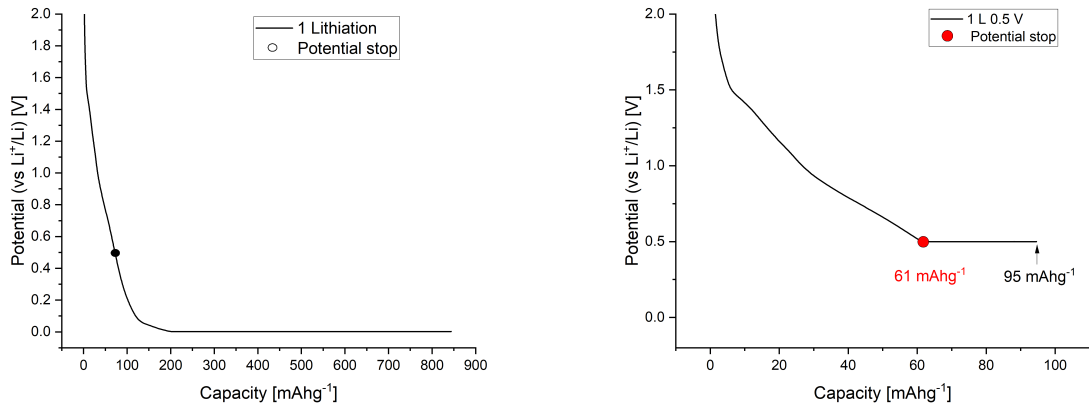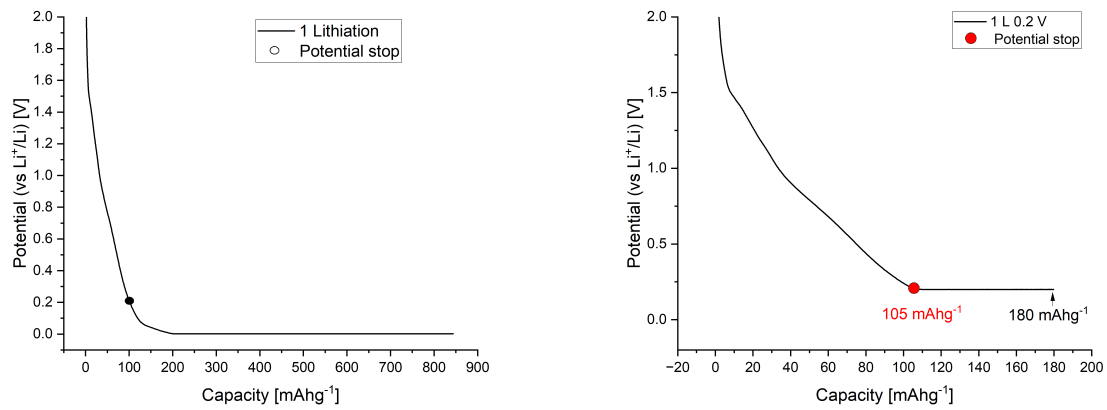
(a) Overview of first lithiation curve with the potential stop of the cell.

(b) Lithiation curve, red dot indicates the potential stop, then holding step for 48 hours.
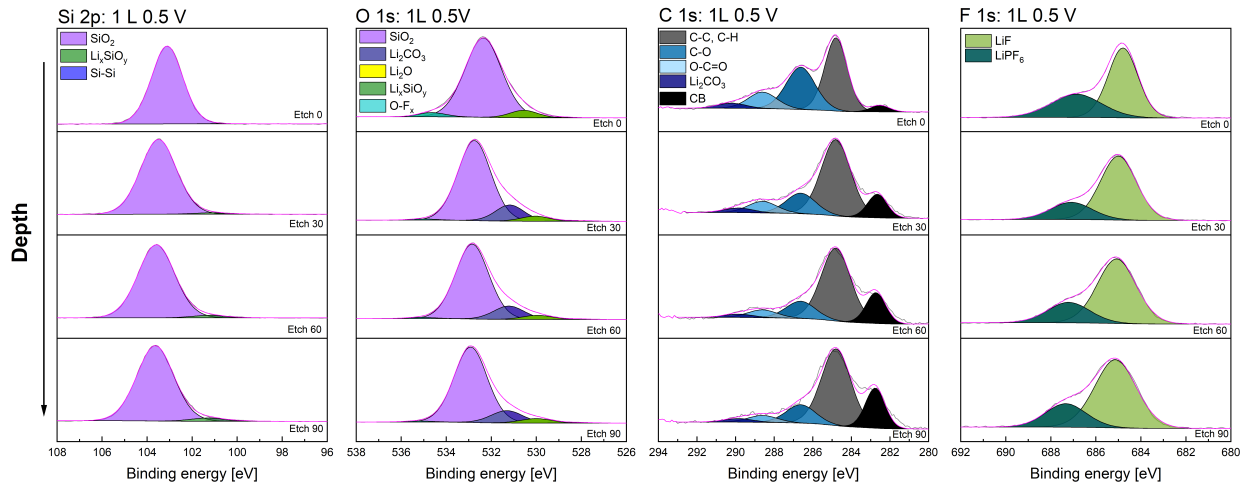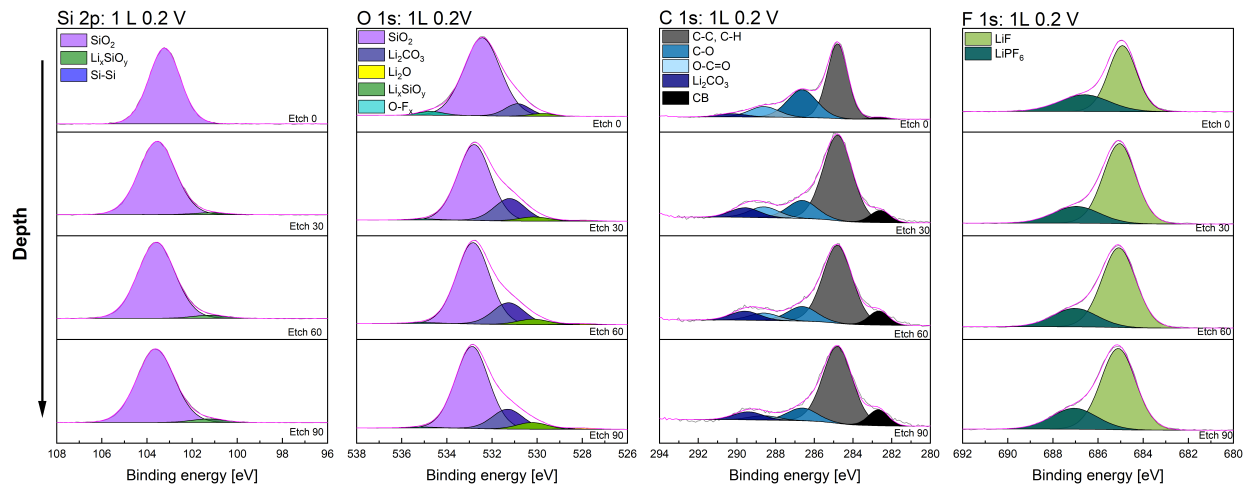

(c) XPS results from SiO$_2$ anode cycled until 0.2 V on the first lithiation cycle. Left to right: spectra of Si 2p, O 1s, C 1s and F 1s corresponding to etching times of 0, 30, 60 and 90 seconds (top to bottom).

Figure 4.11: First lithiation cycled cell stopped at 0.2 V.

(a) Overview of first lithiation curve with the potential stop of the cell.

(b) Lithiation curve, red dot indicates the potential stop, then holding step for 48 hours.

(c) XPS results from SiO$_2$ anode cycled until 0.002 V on the first lithiation cycle. Left to right: spectra of Si 2p, O 1s, C 1s and F 1s corresponding to etching times of 0, 30, 60 and 90 seconds (top to bottom).

Figure 4.12: First lithiation cycled cell stopped at 0.002 V.

First delithiation

In this case, the lithiated cell was delithiated until reaching 0.2 V as shown in Fig. 4.13a. The specific capacity at this voltage value is 24 mAhg^{-1}, and this value increased to 33 mAhg^{-1} after holding the potential for 48 h, Fig. 4.13b.

In the Si 2p spectra, 4.13c, it can be observed that the partially delithiated electrode is composed mainly of SiO$_2$. Again, the signal-to-noise ratio in this spectra is low. At 0 etching time, the signal corresponding to Li$_x$SiO$_y$ and Si-Si is very weak, and the Li$_x$SiO$_y$ signal increases notably with increasing etching times. The O 1s spectra show a similar amount of SiO$_2$ for all the etching times. The Li$_2$O signal is not visible at 0 etching but is visible after etching, and increases with etching time. A very small amount of Li$_x$SiO$_y$ signal is present. In the C 1s spectra Li$_2$CO$_3$ is the dominant peak after 30 seconds etching. At 0 etching the signal is very poor, but after 30 seconds of etching the signal is very prominent. CB is almost not visible in any of the C 1s spectra.

Fig. 4.14a displays the voltage value of 0.5 V where the delithiated cell was halted to perform XPS analysis. As it can be seen from Fig. 4.14, the initial capacity of 139 mAhg^{-1} is increased to 160 mAhg^{-1} after holding the potential for 48 h. Fig. 4.14c displays the XPS spectra for Si 2p, O 1s, C 1s, and F 1s, and their corresponding fits for this cell.

The Si 2p spectra still show a main peak corresponding to SiO$_2$, and the Li$_x$SiO$_y$ amount increases with etching time. In the O 1s spectra, the Li$_x$SiO$_y$ are also visible after etching. Li$_2$O species is visible after 30 seconds of etching and has a higher signal with increasing etching time. The C 1s spectra have a similar trend as the previous potential at 0.2 V, except that the CB signal is more visible.

The last sample investigated during delithiation is stopped at 1.1 V, as depicted in 4.15a. Here, the cell has an initial specific capacity of 218 mAhg^{-1}, which increases to 251 mAhg^{-1}, Fig. 4.15b. The Si 2p spectra, Fig. 4.15c, shows a different trend than for the previous potentials during delithiation, here the Li$_x$SiO$_y$ peak decreases from 30 to 90 seconds etching. In the O 1s spectra, the Li$_2$CO$_3$ peak is dominant for all etching times, and the Li$_2$O species are first visible after 30 seconds of etching. Both the SiO$_2$ and Li$_x$SiO$_y$ peak increases from 30 to 60 seconds etching. The C 1s spectrum shows an increasing CB peak as well as an increasing Li$_2$CO$_3$ peak with etching time. In the F 1s spectra the LiPF$_6$ peak has a weak signal compared to LiF, which does not show significant change with increasing etching times.
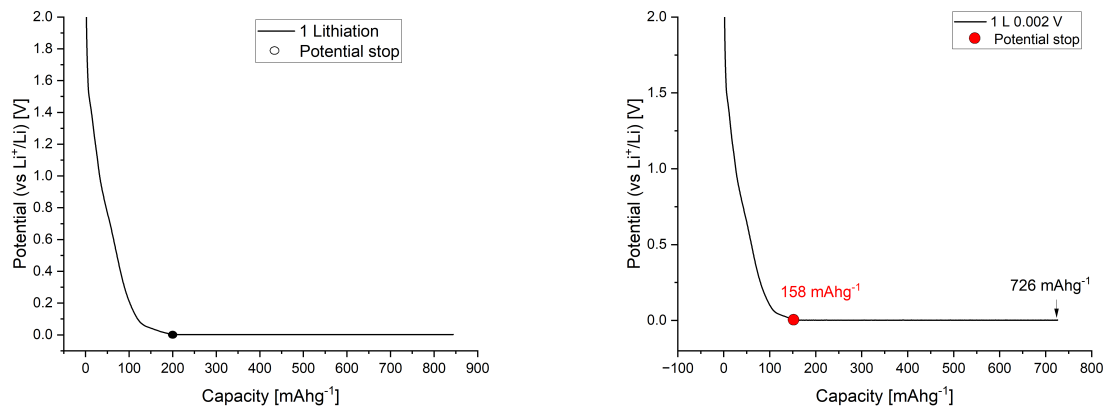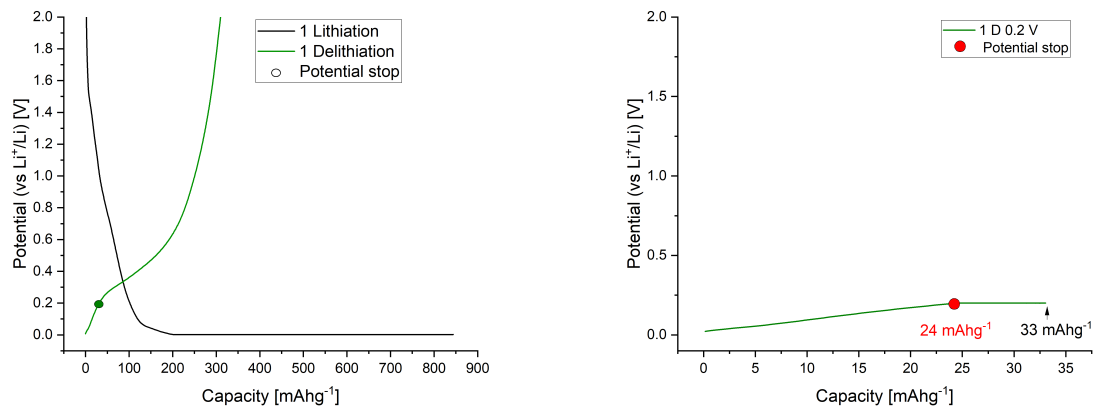
(a) Overview of first delithiation curve with the potential stop of the cell.

(b) Delithiation curve, red dot indicates the potential stop, then holding step for 48 hours.
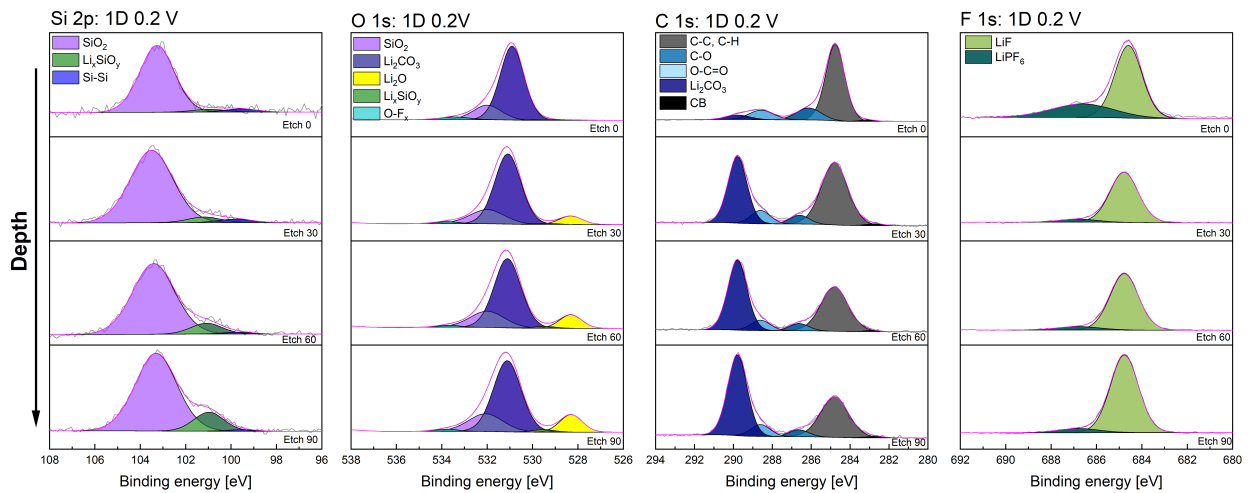
(c) XPS results from SiO$_2$ anode cycled until 0.2 V on the first delithiation cycle. Left to right: spectra of Si 2p, O 1s, C 1s and F 1s corresponding to etching times of 0, 30, 60 and 90 seconds (top to bottom).

Figure 4.13: First delithiation cycled cell stopped at 0.2 V.
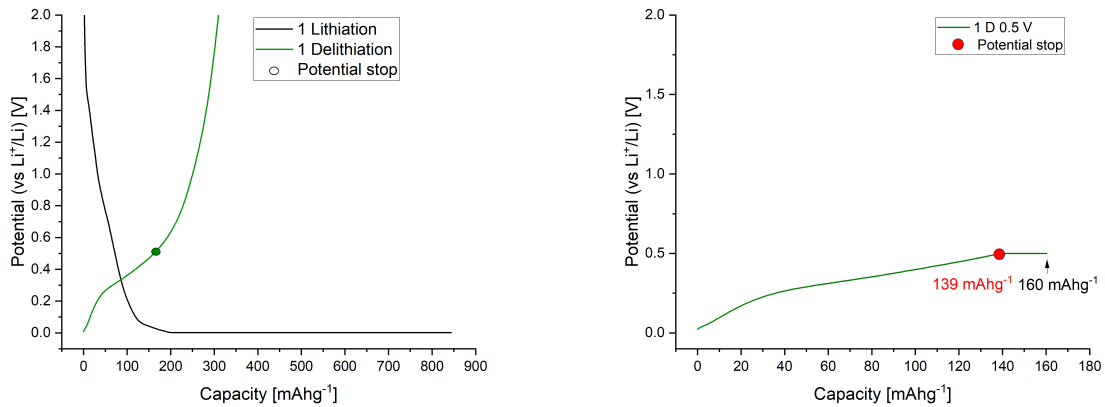
(a) Overview of first delithiation curve with the potential stop of the cell.

(b) Delithiation curve, red dot indicates the potential stop, then holding step for 48 hours.
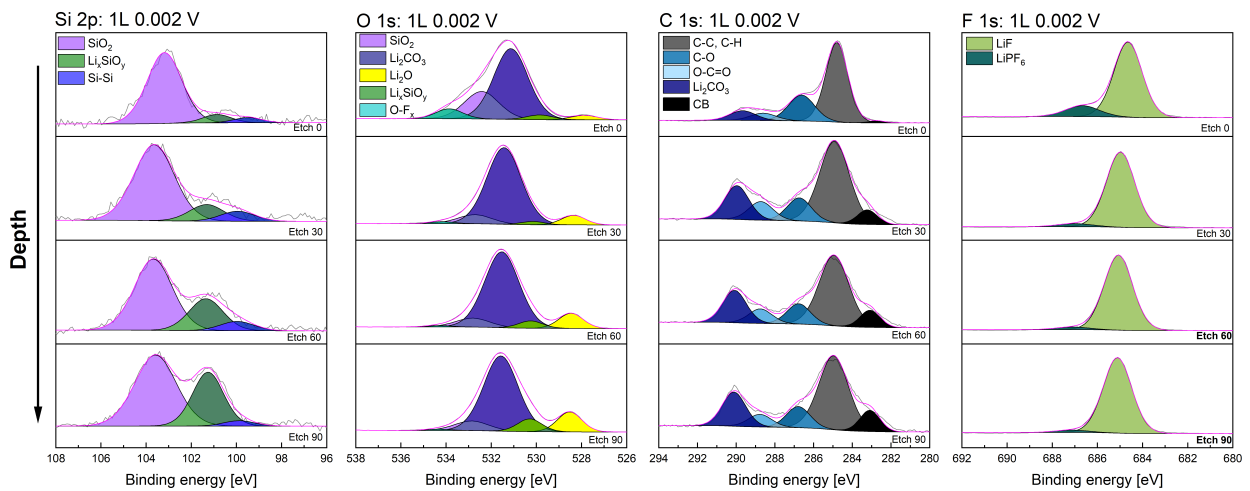

(c) XPS results from SiO$_2$ anode cycled until 0.5 V on the first delithiation cycle. Left to right: spectra of Si 2p, O 1s, C 1s and F 1s corresponding to etching times of 0, 30, 60 and 90 seconds (top to bottom).

Figure 4.14: First delithiation cycled cell stopped at 0.5 V.

(a) Overview of first delithiation curve with the potential stop of the cell.

(b) Delithiation curve, red dot indicates the potential stop, then holding step for 48 hours.

(c) XPS results from SiO_2 anode cycled until 1.1 V on the first delithiation cycle. Left to right: spectra of Si 2p, O 1s, C 1s and F 1s corresponding to etching times of 0, 30, 60 and 90 seconds (top to bottom).

Figure 4.15: First delithiation cycled cell stopped at 1.1 V.

Second lithiation

Fig. 4.16a displays the voltage point during the second lithiation cycle at which the cell was halted. Fig. 4.16b exhibits the initial specific capacity at 0.25 V, measured to be 55 mAhg^{-1}. At this stage, the potential hold of 48 h increased the capacity to 115 mAhg^{-1}. Fig. 4.16c shows the XPS spectra for Si 2p, O 1s, C 1s, and F 1s, and their corresponding fits, after the 48 h voltage hold at 0.25 V during the second lithiation cycle. In the Si 2p spectra, Li$_x$SiO$_y$ is present, and the peak area increases slightly with etching time. Conversely, in the O 1s spectra, the Li$_x$SiO$_y$ species are not visible until 60 seconds of etching and exhibit a low peak intensity. The SiO$_2$ peak looks similar deeper in the sample, but Li$_2$O is barely visible before etching and has a slight increase in intensity deeper in the sample. As etching time increases, the C 1s spectrum shows a decreasing C-C peak and an increasing Li$_2$CO$_3$ peak. The LiF signal in the F 1s spectra increases with etching time.

The next cell was stopped at 0.15 V, Fig. 4.17a. In this case, the capacity increased from 115 mAhg^{-1} to 179 mAhg^{-1} after the potential hold of 48 h, Fig. 4.17b. Looking at the XPS spectra depicted in Fig. 4.17c, the SiO$_2$ signal decreases with etching time, while the Li$_x$SiO$_y$ signal increases. At both 0 and 30 seconds of etching, a weak Si-Si signal is observed. The Li$_x$SiO$_y$ signal in the O 1s spectra is only visible at 90 seconds of etching. The C 1s spectra show a similar trend as the previous 0.25 V spectra.

Fig. 4.18a shows the second lithiation cycle at which the cell was halted at 0.04 V. The specific capacity increased from 206 mAhg^{-1} to 328 mAhg^{-1} after 48 h of potential hold, as seen in 4.18b. In Fig. 4.18c, the main peak in the Si 2p signal is assigned to SiO$_2$. However, a signal from Si-Si is visible at both 0 and 60 seconds of etching. The amount of Li$_x$SiO$_y$ increases slightly with longer etching times. The O 1s spectra also show a small SiO$_2$ peak and no visible Li$_x$SiO$_y$ peak, but dominant signals are observed from Li$_2$CO$_3$ and Li$_2$O. The C 1s spectra only exhibit a visible CB peak at 30 seconds of etching, while the peak with the highest intensity during etching is attributed to Li$_2$CO$_3$. The F 1s spectra have a minimal signal from LiF and LiFP$_6$.

Fig. 4.19a displays the voltage value of 0.002 V of the second lithiation cycle. In Fig. 4.19b there is a huge increase in specific capacity after potential hold from the initial value of 299 mAhg^{-1} to 618 mAhg^{-1}. Fig. 4.19c shows that the Si 2p spectra exhibit significant noise,

while the SiO_2 peak is prominent, and the Li_xSiO_y peak increases with etching time. The Si-Si peak shows no consistent trend but is present in all spectra. In the O 1s spectra, the SiO_2 peak is almost invisible for the etched samples, while Li_2CO_3 is the dominant peak, and Li_2O shows an increasing peak during etching. The C 1s spectra show that CB is only visible at 0 etching, and the peak with the highest intensity is Li_2CO_3, which increases with etching time. The F 1s spectra indicate more $LiPF_6$ at 0 etching, and minimal signal during etching.
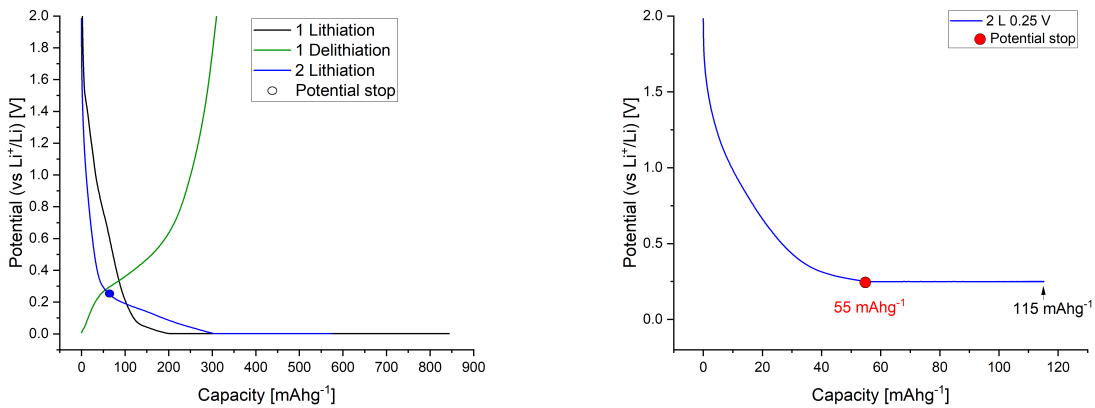
(a) Overview of second lithiation curve with the potential stop of the cell.

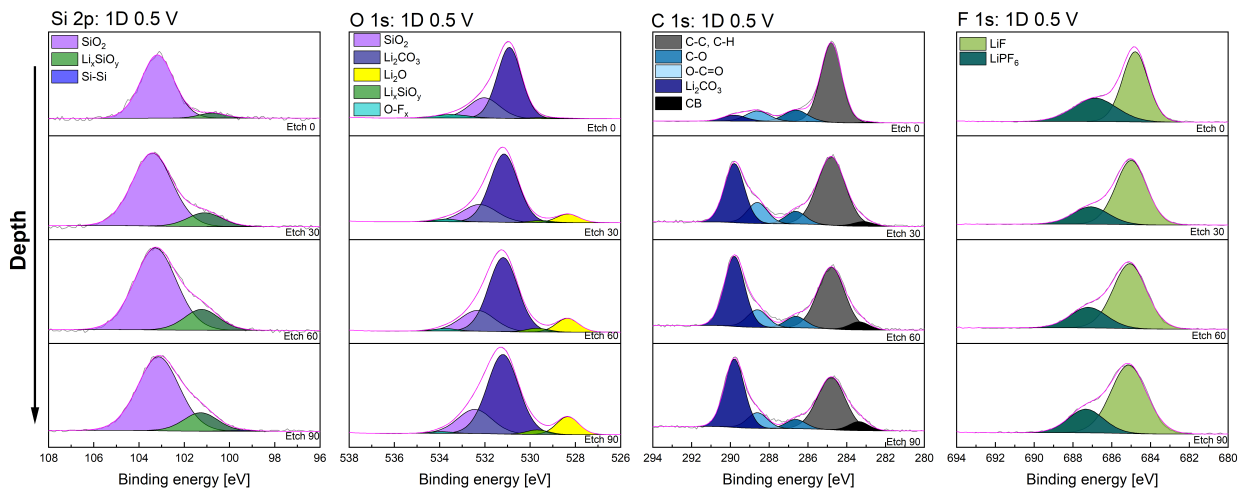**(b)** Lithiation curve, red dot indicates the potential stop, then holding step for 48 hours.
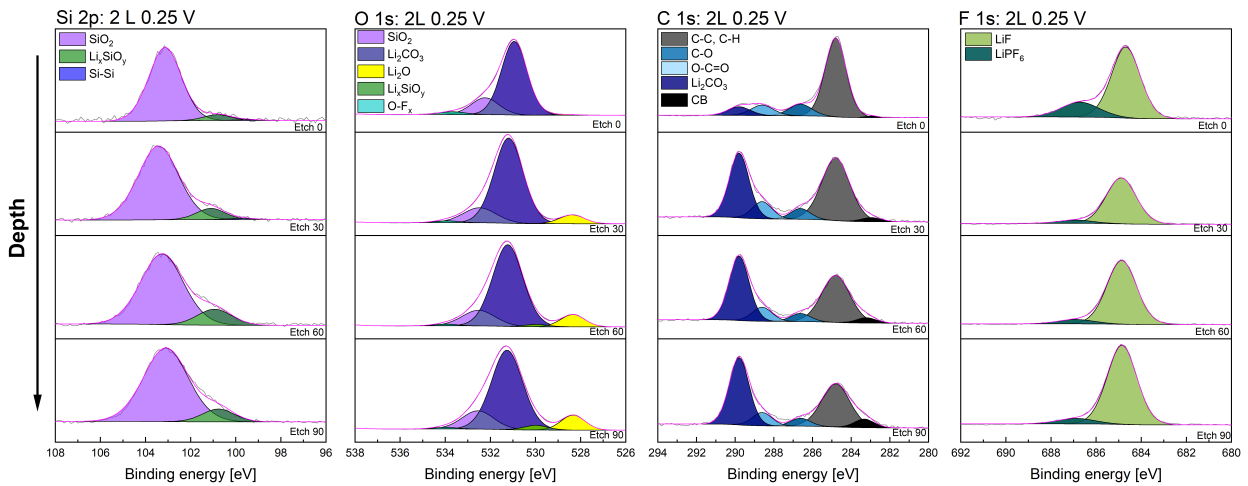
(c) XPS results from SiO_2 anode cycled until 0.25 V on the second lithiation cycle. Left to right: spectra of Si 2p, O 1s, C 1s and F 1s corresponding to etching times of 0, 30, 60 and 90 seconds (top to bottom).

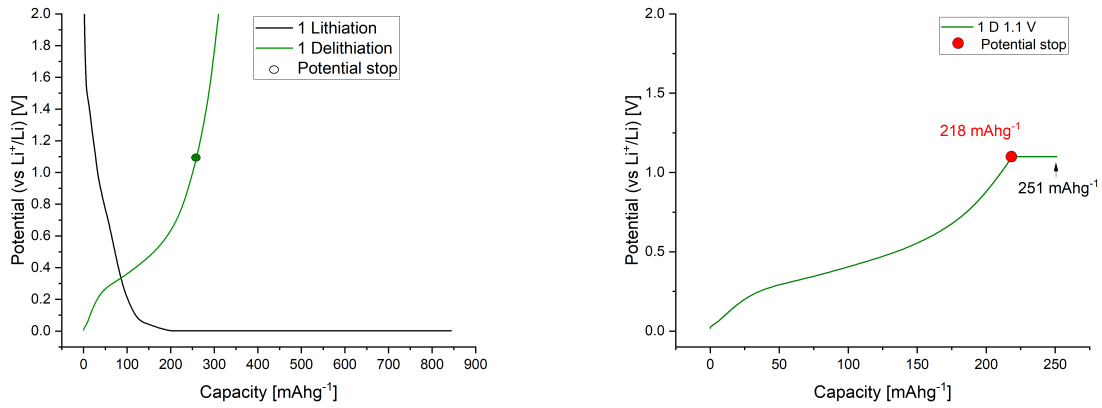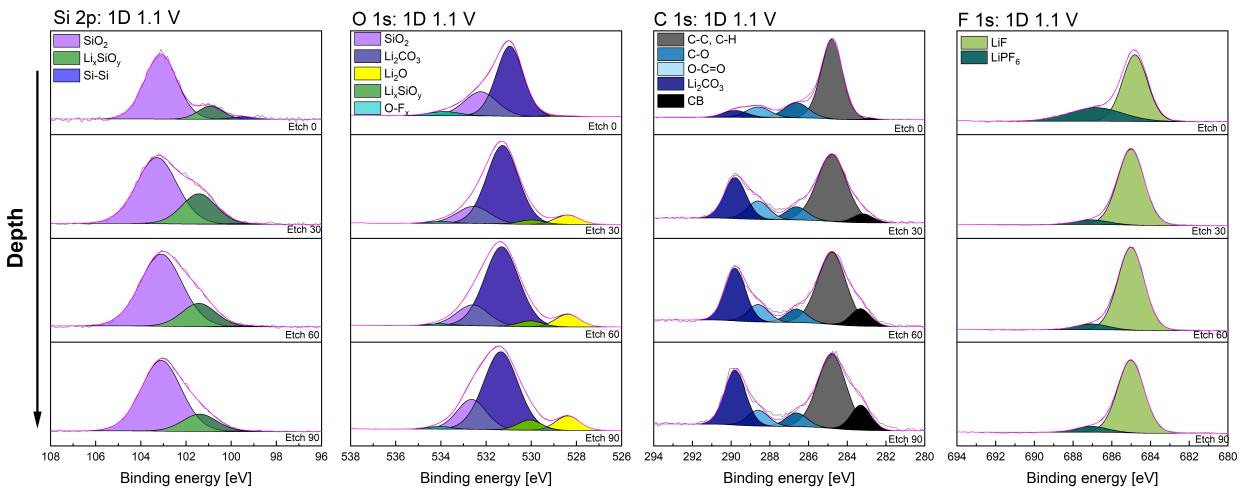**Figure 4.16:** Second lithiation cycled cell stopped at 0.25 V.
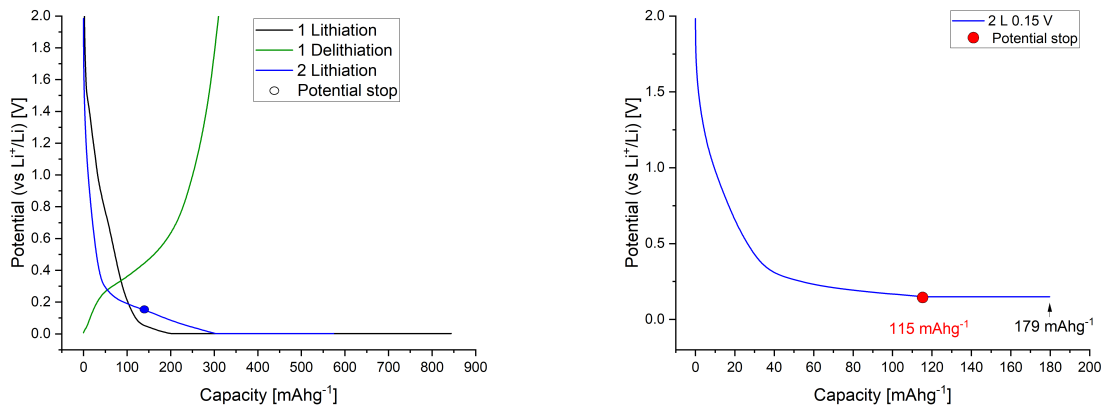
(a) Overview of second lithiation curve with the potential stop of the cell.

(b) Lithiation curve, red dot indicates the potential stop, then holding step for 48 hours.
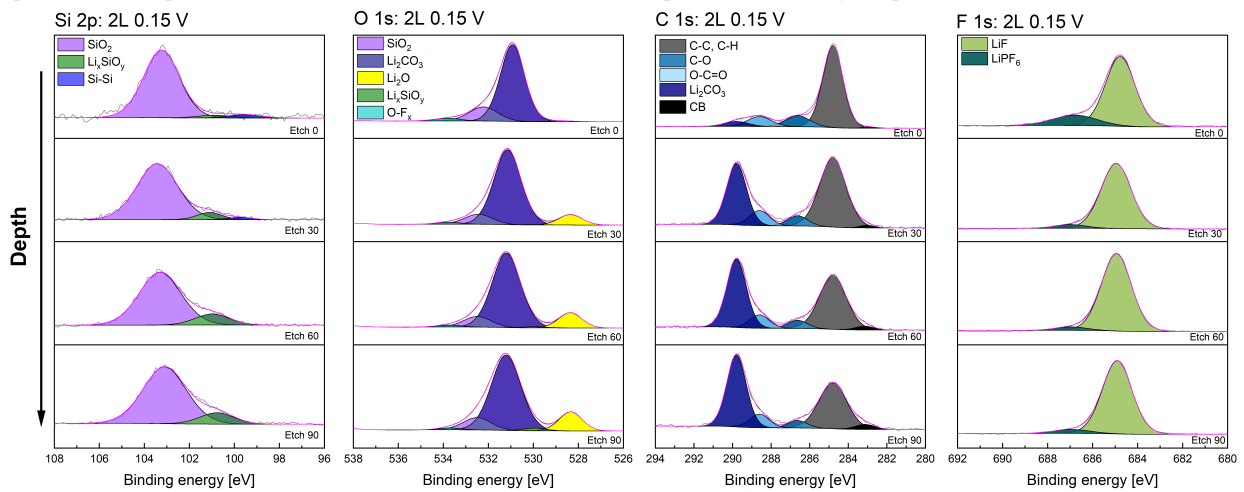
(c) XPS results from SiO$_2$ anode cycled until 0.15 V on the second lithiation cycle. Left to right: spectra of Si 2p, O 1s, C 1s and F 1s corresponding to etching times of 0, 30, 60 and 90 seconds (top to bottom).

Figure 4.17: Second lithiation cycled cell stopped at 0.15 V.
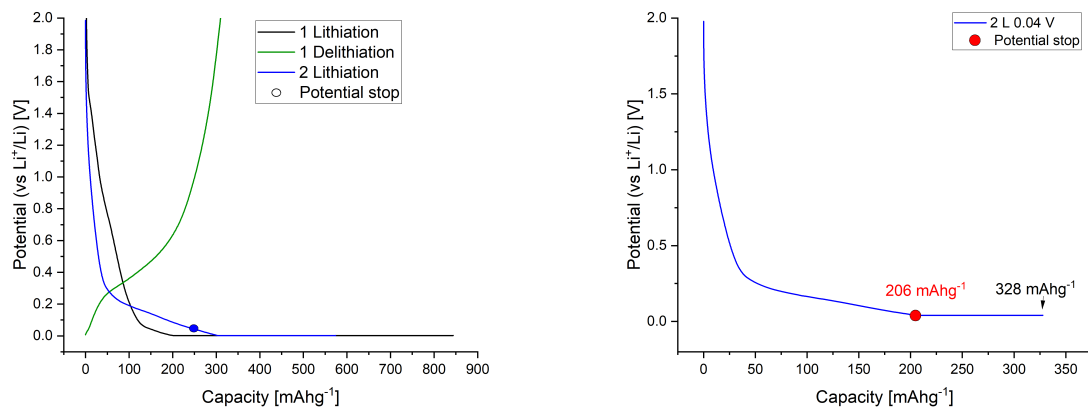
(a) Overview of second lithiation curve with the potential stop of the cell.

(b) Lithiation curve, red dot indicates the potential stop, then holding step for 48 hours.
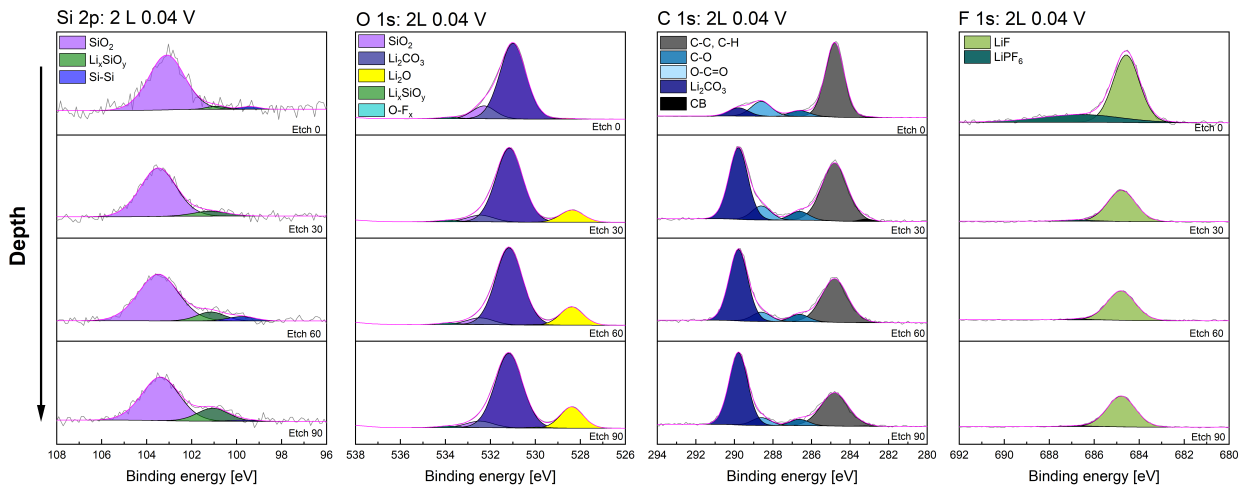
(c) XPS results from SiO_2 anode cycled until 0.04 V on the second lithiation cycle. Left to right: spectra of Si 2p, O 1s, C 1s and F 1s corresponding to etching times of 0, 30, 60 and 90 seconds (top to bottom).

Figure 4.18: Second lithiation cycled cell stopped at 0.04 V.
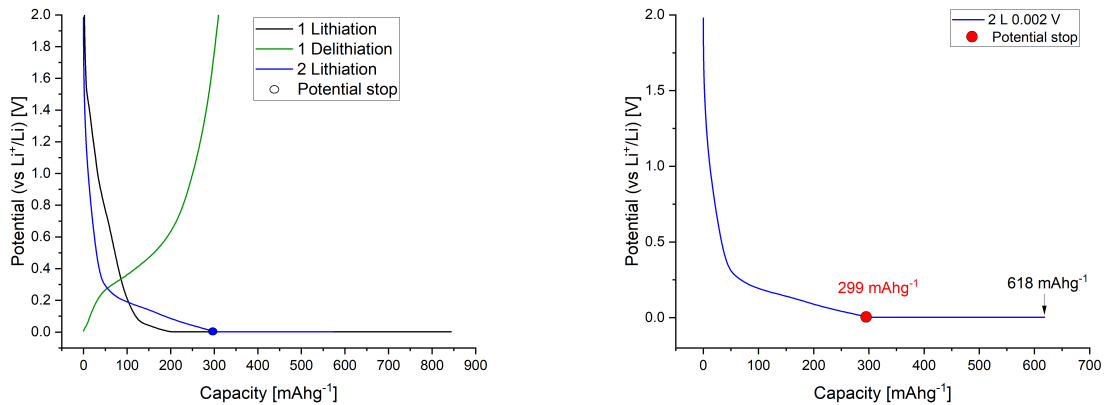
(a) Overview of second lithiation curve with the potential stop of the cell.

(b) Lithiation curve, red dot indicates the potential stop, then holding step for 48 hours.
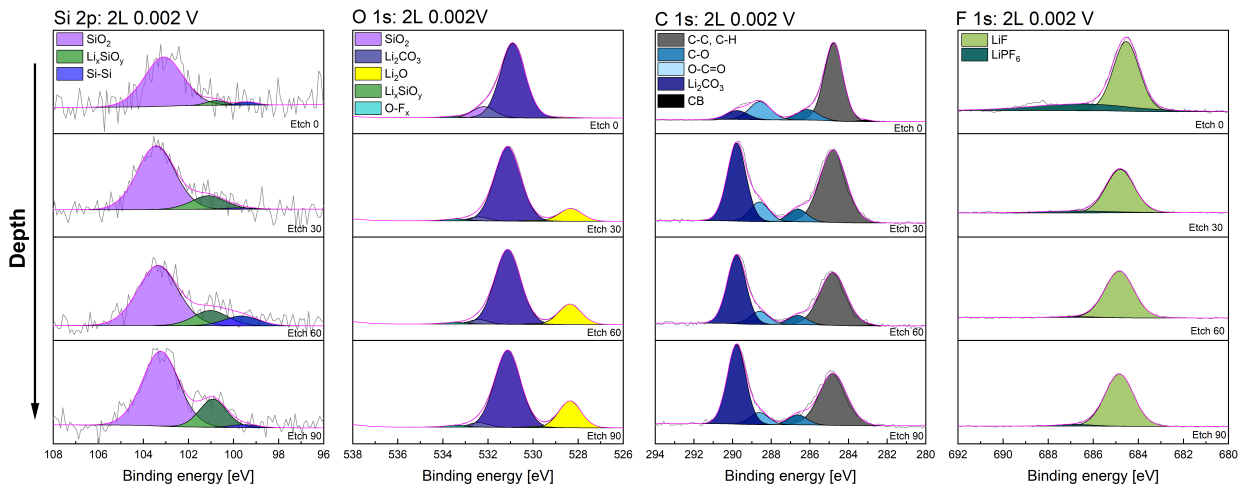
(c) XPS results from SiO_2 anode cycled until 0.002 V on the second lithiation cycle. Left to right: spectra of Si 2p, O 1s, C 1s and F 1s corresponding to etching times of 0, 30, 60 and 90 seconds (top to bottom).

Figure 4.19: Second lithiation cycled cell stopped at 0.002 V.

Fourth delithiation

The previous post-mortem XPS analysis on electrodes subjected to 1 and 2 activation cycles show a very slow reaction of SiO_2 towards Li^+. From the electrochemical data, in section 4.3.1, it can be observed that after 4 lithiation/delithiation cycles a considerable amount of Si-Si is reversibly lithiated, meaning that at that stage most of the SiO_2 has reacted. Hence, in order to reveal the final reaction products of SiO_2 reaction towards Li^+, the XPS analysis was extended to the 4th activation cycle.

Fig. 4.20 presents the high-resolution spectra of Si 2p, O 1s, C 1s and F 1s and corresponding composition analysis of a delithiated cell stopped at 2 V after 4 activation cycles. The data was collected after 0 and 20 seconds of etching, therefore most of the data is related to the top surface of the electrode.

As can be observed from the figure, the Si 2p spectra display a low signal-to-noise ratio. However, two main components are clearly observed. Li_xSiO_y and Si, can be distinguished, which indicates that after 4 lithiation/delithiation cycles, most of the SiO_2 has reacted. A small peak at the SiO_2 position was identified. Although the fitting corresponding to this peak can be attributed to the weak signal, the SiO_2 signature is also present at the O 1s spectra, which serves to corroborate its presence on the electrode. A peak corresponding to the Li_xSiO_y and Li_2CO_3 species can also be observed in the O 1s spectra. Notably, no peak corresponding to the Li_2O species is observed. Looking at the C 1s spectra, the C-C peak had the highest intensity, and some Li_2CO_3 was observed. The F 1s spectra contained both LiF and $LiPF_6$ components. From the software analysis, the area% of species Li_xSiO_y:Si were 51.4:43.1 and 63.8:31.5 for 0 and 20 seconds of etching, respectively.
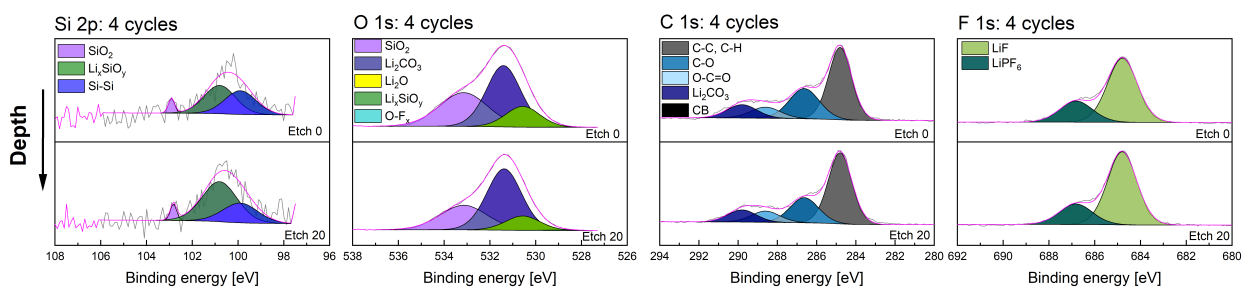
Figure 4.20: Fourth delithaition cycled cell stopped at 2 V.

Fourth delithiation - HAXPES

Fig. 4.21 corresponds to HAXPES Si 1s and O 1s spectra, conducted in the framework of the specialisation project [1]. These spectra were recorded at two different energies of the incoming beam, namely 7 and 12 keV, to generate a depth profile of the sample. Notably, the HAXPES technique yields more detailed information deeper into the sample than the XPS technique. The peak of the Si 1s spectra corresponds mainly to the binding energy of Si-Si at 1840.4 eV. Showing that SiO$_2$ is converted to Si, as predicted by the theory. There could be a shoulder corresponding to SiO$_2$, which could be SiO$_2$ remaining on the SEI. At lower binding energies there is a shoulder corresponding to Li$_x$SiO$_y$. The main peak of the O 1s spectra corresponds to Li$_2$CO$_3$. There is no distinct shoulder corresponding to Li$_2$O, however, at 12 keV it seems like Li$_2$O could be present. This could indicate that Li$_2$O is present after 4 cycles at deeper levels in the SEI. Peak fitting was not performed on the spectra since the broad nature of the peaks in the HAXPES spectra makes it challenging to accomplish using CasaXPS.
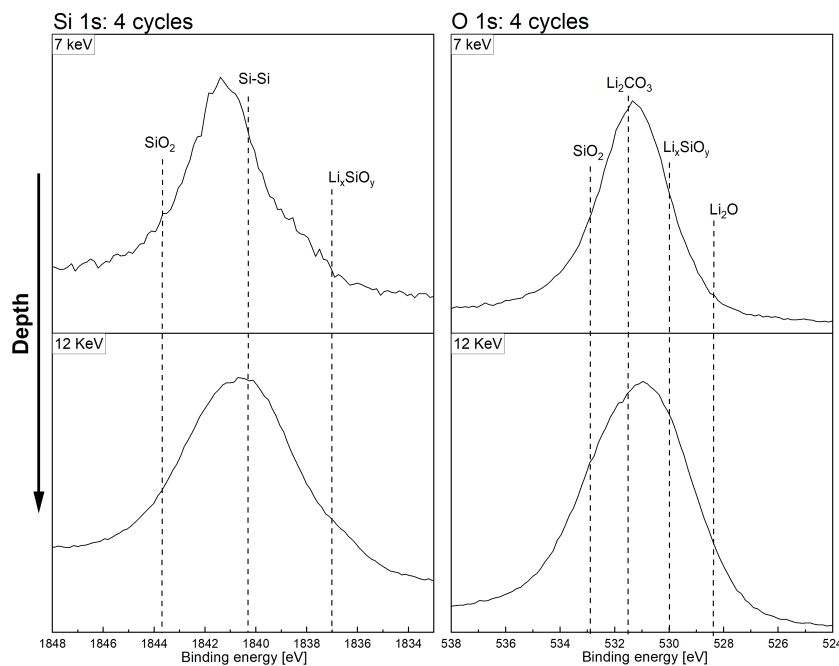
Figure 4.21: HAXPES high-resolution spectra of Si 1s and O 1s at 7 keV and 12 keV after 4 activation cycles.

4.4.2 High-resolution spectra at different potentials

1th lithiation

Fig. 4.22 displays the evolution of silicon, oxygen, carbon and fluorine signal as a function of the voltage during lithiation at 0 etching and at 90 seconds of etching. The major difference of the Si 2p signal is that the Li_xSiO_y species at 0 etching are not visible before reaching 0.002 V, while at 90 seconds etching the Li_xSiO_y have a weak signal at all of the potentials. Moreover, the Si-Si signal becomes evident at 0.002 V, and most of the Li_xSiO_y signal is observed at this voltage. The Si 2p spectra at 0.002 V are distinctly noisier than for the other potentials. Regarding the O 1s spectra, SiO_2 is the main peak at 1.1 V, 0.5 V and 0.2 V. But at 0.002 V, Li_2CO_3 has a higher intensity than SiO_2. Additionally, Li_2O first appear at 0.002 V for both the etched and un-etched spectra. The Li_xSiO_y amount increases at lower potentials. In the C 1s spectra, there is a clear trend that the CB signal decreases when lowering the potential, while the intensity of the C-C peak is stable. The Li_2CO_3 peak is highest at 0.002 V. Regarding the F 1s spectra, the peak corresponding to $LiPF_6$ decreases with charging at zero etching. The LiF peak looks relatively similar in intensity for the different voltages.
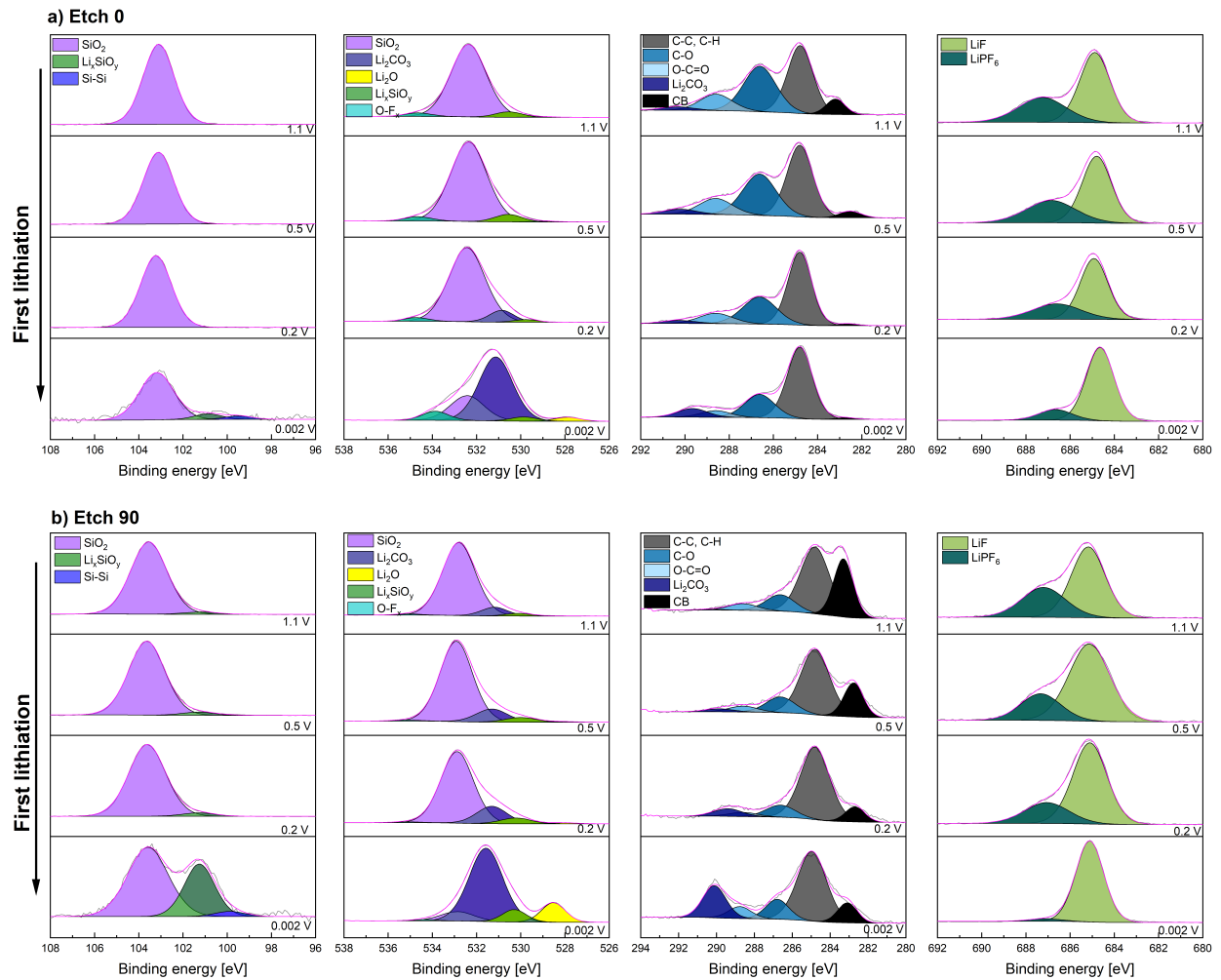
Figure 4.22: XPS spectra from first lithiation cells at different potentials with 0 and 90 seconds etching time shown in a) and b), respectively.

1th delithiation

Fig. 4.23 displays the evolution of Si 2p, O 1s, C 1s and F 1s signal as a function of the voltage during the first delithiation at 0 etching and at 90 seconds of etching. The Si 2p spectra corresponding to the non-etched electrode show a low signal-to-noise ratio at 0.2 V, which increases as the delithiation potential increases to 1.1 V. Although the main component on the spectra corresponds to SiO_2, the presence of Li_xSiO_y species is also observed. The Si-Si signal is, however, barely visible. After 90 seconds of electrode etching, the Li_xSiO_y signal is more significant. It must be remarked that this notable increase in the Li_xSiO_y species compared with 0 etching time is consistent with the appearance of a significant amount of Li_2O in the O 1s spectra, which was not present on the non-etched sample. Also, the Li_xSiO_y signal on the O 1s spectra is more preponderant after etching. Both Li_xSiO_y and Li_2O are reaction products of SiO_2 lithiation. There is a big difference in the peak intensity of Li_2CO_3 in the C 1s spectra. At 0 etching there is a weak and consistent signal at the different potentials, but at 90 seconds etching Li_2CO_3 has the highest peak intensity and the peak decreases with increasing signal. Additionally, the CB signal increases with increasing potential. The peaks from F 1s spectra has more signal from $LiPF_6$ at 0 etching than at 90 seconds of etching.
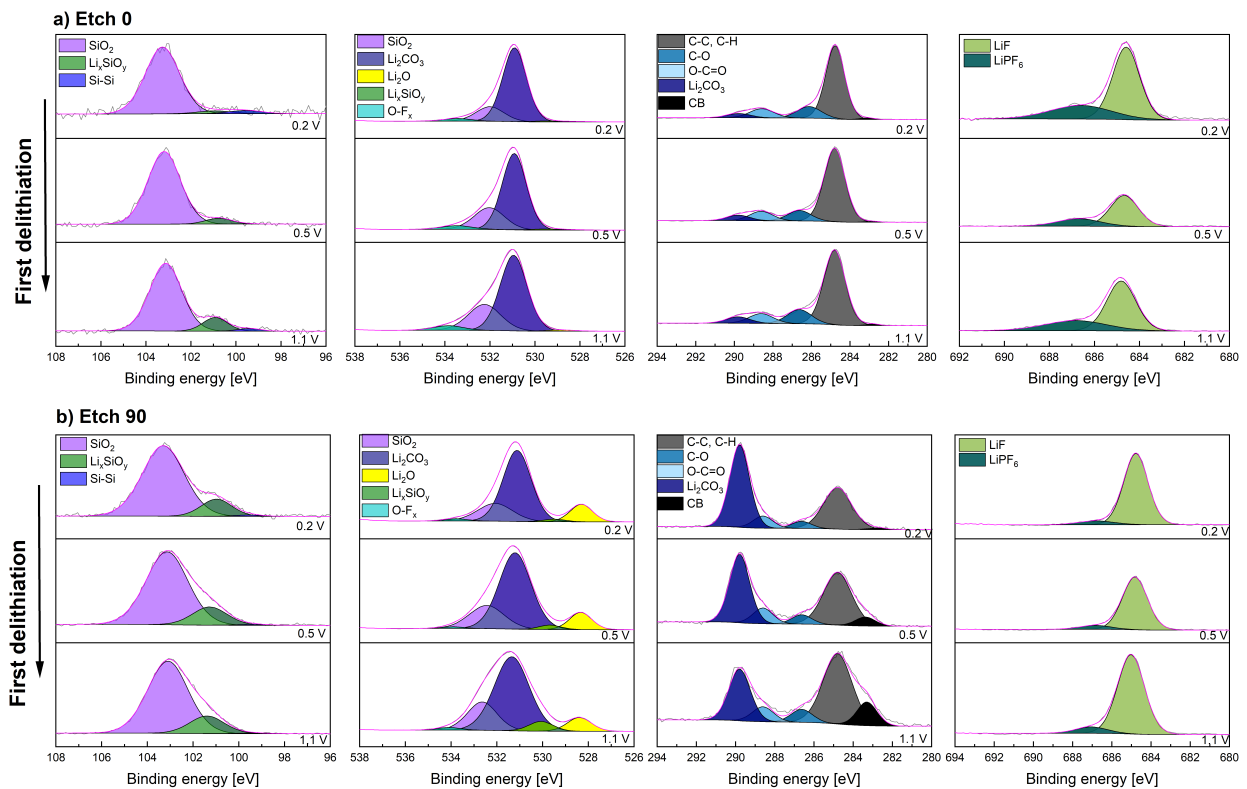
Figure 4.23: XPS spectra from first delithiation cells at different potentials with 0 and 90 seconds etching time shown in a) and b), respectively.

2$^{\text{nd}}$ lithiation cycle

Fig. 4.24 displays the evolution of Si 2p, O 1s, C 1s and F 1s signal as a function of the voltage during the second lithiation at 0 etching and at 90 seconds of etching. The Si 2p spectra exhibit a considerably low signal-to-noise ratio, particularly at the lowest potentials (0.04 and 0.002V), which might be indicative of a thicker SEI deposited on top of the active material. Interestingly, the contribution from Si-Si is minimal in all spectra. At 90 seconds of etching, both SiO_2 and Li_xSiO_y are detectable, whereas the spectra from zero seconds of etching predominantly show the signal from SiO_2. However, it should be mentioned that although SiO_2 is one of the main species, its relative amount on the probed surface is significantly lower in comparison with the first lithiation cycle. This will be presented in the next section, where results from survey scans are shown.

The O 1s spectra at 0 seconds of etching are very similar for all potentials, here the main peak is Li_2CO_3 and the other peak is attributed to SiO_2. However, at 90 seconds of etching, all potentials have a signal attributed to Li_2O. At 0.25 V the spectra have a small Li_xSiO_y peak. This peak decreases when the potential is lowered to 0.15 V, and at lower potentials (0.04 and 0.002 V) the peak has disappeared. Furthermore, the SiO_2 peak in the spectra decreases with potential, and at 0.002 V the peak is almost not detectable. There are no big changes in the C 1s spectra at 0 seconds of etching. Here C-C is the dominant peak, some Li_2CO_3 is observed and there is a negligible signal present from CB. However, at 90 seconds of etching there is a peak from CB at 0.25 V. This peak decreases at lower potentials and vanishes at 0.002 V. Meanwhile, the peak of Li_2CO_3 grows slightly as the potential is lowered. The peaks from C-O and O-C=O do not change much at different potentials. In the F 1s spectra (0 and 90 seconds of etching), LiF peak intensity decreases with voltage decrease.
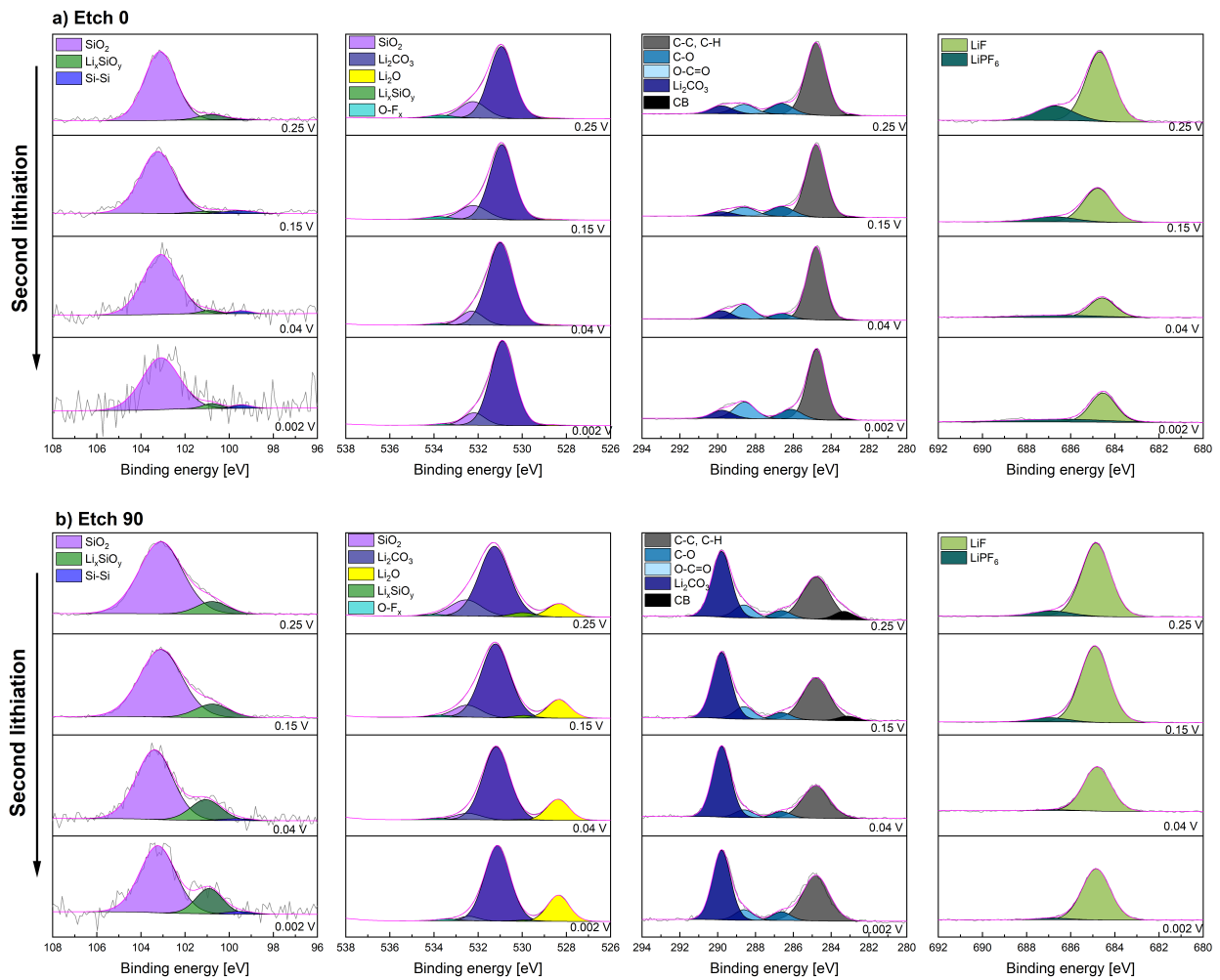
Figure 4.24: XPS spectra from second lithiation cells at different potentials with 0 and 90 seconds etching time shown in a) and b), respectively.

4.4.3 Survey scans

Survey scan spectra at 0 and 90 seconds etching made it possible to analyse the atomic% of each element in the electrodes during lithiation and delithiation. Fig. 4.25 shows the whole atomic composition evolution of the SiO_2 anode at different potentials during the first and half second cycle at 0 and 90 seconds of etching, Fig. 4.25a and Fig. 4.25b, respectively. Fig. 4.26 shows the evolution of the total amount of silicon of the sample upon the first lithiation/delithiation and second lithiation at 0 and 90 seconds of etching. The survey scans from 0 etching provide information about the top layer of the electrode. While the survey scan detected after 90 seconds of etching reveals information closer to the particle.

From the survey scan the pristine SiO_2 anode consist of Si, C, O, F, P and Na. The Na amount comes from the Na-alginate binder, while the Si, O and C come from the diatom frustules (anode AM) and CB. The presence of low amounts (below 1.3%) of fluorine and phosphorus in the sample could be attributed to potential contamination in the glovebox.

As seen in Fig. 4.26 on the first lithiation, the Si 2p signal is stable for the first three potentials upon lithiation. But from 0.2 V to 0.002 V the signal drastically drops. At the same potential, the C signal increases, at both 0 and 90 seconds of etching. This could indicate that the SEI is forming, in the way that electrolyte is being reduced onto the anode. During the delithiation, the Si 2p signal increases slightly. At the second lithiation stage, there is another decrease in the Si 2p signal and at 0.002 V the signal is almost gone at 0 and 90 seconds etching.

There is a clear difference in the C atomic percentage between the two etching times upon the first lithiation and delithiation. The atomic proportion of C in the non-etched specimen is roughly double the proportion detected in the 90 seconds etched sample. During the first 3 lithiation potentials, the C atomic percentage increases a $\sim$ 5% (Etch 0), but between 0.2 V and 0.002 V, it increases $\sim$ 5% (Etch 0). At delithiation, the C signal decreases by $\sim$ 6% between 0.002 V and 0.2 V, for both the sample with 0 and 90 seconds of etching. However, the signal then increases a little during delithiation. At the second lithiation, the C percentage decreases slightly at 0 and 90 seconds of etching.

The O signal is higher after etching than without, but the atomic percentage is not significantly different. During the course of lithiation, the signal decreases slightly, but it has a significant drop between 0.2 V and 0.002 V. Between the lithiation and delithiation at 0.2 V the O amount increases by $\sim$ 5% (Etch 0) and $\sim$ 8% (Etch 90). And then during the following delithiation potentials, it decreases by $\sim$ 2% (Etch 0) and $\sim$ 3% (Etch 90).

The Li percentage is similar during the first two potentials during lithiation at 90 seconds of etching. But at 0 seconds of etching the lithium content decreases between 1.1 V and 0.5 V. There is a higher increase in lithium atomic% for the data collected at 90 seconds of etching than for the data from the surface of the sample. But for both etching times there is a huge increase in lithium content from 0.2 V to 0.002 V during lithiation, $\sim$ 9% (Etch 0) and $\sim$ 20% (Etch 90) increase. This makes sense since lithium is inserted into the anode during lithiation. During delithiation, the lithium amount decreases in the anode, by $\sim$ 6% (Etch 0) and $\sim$ 7% (Etch 90). At the second lithiation the lithium amount increases by $\sim$ 8% (Etch 0) and $\sim$ 15% (Etch 90).

During the lithiation cycle, the F content of the anode increases greatly compared to its pristine state. The fluorine amount is highest during the first lithiation cycle, specifically at the 0.2 V stage the signal is highest. This indicates that the electrolyte is reacting with the anode material, forming LiF during lithiation. The signal increases during lithiation but decreases slightly between 0.2 V and 0.002 V. The F signal decreases a lot between the lithiation and the first delithiation potential. This could be due to the SEI being thicker. Then the F signal increases during delithiation, this could indicate SEI thinning. The F signal also decreases during the second lithiation.

Etch 0
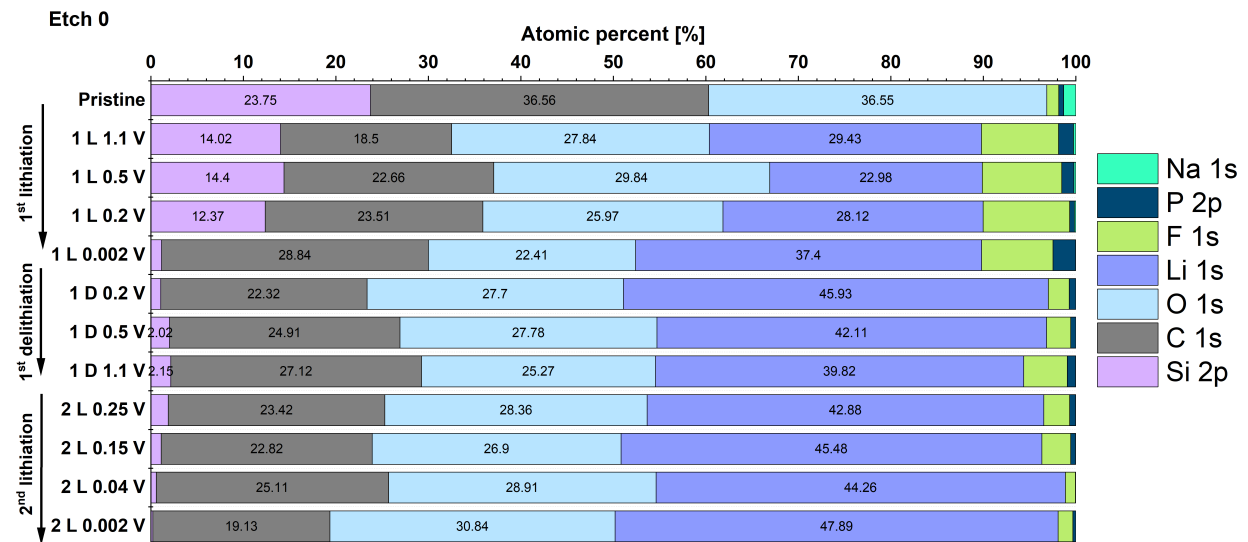
(a) Atomic composition from survey scan at 0 seconds etching.

Etch 90
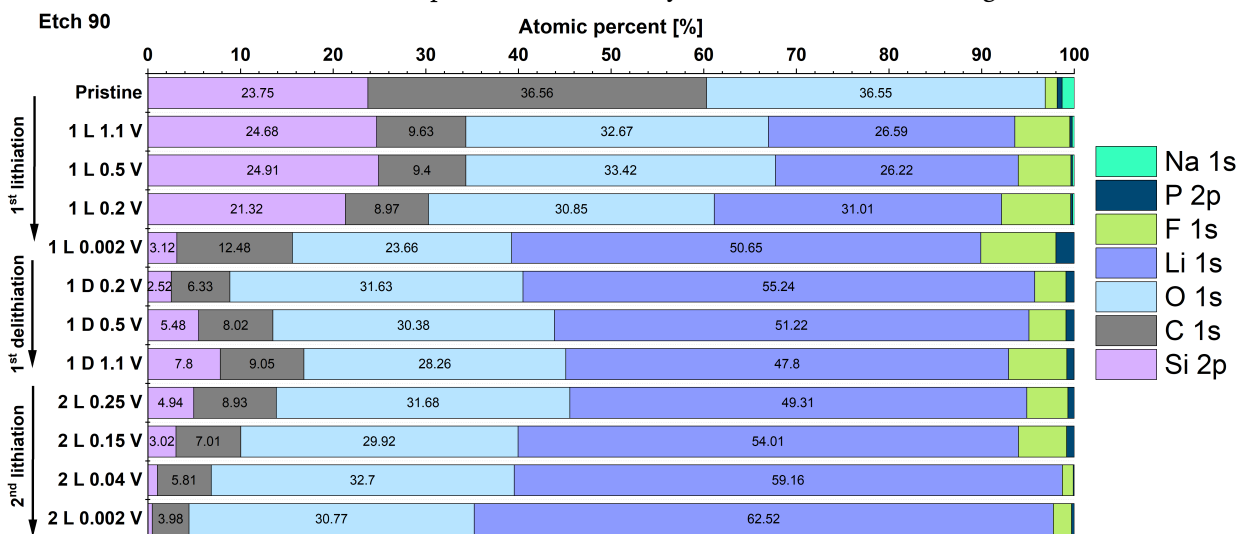
(b) Atomic composition from survey scan at 90 seconds etching.

Figure 4.25: Atomic composition of the electrode surface, determined by XPS survey scan at different potentials during lithiation and delithiation at a) 0 and b) 90 seconds etching.

(a) Etch 0 s.

(b) Etch 90 s.
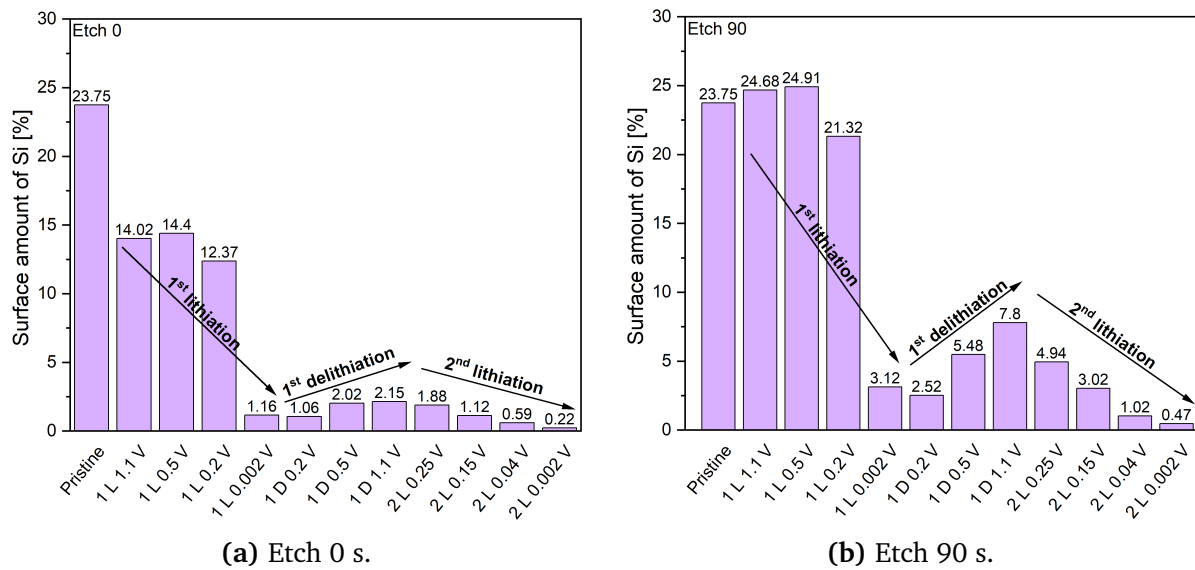
Figure 4.26: Evolution of Si content at the surface of the electrodes determined from XPS survey spectra upon the first lithiation/delithiation and second lithiation.

4.5 Morphological analysis

4.5.1 FIB/SEM of electrodes

The cross-section of the pristine electrode is shown in Fig. 4.27. The cut reveals a highly porous electrode and SiO$_2$ particles are clearly visible. At the electrode/Cu interphase, there is a noticeable void, revealing that the contact between the electrode and the current collector is uneven. This can lead to a higher current on the material that is in contact with it. Cross-sections of the cycled electrodes are shown in 4.28. Here, the electrode stopped at 0.002 V during the first lithiation is shown in Fig.4.28a and the electrode stopped during the first delithiation at 1.1 V is shown in Fig. 4.28b.

After the first lithiation, the electrode morphology looks less porous compared to the pristine electrode. This suggests electrolyte reaction products have deposited at the surface of the active material. This is consistent with the XPS results. Also, the active material particles might have undergone expansion upon lithiation, which also contributes to the porosity loss of the electrode.

The SEM image also shows some larger grey spots. This could be some large agglomerates, or some shadowing due to the instrument. In the third picture to the left, the large grey spots seem to have some small particles inside of it, corresponding to an agglomerate. The surface

of the cross-section has unevenly sized particles, and it seems like the electrode is denser higher up in the electrode and more porous deeper in the electrode.

When looking at the SEM picture of the delithiated electrode stopped at 1.1 V, the electrode exhibits visible cracks at the surface and throughout the whole electrode. On the right side of the main crack, the electrode is quite dense. While on the left side of the crack, the electrode is more porous. The porosity is very varied in the electrode samples which can lead to variations in the XPS signal. The delithiated particles seem larger than the particles in the pristine electrode, which could be due to the buffering components that have been formed upon lithiation.
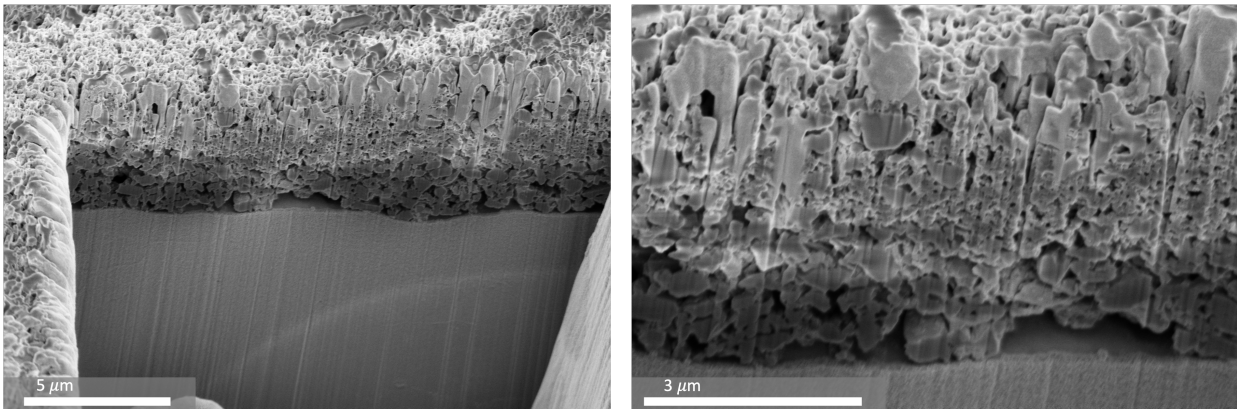
Figure 4.27: Cross-section of the pristine electrode.
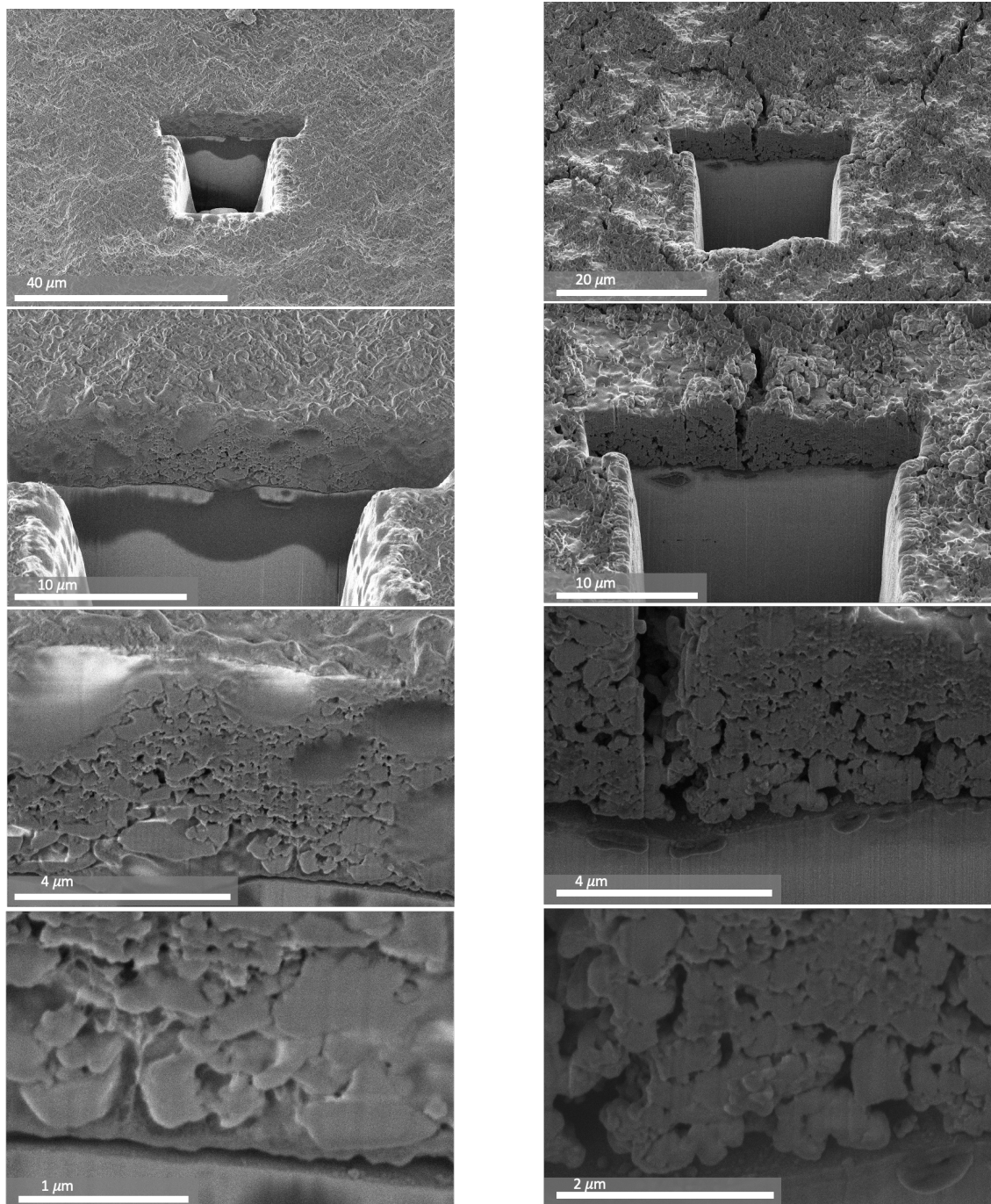
(a) First lithiation at 0.002 V.

(b) First delithiation at 1.1 V.

Figure 4.28: Cross-section of electrodes stopped at first lithiation and delithiation.

Chapter 5

Discussion

5.1 Electrochemical characterisation

5.1.1 Cycling stability

The evolution of the specific discharge capacity of SiO_2 anodes upon cycling, which is displayed in Table 4.1, show a gradual increase from 828 $mAhg^{-1}$ to 1172 $mAhg^{-1}$ during the first 4 activation cycles. The increase in capacity during the already described sequence of constant current and constant voltage step (activation procedure), is accompanied by a marked change in the voltage profile plots, which is in agreement with the conversion of SiO_2 to Si, resulting in a higher degree of Si utilisation in the Li−Si electrochemical alloying process [82]. After 4 activation cycles, the specific capacity reached a stable value, which can indicate that the material had reached a practical limit for lithiation. At this stage, the lithiation and delithiation reactions show a higher degree of reversibility, with CE above 94%. Additionally, the table shows how the specific capacity is relatively stable between 10 to 200 cycles. The relatively good cycling stability of the first 200 cycles, could be attributed to the buffering of the volume expansion of silicon by the products Li_2O, Li_4SiO_4 and $Li_2Si_2O_5$, which are formed during SiO_2 conversion to Si [37].

5.1.2 Differential capacity plot

The DC plot shown in Fig. 4.4 corresponds to the first four lithiation and delithiation cycles. During the first lithiation, there are three cathodic peaks at approximately 1.47 V, 0.83 V

and 0.042 V. During the second lithiation the cathodic peaks are positioned at 0.26 V, 0.17 V and 0.045 V. The peak at higher potentials is associated with irreversible conversion reactions between the electrolyte and the electrode [10]. In literature, it has been reported that Li$_{15}$Si$_4$ is formed at very low voltages ($\sim$ 0.05 V) [29] [84], therefore the peaks at first and second lithiation, 0.042 V and 0.045 V, respectively, could be resulting from this. During the second lithiation, the peak at 0.26 V could be attributed to Li$^+$ insertion into SiO$_2$, and the formation of Li$_2$Si$_2$O$_5$, Li$_4$SiO$_4$ and Si [29]. During the first delithiation, the anodic peaks are positioned at 0.029 V, 0.3 V and 0.45 V. The peaks at 0.3 V and 0.45 V could be attributed to the delithiation of the lithiated phase Li$_x$Si and the complete removal of lithium from the silicon [85]. While the peak at 0.029 V could be due to some artefact.

5.1.3   Cyclic voltammetry

The CV curves with a scanning rate of 0.1 mVs^{-1} and 0.05 mVs^{-1} are depicted in Fig. 4.5a and Fig. 4.6a, respectively. The reduction peaks at 1.45 V and 0.73 V are apparent during the first lithiation. These peaks have been previously reported and are associated with irreversible reactions and SEI formation [10]. The peak at 1.45 V is believed to be the result of the decomposition of the electrolyte additive FEC [48]. While the peak at 0.73 V could be the reduction of the solvent EC in the electrolyte [52], forming CH$_2$=CH$_2$ and Li$_2$CO$_3$ [50]. From another work, it has also been reported that at 0.72 V SiO$_2$ is converted to Li$_2$O and Si [30]. The cathodic peak at 1.16 V was only observed at the scan rate of 0.05 mVs^{-1} and could be attributed to the EC/DEC reduction, which has been reported to happen at 1.3 V [53]. These peaks are not clearly observed in the subsequent cycles, indicating the formation of SEI is mostly complete in the first cycle. The cathodic current increase appearing at voltages below 0.12 V could be assigned to the electrochemical reduction of SiO$_2$ to Si and the formation of Li$_2$O and Li$_4$SiO$_4$ [86]. In literature, it has been reported that Li$_2$Si$_2$O$_5$ and Li$_4$SiO$_4$ are formed at the potential 0.27 V and 0.24 V, respectively [29]. Although these voltages are above 0.1 V, it can be due to the difference in material and experimental procedure. Therefore, SiO$_2$ reactions could be assigned to the current increase at 0.1 V and 0.12 V.

During the first delithiation, two peaks at lower voltages are observed. One peak at 0.2 V and another at 0.5 V. It is difficult to say what these peaks are attributed to. From the literature, a peak at 0.25 V has been referred to as an oxidation peak of Si during Li$^+$ extraction from Li$_x$Si [9]. Another study reported the same reaction at an anodic peak at 0.33 V [87]. Other

reported reactions are the reversibility of $Li_2Si_2O_5$ to SiO_2, happening at 0.39 V [29]. The anodic peaks at 1.03 V and 1.38 V could be additional oxidation of silicates or some SEI dissociation.

5.2 Compositional analysis

5.2.1 Initial lithiation and delithiation

The investigation of SiO_2 anodes using XPS and argon etching revealed that the SiO_2 and SEI changes during early lithiation and delithiation cycles. In all selected potentials, the electrode surface is composed of electrolyte decomposition products, SiO_2 and Si-containing species. However, the specific chemical composition of the electrode varies depending on the state of charge (potential). The discussion will be about comparing the chemical composition during lithiation and delithiation at two different electrode depths, 0 and 90 seconds of etching, respectively. The peak analysis is based on CasaXPS software.

From the assumed reactions happening during the initial lithiation of SiO_2, the expected products are $Li_2Si_2O_5$, Li_4SiO_4, Li_2SiO_3, Li_2O and Si. Then Si is expected to further react to the lithiated form of Si, lithium silicide (Li_xSi). From the XPS spectra during the first and second lithiation, there are no peaks attributed to Li_xSi and almost no signal attributed to Si-Si. However, there are two peaks corresponding to SiO_2 and Li_xSiO_y.

In a publication by Philippe et al., SiO_2 and Li_xSiO_y signature in Si 2p was reported at 0.06 V and 0.01 V, and no Li_xSi peak was reported [63]. Notable the photon energy used for the XPS measurements was 230 eV, and Li_xSi signature appeared when the photon energy was increased to 1487 eV. Other similarities are the emergence of Li_xSiO_y below 0.5 V, at 0.1 V, which is in good agreement with the results presented in this work. The reason for not seeing the Si-Si and Li_xSiO_y signal emerging at the same time is not clear. It could be that the Si-Si signal is weakened because of the thickening of the SEI, and that the Li_xSiO_y are on top of the Si-Si, therefore only a Li_xSiO_y signal is seen. This is also the case in the same study, the Si-Si signature was reported until 0.1 V at lithiation, but this signal disappeared at 0.06 V [63]. During the first delithiation at 90 seconds of etching, the Li_xSiO_y peak displays a similar peak area. In literature one of the silicate components, $Li_2Si_2O_5$, is found to be reversible [29]. From the plots, it could be assumed that if this species is formed during the lithiation, the amount of it is minimal due to the stable peak area in the XPS spectra during

delithiation. Another reason could be that Li$_2$Si$_2$O$_5$ is not formed during lithiation, or that it is not a reversible component. When looking at the delithiation at 0 etching, the Li$_x$SiO$_y$ signal is increasing with delithiation, and the signal-to-noise ratio of the spectra is decreasing. This could be due to SEI dissolution, and that it is getting thinner, resulting in a better Si 2p signal [63]. From the second lithiation XPS Si 2p spectra the signal-to-noise ratio decreases during lithiation, presumably because the SEI is getting thicker. During the lithiation the silicate signal increases, indicating more SiO$_2$ is converted to Si.

Because of its specific O 1s signature with low binding energy compared to other oxygen species, it is very easy to detect Li$_2$O. It is first observed at the lowest voltage (0.002 V) as shown in Fig. 4.22. Most signal of this species is detected after 90 seconds of etching. Meaning that is probably located below the SEI. From a similar study, the Li$_2$O was observed at 0.06 V, and not at 0.1 V at a probing energy of 1487 eV [63]. This could mean that the emergence of Li$_2$O happens between 0.1 V and 0.002 V. However, at higher probing energy (2300 eV) the signature was observed at 0.1 V. When looking at the other oxygen-containing components during the first lithiation, the Li$_x$SiO$_y$ signature is most evident at 90 seconds of etching and at 0.002 V. This could indicate that Li$_2$O and Li$_x$SiO$_y$ are located at a similar depth, probably at the interphase between the SEI and the core silica/silicon/Li$_x$Si particle [63]. The signal from Li$_2$CO$_3$ in O 1s spectra is first visible with a low-intensity peak at 0.2 V, but when the potential is stopped at 0.002 V, the main signal comes from this species. This suggests that Li$_2$CO$_3$ is mostly formed at low voltages and is a part of the SEI since it has a higher signal than Li$_x$SiO$_y$ and Li$_2$O. During the delithiation the Li$_2$O component is not visible at 0 etching, but at 90 seconds of etching the component is visible, and has a relatively stable peak, indicating that the formation is not reversible. The reason that Li$_2$O is not visible at 0 etching is probably because the signal is too weak due to the SEI layer. At the second lithiation, the Li$_2$O component is also not visible before the etching of the electrode. In this case, the Li$_2$O peak increases in intensity during lithiation, and simultaneously the SiO$_2$ signal decreases. This could be due to the SiO$_2$ reaction to Li$_2$O, during lithiation. However, this could also be because the SEI gets thicker and decreases the signal from SiO$_2$, which can be observed by the survey scans.

The C 1s spectra evolve during lithiation and delithiation. During the first lithiation, there is a clear trend that the CB peak decreases compared to the C-C peak. One study done by Bryngelsson et al. suggested that this is related to the SEI getting thicker [88]. There is a weak signature of Li$_2$CO$_3$ at 1.1 V, which increases during lithiation, and at 0.002 V the peak

has the second highest intensity of the components in the C 1s spectra (Etch 90 s). The increase of the Li_2CO_3 signature is in good agreement with previous research [63]. All the C 1s spectra without etching have a higher signal of O—C=O and C—O than $LiCO_3$. This could indicate that the $LiCO_3$ lays below these components. During delithiation, the Li_2CO_3 signature decreases simultaneously as the CB signal increases. In literature, Li_2CO_3 component is found to be stable with the FEC additive [89]. Making the decrease in signal a question that needs to be further investigated. During the second lithiation at 90 seconds of etching the CB signal decreases, while the Li_2CO_3 peak is relatively stable. Further indicating that the SEI is getting thicker and that Li_2CO_3 is a big part of the SEI.

5.2.2   4 activation cycles XPS and HAXPES

When comparing the Si 2p spectra of the first delithiation (Fig. 4.15c) and the fourth delithiation (Fig. 4.20), there is a big difference. During the first delithiation at 1.1 V, the main peak corresponds to SiO_2, with a shoulder attributed to Li_xSiO_y. While after 4 cycles, the main signal in the electrode is attributed to Li_xSiO_y and Si-Si, and the SiO_2 peak is likely from noise. This is a major change in the chemical components of the electrode, showing that it takes at most 4 cycles to fully convert the SiO_2 to Li_xSiO_y and Si-Si. Although it could be claimed that this change could have taken place after 3 activation cycles, the electrochemical cycling data shows that a stable specific capacity is reached after 4 cycles. This can be interpreted as a full reaction of SiO_2 particles to form electroactive species that would then cycle reversibly. Importantly, a non-destructive depth profile analysis of delithiated SiO_2 anode subjected to 4 activation cycles was performed by HAXPES (with X-ray photon energies of 7 keV and 12 keV). This complementary analysis, Fig. 4.21, allowed the identification of Si as the main species of the Si 1s spectra and further supports the hypothesis that conversion of SiO_2 is almost complete after 4 activation cycles.

From the XPS technique, it was difficult to distinguish which specific silicates are formed, and in what amount the different silicates were. However, relevant information can be extracted from the Si 2p XPS spectra of the fully activated sample. The relative percentage of Si and Li_xSiO_y species (both SiO_2 reaction products) on the non-etched sample was calculated to be 43.1% and 51.4%, respectively. If we consider the Li_xSiO_y as non-electrochemically active species, then it is possible to conclude that after 4 activation cycles, the electrode is composed of 43.1% of Si electroactive domains and 51.4% of inactive species that would serve to ac-

commodate Si volume variations, therefore providing high stability to the electrode. This can be corroborated by the stable specific capacity that the electrode displays after 200 cycles.

Furthermore, it is also true that the combination of active and inactive species might be the key to providing higher stability to Si anodes. Therefore, gaining a fundamental understanding of SiO$_2$ reaction products and their role in electrode stability is crucial for the development of improved electrodes for next-generation LIB. A promising approach is the synthesis of SiO$_x$ compounds with tailored oxygen content, in which the Si/SiO$_2$ ratio can be tuned to optimise the ratio between electroactive Si domains, which will contribute to a high reversible capacity of the electrode, and inactive buffer species, which will provide higher stability to the anode. In this regard, our approach of quantifying the silicon-to-silicates ratio on fully reacted electrodes can be used as a baseline for studies on SiO$_x$ anodes. Also, it has been suggested that a fruitful approach for SiO$_2$ and SiO$_x$-based anodes, is to investigate whether it is possible to carefully control the electrode composition via some innovative pre-lithiation procedure or another pretreatment that maximise the amount of active components (e.g., Li$_x$Si) while simultaneously minimises the amount of inactive components (e.g., Li$_2$O, Li$_4$SiO$_4$) [82]. This approach with XPS on SiO$_2$ anodes could therefore give a fundamental understanding of the ratio of silicon and silicates needed.

5.2.3 Analysis of high-resolution spectra at different potentials

When investigating the SiO$_2$ reaction, the main emphasis is on studying the Si 2p and O 1s spectra. Looking at the Si 2p spectra during first lithiation and delithiation and second lithiation as seen in Fig. 4.22, Fig. 4.23 and Fig. 4.24, all these contain a main peak of SiO$_2$. During the first lithiation, there is an evolution of Li$_x$SiO$_y$ at lower potentials, specifically in the sample stopped at 0.002 V. At the same potential a low-intensity peak of Si-Si is present. This indicates that most of the SiO$_2$ reaction is happening at very low potentials, specifically below 0.2 V. This could correspond to the 0.042 V peak shown in the DC plot during the first lithiation. Additionally, in the sample at 0.002 V the O 1s spectra show a peak corresponding to Li$_2$O, which is one of the products of SiO$_2$ conversion to Si. However, previous studies have indicated that the etching process can induce the formation of Li$_2$O via the decomposition of SEI compounds like Li$_2$CO$_3$ [60]. But due to the Li$_2$O signal being present without etching, it could possibly be due to the SiO$_2$ reaction to Si (eq. 2.3.7). Li$_x$SiO$_y$ signature is also present in the O 1s spectra and increases during lithiation, supporting what is seen in the Si 2p spectra.

The formation of Li_2O and Li_xSiO_y has also been observed by a previous depth profiling XPS study on nano-silicon anodes [63]. During the second lithiation, the silicate peak in the Si 2p spectra (Etch 90) looks stable, being an indicator that the observed lithium silicates are irreversibly formed.

The onset of LiF is observed at 1.1 V, during the first lithiation. This is expected from the predicted reduction potential of FEC at around 1.47 V vs Li^+/Li [48]. In all the lithiation and delithiation spectra both the LiF and $LiPF_6$ component is present. The $LiPF_6$ peak could indicate incomplete removal of the electrolyte when washed with DMC.

5.2.4   Survey scans - information about the SEI

The surface chemical composition of the anode at selected potentials during lithiation and delithiation was determined by XPS survey scans. The evolution of the total amount of silicon is shown in Fig. 4.26, while a complete quantification of the different scanned elements is presented in Fig. 4.25, indicating the presence of Si, C, O, F, Li, F, P and Na. The data was selected for 0 and 90 seconds etching, to look at differences between the surface composition and the bulk composition of the electrode.

As shown in Fig. 4.26, the Si atomic% change upon lithiation and delithiation. The Si amount is higher in the samples scanned at 90 seconds of etching than at the un-etched electrode, presumably due to scanning closer to the SiO_2 particle with etching. For a sample consisting of bulk material like SiO_2/Si covered by a layer of different components like the SEI, the variation of intensity is to a high extent the result of variation in attenuation. Therefore, the atomic% of Si is mainly a measure of the increase/decrease of the thickness of the SEI [63]. The Si 2p atomic% dramatically drops upon the first lithiation between 0.2 V and 0.002 V. And at 0.002 V the Si atomic percentage had dropped 95% of the initial atomic percentage value measured on the pristine electrode. Since the amount of Si atoms should not decrease during lithiation, this decrease must be due to a weakening of the Si 2p signal due to the formation of the SEI. Upon delithiation, the Si 2p signal increases slightly but has a distinctly lower value than the pristine anode. This shows that SEI formation is also irreversible, as suggested by other publications [88]. During the second lithiation, the Si 2p signal decreases again, corresponding to the further development of the SEI. From this, presume that the SEI layer is a dynamic layer that changes during lithiation and delithiation.

The C signal from the pristine electrode is higher than for the cycled electrodes. The C

signal from the pristine electrode comes from the conductive additive in the electrode, namely Carbon Black. As the SEI layer is formed during lithiation, the CB is more covered, and less signal could come from this. Notably, the C content for the un-etched electrodes is much higher than for the 90 seconds etched electrodes. For un-etched electrodes, the C-H bond has the strongest signal and is primarily due to contamination of the surface. Therefore when the electrode is etched, the C-H signal decreases and less C signal is detected. The C amount for both un-etched and etched electrodes gradually increases from 1.1 V to 0.2 V. However, between 0.2 V and 0.002 V, the amount of carbon detected increased significantly. Since the C content increases during lithiation, this is likely due to the reduction of electrolyte, but it is lower than the pristine content since the SEI also contains components without carbon, like LiF.

Looking at the F amount at 1.1 V it has increased a lot compared to the pristine electrode. The F amount is expected to increase during lithiation since the electrolyte is containing both FEC and LiPF$_6$ which is reduced to LiF at 1.45 V from theory. The F amount increases during lithiation, but has a weaker signal during delithiation. This could be due to that most LiF is associated with the inner SEI layer. Additionally from the electrochemical data, there was no reduction peak associated with the reduction of FEC at the second lithiation cycle. Therefore the decrease in the F signal makes sense, now the more carbon-rich components in the outer SEI are forming.

The Li amount increased during lithiation and did not decrease drastically during delithiation. This could be because the lithium during lithiation has formed irreversible components like Li$_4$SiO$_4$, Li$_2$SiO$_3$ and Li$_2$O. However, the Li amount increases again during the second lithiation, indicating that Li$^+$ is entering the electrode during lithiation. Another study done on Si nanoparticles by Desrues et al investigated the surface composition by XPS [90]. Here, the electrolyte was a solution of LiPF$_6$ at 1M in EC/DEC (vol. 1:1) containing 2 wt% VC and 10 wt% FEC. The study reported a similar trend in the atomic composition during lithiation and delithiation, although the selected potentials were different.

During the delithiation both the Si and F amount increases. There are no reported reactions with the fluorine taking place during oxidation. Therefore the increase in amount must be due to an increased signal. One explanation for this could be that the SEI is getting thinner during delithiation [88].

5.2.5 Potential holding time

In this thesis, the criteria for the potential holding time was that the current of the sample had to decrease to 10% of the initial current value. As seen in Fig. 4.7 the samples stopped at different potentials, needed a very different potential holding time to come below this criteria. For the electrodes stopped at 1.1 V, 0.5 V and 0.2 V the current during potential hold decreased rapidly compared to the electrode stopped at 0.002 V, which decreased slowly and used 48 hours to get a low and stable current. We decided to use the same potential holding time (48 h) for all the samples. In another study, they selected the same holding time for all samples but used a 2-hour holding time [13]. If this method is going to be used again, the holding time could be selected individually for each sample, in order to assure that the holding time corresponds to reached steady-state for the specific electrode.

5.2.6 Irreversible capacity loss

When comparing the first and the second lithiation at 0.002 V, looking at the potential profiles in Fig. 4.12b and Fig. 4.19b, respectively, the specific capacity reached after the second lithiation is lower than at the first lithiation. The initial specific capacity during the first lithiation was 158 mAhg^{-1}, which increased to 726 mAhg^{-1} after the potential holding step. And during the second lithiation, the initial capacity was measured to be 299 mAhg^{-1}, and after the potential holding step, it increased to 618 mAhg^{-1}. At these potentials, most of the specific capacity is a result of lithium loss to the silicates and lithium carbonate formation. The capacity increases the most during the first lithiation, which could indicate that most of the silicates are formed during the first cycle. However, there is a huge increase as well during the second lithiation. From these plots, we see the importance of having a voltage holding time to have time to get the volume buffering components. From the potential plots during delithiation, there is a slight increase in specific capacity during the potential holding time. This could be due to some un-reacted components, that react during the voltage hold.

5.2.7 Challanges using XPS to investigate SiO$_2$ reactions

Investigating the SiO$_2$ reactions by XPS is difficult since the Si 2p signal decreases significantly during cycling. This is probably due to the SEI film covering the SiO$_2$ particles. A low signal results in significant noise in the Si 2p spectra, making it challenging to analyse using

software like CasaXPS. Additionally, using argon-ions to etch the electrode surface, is known to modify the chemistry and makes it hard to make conclusions if the chemical component is due to electrochemical reactions during cycling or due to the etching. Hence, results should be carefully interpreted.

5.3   Morphological analysis

SEM images of electrode cross-sections shown in Fig. 4.27 and Fig.4.28 show the morphological changes undergone by the SiO$_2$ anode upon lithiation and delithiation. These results are in good agreement with previous works [32]. Upon lithiation, as shown in Fig. 4.28a, the reaction of SiO$_2$ with lithium results in a volume expansion of the particles. While upon delithiation, shown in Fig. 4.28b, the removal of this lithium leads to the formation of cracks in the electrode. This is clearly seen in the 10 μm image that the crack extends through the hole electrode from the surface to the copper foil. Additionally, the electrode is more porous compared to the fully lithiated state. From the SEM image at 1 μm stopped at 0.002 V during the first lithiation, there seem to be some areas with large particles that are dense, and some parts with smaller particles with a more porous area.

Chapter 6

Conclusion

SiO$_2$ electrodes were fabricated using ball-milled SiO$_2$ from diatomaceous earth as active material. The electrodes were electrochemically cycled under a specific protocol involving a sequence of constant current and constant voltage steps, which are named "activation cycles". A thorough investigation of voltage-dependent chemical changes on the anodes upon electrochemical cycling was performed by cycling electrodes to selected potentials upon lithiation and delithiation. For each potential, depth profile analysis of chemical composition was performed by XPS coupled with argon ion sputtering.

One of the main conclusions of this work is the slow reaction between SiO$_2$ and lithium ions. During the first lithiation cycle, SEI is clearly formed. This can be inferred from the drastic drop in the Si species atomic percentage on lithiated electrodes, which was about 95% of the initial atomic percentage value measured on the pristine electrode. Interestingly, no major changes are observed on the SiO$_2$ matrix until the voltage reaches 0.002 V. At this potential, a significant amount of SiO$_2$ is converted to Li$_x$SiO$_y$ and Si, and the presence of such species is higher at deepest probing levels. Importantly, the increase of Li$_x$SiO$_y$ and Si species on the Si 2p spectrum shows a good correlation with the increase of Li$_2$O species on the O 1s spectrum, therefore suggesting that SiO$_2$ would be reacting with lithium ions via more than one route. The same trend is observed for the second lithiation cycle.

The second conclusion of this work is the importance of the electrochemical activation protocol to ensure full reaction of SiO$_2$ particles. XPS depth profiling results showed that after 4 activation cycles, most of the probed SiO$_2$ matrix has been fully converted to Li$_x$SiO$_y$ and electroactive Si. These results were also confirmed by HAXPES measurements, which allowed to probe a higher volume of the electrode in a non-destructive way, and by electrochemical

cycling results, which showed that after 4 activation cycles, the electrode reached a maximum reversible capacity of 1172 mAhg^{-1}. Importantly, this capacity remains stable after 200 cycles.

The third conclusion of this work is that, for the first time, the ratio between electroactive Si domains and presumably inactive Li$_x$SiO$_y$ species on fully reacted SiO$_2$ electrodes was established. According to the experimental results presented in this work, 43.1% of the original SiO$_2$ would convert to Si and 51.4% would have reacted with lithium ions to form Li$_x$SiO$_y$. In view of the potential contribution of Si to the total specific capacity of the electrodes and the contribution of Li$_x$SiO$_y$ species to the cycling stability of the anodes, it is expected that by modifying the Si/SiO$_2$ ratio on initial electrodes (e.g., by synthesising SiO$_x$ compounds of controlled stoichiometry) the reversible capacity and stability of the anodes can be optimised.

Morphological analysis of electrode cross-sections performed by FIB/SEM provided insights on microstructural changes occurring at the electrode level upon lithiation and delithiation. Results suggested that upon lithiation the volume of the active material particles expands, and electrode porosity is reduced, while during delithiation the electrode cracks.

Hence, SiO$_2$ from diatomaceous earth is a promising material to fabricate sustainably sourced anodes for next-generation Li-ion batteries. However, drawbacks such as high irreversible capacity loss and slow reaction of the material towards lithium ions are challenges that must be addressed in order to successfully integrate this material into battery technology. Gaining control of the Si/SiO$_2$ ratio on the active material as well as the exploration of different pre-lithiation protocols could pave the way for improving the performance of the presented anodes. In this regard, XPS depth profiling and HAXPES have shown to be adequate techniques to gain insights into the lithiation process of amorphous SiO$_2$ anodes.

Chapter 7

Further work

To further investigate the chemical changes of SiO_2 anodes upon initial cycling, the analysis should be complemented with non-destructive depth-resolved HAXPES investigations, providing a full assessment of SiO_2 lithiation and delithiation products deeper in the electrode.

In addition, the voltage-dependent XPS characterisation of chemical species of SiO_2 anodes for different lithiation/delithiation cycles could be complemented with high-resolution transmission electron microscopy (HR-TEM) and atom probe tomography (APT) analysis in order to identify the individual lithium silicates that are produced upon silica lithiation and to reveal their spatial distribution with respect to electroactive Si domains.

Bibliography

[1]   K. Hjelseng, 'Improving the performance algae-derived SiO2 anodes by optimizing electrode/electrolyte interphase,' Dept. of Mater. Sci, NTNU (2022).

[2]   J. Scheffran, M. Felkers and R. Froese, 'Economic Growth and the Global Energy Demand,' in *Green Energy to Sustainability*, John Wiley & Sons, Ltd, 2020, pp. 1–44. DOI: `10.1002/9781119152057.ch1`.

[3]   A. Midilli, I. Dincer and M. Ay, 'Green energy strategies for sustainable development,' *Energy Policy*, vol. 34, no. 18, pp. 3623–3633, 2006. DOI: `10.1016/j.enpol.2005.08.003`.

[4]   Artelys, D.-G. for Energy (European Commission), Enerdata, Trinomics, C. Andrey, P. Barberi, L. v. Nuffel, F. Gérard, J. Gorenstein Dedecca, K. Rademaekers, Y. El Idrissi, M. Crenes and L. Lacombe, *Study on energy storage: contribution to the security of the electricity supply in Europe*. LU: Publications Office of the European Union, 2020.

[5]   W. van Schalkwijk and B. Scrosati, in *Advances in Lithium-Ion Batteries*, W. A. van Schalkwijk and B. Scrosati, Eds., Springer US, 2002, pp. 1–5. DOI: `10.1007/0-306-47508-1_1`.

[6]   A. Manthiram, 'An Outlook on Lithium Ion Battery Technology,' *ACS Central Science*, vol. 3, no. 10, pp. 1063–1069, 2017, Publisher: American Chemical Society. DOI: `10.1021/acscentsci.7b00288`.

[7]   P. Dolega, M. Buchert and J. Betz, 'Environmental and socio-economic challenges in battery supply chains: Graphite and lithium,' Tech. Rep., 2020.

[8]   M. Ashuri, Q. He and L. L. Shaw, 'Silicon as a potential anode material for Li-ion batteries: Where size, geometry and structure matter,' *Nanoscale*, vol. 8, no. 1, pp. 74–103, 2016, Publisher: Royal Society of Chemistry. DOI: `10.1039/C5NR05116A`.

[9]   Z. Favors, W. Wang, H. H. Bay, A. George, M. Ozkan and C. S. Ozkan, 'Stable Cycling of SiO2 Nanotubes as High-Performance Anodes for Lithium-Ion Batteries,' *Scientific Reports*, vol. 4, no. 1, p. 4605, 2014, Number: 1 Publisher: Nature Publishing Group. DOI: 10.1038/srep04605.

[10]   G. Lener, M. Otero, D. E. Barraco and E. P. M. Leiva, 'Energetics of silica lithiation and its applications to lithium ion batteries,' *Electrochimica Acta*, vol. 259, pp. 1053–1058, 2018. DOI: 10.1016/j.electacta.2017.10.126.

[11]   A. M. Tripathi, W.-N. Su and B. J. Hwang, 'In situ analytical techniques for battery interface analysis,' *Chemical Society Reviews*, vol. 47, no. 3, pp. 736–851, 2018, Publisher: The Royal Society of Chemistry. DOI: 10.1039/C7CS00180K.

[12]   C. K. Chan, R. Ruffo, S. S. Hong and Y. Cui, 'Surface chemistry and morphology of the solid electrolyte interphase on silicon nanowire lithium-ion battery anodes,' *Journal of Power Sources*, vol. 189, no. 2, pp. 1132–1140, 2009. DOI: 10.1016/j.jpowsour.2009. 01.007.

[13]   C. Cao, I. I. Abate, E. Sivonxay, B. Shyam, C. Jia, B. Moritz, T. P. Devereaux, K. A. Persson, H.-G. Steinrück and M. F. Toney, 'Solid Electrolyte Interphase on Native Oxide-Terminated Silicon Anodes for Li-Ion Batteries,' *Joule*, vol. 3, no. 3, pp. 762–781, 2019.

[14]   R. Ruffo, S. S. Hong, C. K. Chan, R. A. Huggins and Y. Cui, 'Impedance Analysis of Silicon Nanowire Lithium Ion Battery Anodes,' *The Journal of Physical Chemistry C*, vol. 113, no. 26, pp. 11 390–11 398, 2009, Publisher: American Chemical Society. DOI: 10.1021/jp901594g.

[15]   C. Julien, A. Mauger, A. Vijh and K. Zaghib, *Lithium batteries : science and technology*. Cham: Springer, 2016.

[16]   J. B. Goodenough and K.-S. Park, 'The Li-Ion Rechargeable Battery: A Perspective,' *Journal of the American Chemical Society*, vol. 135, no. 4, pp. 1167–1176, 2013, Publisher: American Chemical Society. DOI: 10.1021/ja3091438.

[17]   H. Berg, *Batteries for electric vehicles : Materials and electrochemistry*, Cambridge, 2015.

[18]   M. Qadrdan, N. Jenkins and J. Wu, in *McEvoy's Handbook of Photovoltaics (Third Edition)*, S. A. Kalogirou, Ed., Academic Press, 2018, pp. 915–928. DOI: 10.1016/B978-0-12-809921-6.00025-2.

[19] Y. Lu, L. Yu and X. W. (Lou, 'Nanostructured Conversion-type Anode Materials for Advanced Lithium-Ion Batteries,' *Chem*, vol. 4, no. 5, 2018. DOI: `10.1016/j.chempr.2018.01.003`.

[20] K. Xu, 'Nonaqueous Liquid Electrolytes for Lithium-Based Rechargeable Batteries,' *Chemical Reviews*, vol. 104, no. 10, pp. 4303–4418, 2004, Publisher: American Chemical Society. DOI: `10.1021/cr030203g`.

[21] J. Lu, Z. Chen, F. Pan, Y. Cui and K. Amine, 'High-Performance Anode Materials for Rechargeable Lithium-Ion Batteries,' *Electrochemical Energy Reviews*, vol. 1, no. 1, pp. 35–53, 2018. DOI: `10.1007/s41918-018-0001-4`.

[22] C.-M. Park, J.-H. Kim, H. Kim and H.-J. Sohn, 'Li-alloy based anode materials for Li secondary batteries,' *Chemical Society Reviews*, vol. 39, no. 8, pp. 3115–3141, 2010, Publisher: The Royal Society of Chemistry. DOI: `10.1039/B919877F`.

[23] C. Zhang, F. Wang, J. Han, S. Bai, J. Tan, J. Liu and F. Li, 'Challenges and Recent Progress on Silicon-Based Anode Materials for Next-Generation Lithium-Ion Batteries,' *Small Structures*, vol. 2, no. 6, p. 2 100 009, 2021. DOI: `10.1002/sstr.202100009`.

[24] K. Ogata, E. Salager, C. J. Kerr, A. E. Fraser, C. Ducati, A. J. Morris, S. Hofmann and C. P. Grey, 'Revealing lithium–silicide phase transformations in nano-structured silicon-based lithium ion batteries via in situ NMR spectroscopy,' *Nature Communications*, vol. 5, no. 1, p. 3217, 2014, Number: 1 Publisher: Nature Publishing Group. DOI: `10.1038/ncomms4217`.

[25] M. Takla, N. E. Kamfjord, H. Tveit and S. Kjelstrup, 'Energy and exergy analysis of the silicon production process,' *Energy*, vol. 58, pp. 138–146, 2013. DOI: `10.1016/j.energy.2013.04.051`.

[26] B. Guo, J. Shu, Z. Wang, H. Yang, L. Shi, Y. Liu and L. Chen, 'Electrochemical reduction of nano-SiO2 in hard carbon as anode material for lithium ion batteries,' *Electrochemistry Communications*, vol. 10, no. 12, pp. 1876–1878, 2008. DOI: `10.1016/j.elecom.2008.09.032`.

[27] Q. Sun, B. Zhang and Z.-W. Fu, 'Lithium electrochemistry of SiO2 thin film electrode for lithium-ion batteries,' *Applied Surface Science*, vol. 254, no. 13, pp. 3774–3779, 2008. DOI: `10.1016/j.apsusc.2007.11.058`.

[28] M. N. Obrovac and V. L. Chevrier, 'Alloy Negative Electrodes for Li-Ion Batteries,' *Chemical Reviews*, vol. 114, no. 23, pp. 11 444–11 502, 2014, Publisher: American Chemical Society. DOI: `10.1021/cr500207g`.

[29] W.-S. Chang, C.-M. Park, J.-H. Kim, Y.-U. Kim, G. Jeong and H.-J. Sohn, 'Quartz (SiO2): A new energy storage anode material for Li-ion batteries,' *Energy & Environmental Science*, vol. 5, no. 5, pp. 6895–6899, 2012, Publisher: The Royal Society of Chemistry. DOI: `10.1039/C2EE00003B`.

[30] J. Tu, Y. Yuan, P. Zhan, H. Jiao, X. Wang, H. Zhu and S. Jiao, 'Straightforward Approach toward SiO2 Nanospheres and Their Superior Lithium Storage Performance,' *The Journal of Physical Chemistry C*, vol. 118, no. 14, pp. 7357–7362, 2014, Publisher: American Chemical Society. DOI: `10.1021/jp5011023`.

[31] N. Nitta, F. Wu, J. T. Lee and G. Yushin, 'Li-ion battery materials: Present and future,' *Materials Today*, vol. 18, no. 5, pp. 252–264, 2015. DOI: `10.1016/j.mattod.2014.10.040`.

[32] M. S. Al Ja'farawy, D. N. Hikmah, U. Riyadi, A. Purwanto and H. Widiyandari, 'A Review: The Development of SiO2/C Anode Materials for Lithium-Ion Batteries,' *Journal of Electronic Materials*, vol. 50, no. 12, pp. 6667–6687, 2021. DOI: `10.1007/s11664-021-09187-x`.

[33] C. Tang, Y. Liu, C. Xu, J. Zhu, X. Wei, L. Zhou, L. He, W. Yang and L. Mai, 'Ultrafine Nickel-Nanoparticle-Enabled SiO2 Hierarchical Hollow Spheres for High-Performance Lithium Storage,' *Advanced Functional Materials*, vol. 28, no. 3, p. 1 704 561, 2018. DOI: `10.1002/adfm.201704561`.

[34] M. V. Blanco, V. Renman, F. Vullum-Bruer and A. M. Svensson, 'Nanostructured diatom earth SiO2 negative electrodes with superior electrochemical performance for lithium ion batteries,' *RSC Advances*, vol. 10, no. 55, pp. 33 490–33 498, 2020, Publisher: The Royal Society of Chemistry. DOI: `10.1039/D0RA05749E`.

[35] J. W. G. Lund, 'The biology of diatoms.,' *Limnology and Oceanography*, vol. 24, no. 1, pp. 200–200, 1979. DOI: `10.4319/lo.1979.24.1.0200`.

[36] P. Aggrey, M. Nartey, Y. Kan, J. Cvjetinovic, A. Andrews, A. I. Salimon, K. I. Dragnevski and A. M. Korsunsky, 'On the diatomite-based nanostructure-preserving material syn-

thesis for energy applications,' *RSC Advances*, vol. 11, no. 51, pp. 31 884–31 922, 2021, Publisher: The Royal Society of Chemistry. DOI: `10.1039/D1RA05810J`.

[37] N. Yan, F. Wang, H. Zhong, Y. Li, Y. Wang, L. Hu and Q. Chen, 'Hollow Porous SiO2 Nanocubes Towards High-performance Anodes for Lithium-ion Batteries,' *Scientific Reports*, vol. 3, no. 1, p. 1568, 2013, Number: 1 Publisher: Nature Publishing Group. DOI: `10.1038/srep01568`.

[38] M. Khan, X. Ding, H. Zhao, Y. Wang, N. Zhang, X. Chen and J. Xu, 'SiO2-Based Lithium-Ion Battery Anode Materials: A Brief Review,' *Journal of Electronic Materials*, vol. 51, no. 7, pp. 3379–3390, 2022. DOI: `10.1007/s11664-022-09628-1`.

[39] J. B. Goodenough and Y. Kim, 'Challenges for Rechargeable Li Batteries,' *Chemistry of Materials*, vol. 22, no. 3, pp. 587–603, 2010, Publisher: American Chemical Society. DOI: `10.1021/cm901452z`.

[40] M. Hu, X. Pang and Z. Zhou, 'Recent progress in high-voltage lithium ion batteries,' *Journal of Power Sources*, vol. 237, pp. 229–242, 2013. DOI: `10.1016/j.jpowsour.2013.03.024`.

[41] S. Han, 'Structure and dynamics in the lithium solvation shell of nonaqueous electrolytes,' *Scientific Reports*, vol. 9, p. 5555, 2019. DOI: `10.1038/s41598-019-42050-y`.

[42] K. Xu, 'Electrolytes: Overview,' *Encyclopedia of Electrochemical Power Sources*, vol. 5, pp. 51–70, 2009.

[43] L. Lv, Y. Wang, W. Huang, Y. Wang, G. Zhu and H. Zheng, 'Effect of lithium salt type on silicon anode for lithium-ion batteries,' *Electrochimica Acta*, vol. 413, p. 140 159, 2022. DOI: `10.1016/j.electacta.2022.140159`.

[44] S. E. Trask, K. Z. Pupek, J. A. Gilbert, M. Klett, B. J. Polzin, A. N. Jansen and D. P. Abraham, 'Performance of Full Cells Containing Carbonate-Based LiFSI Electrolytes and Silicon-Graphite Negative Electrodes,' *Journal of The Electrochemical Society*, vol. 163, no. 3, A345, 2015, Publisher: IOP Publishing. DOI: `10.1149/2.0981602jes`.

[45] H.-B. Han, S.-S. Zhou, D.-J. Zhang, S.-W. Feng, L.-F. Li, K. Liu, W.-F. Feng, J. Nie, H. Li, X.-J. Huang, M. Armand and Z.-B. Zhou, 'Lithium bis(fluorosulfonyl)imide (LiFSI) as conducting salt for nonaqueous liquid electrolytes for lithium-ion batteries: Physicochemical and electrochemical properties,' en, *Journal of Power Sources*, vol. 196, no. 7, 2011. DOI: `10.1016/j.jpowsour.2010.12.040`.

[46]   M. Gauthier, D. Mazouzi, D. Reyter, B. Lestriez, P. Moreau, D. Guyomard and L. Roué, 'A
       low-cost and high performance ball-milled Si-based negative electrode for high-energy
       Li-ion batteries,' *Energy & Environmental Science*, vol. 6, no. 7, pp. 2145–2155, 2013,
       Publisher: The Royal Society of Chemistry. DOI: `10.1039/C3EE41318G`.

[47]   Y.-M. Lin, K. C. Klavetter, P. R. Abel, N. C. Davy, J. L. Snider, A. Heller and C. B. Mullins,
       'High performance silicon nanoparticle anode in fluoroethylene carbonate-based elec-
       trolyte for Li-ion batteries,' *Chemical Communications*, vol. 48, no. 58, pp. 7268–7270,
       2012, Publisher: The Royal Society of Chemistry. DOI: `10.1039/C2CC31712E`.

[48]   T. Jaumann, J. Balach, U. Langklotz, V. Sauchuk, M. Fritsch, A. Michaelis, V. Teltevskij,
       D. Mikhailova, S. Oswald, M. Klose, G. Stephani, R. Hauser, J. Eckert and L. Giebeler,
       'Lifetime vs. rate capability: Understanding the role of FEC and VC in high-energy Li-ion
       batteries with nano-silicon anodes,' *Energy Storage Materials*, vol. 6, pp. 26–35, 2017.
       DOI: `10.1016/j.ensm.2016.08.002`.

[49]   K. Xu, 'Electrolytes and Interphases in Li-Ion Batteries and Beyond,' *Chemical Reviews*,
       vol. 114, no. 23, pp. 11 503–11 618, 2014, Publisher: American Chemical Society. DOI:
       `10.1021/cr500003w`.

[50]   B. Philippe, 'Insights in li-ion battery interfaces through photoelectron spectroscopy
       depth profiling,' 2013.

[51]   A. L. Michan, B. S. Parimalam, M. Leskes, R. N. Kerber, T. Yoon, C. P. Grey and B. L. Lucht,
       'Fluoroethylene Carbonate and Vinylene Carbonate Reduction: Understanding Lithium-
       Ion Battery Electrolyte Additives and Solid Electrolyte Interphase Formation,' *Chemistry
       of Materials*, vol. 28, no. 22, pp. 8149–8159, 2016, Publisher: American Chemical So-
       ciety. DOI: `10.1021/acs.chemmater.6b02282`.

[52]   S. Yoon, H. Kim, J.-J. Cho, Y.-K. Han and H. Lee, 'Lactam derivatives as solid electrolyte
       interphase forming additives for a graphite anode of lithium-ion batteries,' *Journal of
       Power Sources*, vol. 244, pp. 711–715, 2013. DOI: `10.1016/j.jpowsour.2012.11.115`.

[53]   S. J. An, J. Li, C. Daniel, D. Mohanty, S. Nagpure and D. L. Wood, 'The state of un-
       derstanding of the lithium-ion-battery graphite solid electrolyte interphase (SEI) and
       its relationship to formation cycling,' en, *Carbon*, vol. 105, pp. 52–76, 2016. DOI: `10.
       1016/j.carbon.2016.04.008`.

[54] S. K. Heiskanen, J. Kim and B. L. Lucht, 'Generation and Evolution of the Solid Electrolyte Interphase of Lithium-Ion Batteries,' *Joule*, vol. 3, no. 10, pp. 2322–2333, 2019. DOI: 10.1016/j.joule.2019.08.018.

[55] E. Peled, 'The Electrochemical Behavior of Alkali and Alkaline Earth Metals in Nonaqueous Battery Systems—The Solid Electrolyte Interphase Model,' *Journal of The Electrochemical Society*, vol. 126, no. 12, p. 2047, 1979, Publisher: The Electrochemical Society, Inc. DOI: 10.1149/1.2128859.

[56] V. A. Agubra and J. W. Fergus, 'The formation and stability of the solid electrolyte interface on the graphite anode,' *Journal of Power Sources*, vol. 268, pp. 153–162, 2014. DOI: 10.1016/j.jpowsour.2014.06.024.

[57] A. Tokranov, R. Kumar, C. Li, S. Minne, X. Xiao and B. W. Sheldon, 'Control and Optimization of the Electrochemical and Mechanical Properties of the Solid Electrolyte Interphase on Silicon Electrodes in Lithium Ion Batteries,' *Advanced Energy Materials*, vol. 6, no. 8, p. 1 502 302, 2016. DOI: 10.1002/aenm.201502302.

[58] F. A. Stevie and C. L. Donley, 'Introduction to x-ray photoelectron spectroscopy,' *Journal of Vacuum Science & Technology A*, vol. 38, no. 6, p. 063 204, 2020, Publisher: American Vacuum Society. DOI: 10.1116/6.0000412.

[59] C. R. Brundle and B. V. Crist, 'X-ray photoelectron spectroscopy: A perspective on quantitation accuracy for composition analysis of homogeneous materials,' *Journal of Vacuum Science & Technology A*, vol. 38, no. 4, p. 041 001, 2020. DOI: 10.1116/1.5143897.

[60] T. Jaumann, J. Balach, M. Klose, S. Oswald, J. Eckert and L. Giebeler, 'Role of 1,3-Dioxolane and LiNO3 Addition on the Long Term Stability of Nanostructured Silicon/Carbon Anodes for Rechargeable Lithium Batteries,' *Journal of The Electrochemical Society*, vol. 163, no. 3, A557, 2016, Publisher: IOP Publishing. DOI: 10.1149/2.1011603jes.

[61] D. Briggs, 'Handbook of X-ray Photoelectron Spectroscopy C. D. Wanger, W. M. Riggs, L. E. Davis, J. F. Moulder and G. E.Muilenberg Perkin-Elmer Corp., Physical Electronics Division, Eden Prairie, Minnesota, USA, 1979. 190 pp. \$195,' *Surface and Interface Analysis*, vol. 3, no. 4, 1981. DOI: 10.1002/sia.740030412.

[62]   D. R. Baer, K. Artyushkova, H. Cohen, C. D. Easton, M. Engelhard, T. R. Gengenbach, G. Greczynski, P. Mack, D. J. Morgan and A. Roberts, 'XPS guide: Charge neutralization and binding energy referencing for insulating samples,' *Journal of Vacuum Science & Technology A*, vol. 38, no. 3, p. 031 204, 2020, Publisher: American Vacuum Society. DOI: `10.1116/6.0000057`.

[63]   B. Philippe, R. Dedryvère, J. Allouche, F. Lindgren, M. Gorgoi, H. Rensmo, D. Gonbeau and K. Edström, 'Nanosilicon Electrodes for Lithium-Ion Batteries: Interfacial Mechanisms Studied by Hard and Soft X-ray Photoelectron Spectroscopy,' *Chemistry of Materials*, vol. 24, no. 6, pp. 1107–1115, 2012, Publisher: American Chemical Society. DOI: `10.1021/cm2034195`.

[64]   *Carbon | XPS Periodic Table - NO*, en. [Online]. Available: `https://www.thermofisher.com/uk/en/home/materials-science/learning-center/periodic-table/non-metal/carbon.html` (visited on 15/11/2022).

[65]   *X-ray Photoelectron Spectroscopy (XPS) Reference Pages*. [Online]. Available: `http://www.xpsfitting.com/search/label/carbon` (visited on 26/05/2023).

[66]   *NIST XPS Database Detail Page*. [Online]. Available: `https://srdata.nist.gov/xps/XPSDetailPage.aspx?AllDataNo=21820` (visited on 14/05/2023).

[67]   *NIST XPS Database Detail Page*. [Online]. Available: `https://srdata.nist.gov/xps/XPSDetailPage.aspx?AllDataNo=21800` (visited on 26/05/2023).

[68]   *Oxygen | XPS Periodic Table - NO*. [Online]. Available: `https://www.thermofisher.com/uk/en/home/materials-science/learning-center/periodic-table/non-metal/oxygen.html` (visited on 16/11/2022).

[69]   *NIST XPS Database Detail Page*. [Online]. Available: `https://srdata.nist.gov/xps/XPSDetailPage.aspx?AllDataNo=21819` (visited on 14/05/2023).

[70]   *X-ray Photoelectron Spectroscopy (XPS) Reference Pages*. [Online]. Available: `http://www.xpsfitting.com/search/label/Fluorine` (visited on 14/05/2023).

[71]   *X-ray Photoelectron Spectroscopy (XPS) Reference Pages*. [Online]. Available: `http://www.xpsfitting.com/search/label/Silicon` (visited on 14/05/2023).

[72] B. Philippe, R. Dedryvère, M. Gorgoi, H. Rensmo, D. Gonbeau and K. Edström, 'Role of the LiPF6 Salt for the Long-Term Stability of Silicon Electrodes in Li-Ion Batteries – A Photoelectron Spectroscopy Study,' *Chemistry of Materials*, vol. 25, no. 3, pp. 394–404, 2013, Publisher: American Chemical Society. DOI: `10.1021/cm303399v`.

[73] *NIST XPS Database Detail Page*. [Online]. Available: `https://srdata.nist.gov/xps/XPSDetailPage.aspx?AllDataNo=43408` (visited on 26/05/2023).

[74] M. Sachs, M. Gellert, M. Chen, H.-J. Drescher, S. R. Kachel, H. Zhou, M. Zugermeier, M. Gorgoi, B. Roling and J. M. Gottfried, 'LiNi0.5Mn1.5O4 high-voltage cathode coated with Li4Ti5O12: A hard X-ray photoelectron spectroscopy (HAXPES) study,' *Physical Chemistry Chemical Physics*, vol. 17, no. 47, pp. 31 790–31 800, 2015, Publisher: The Royal Society of Chemistry. DOI: `10.1039/C5CP03837E`.

[75] W. Zhou, R. Apkarian, Z. L. Wang and D. Joy, 'Fundamentals of Scanning Electron Microscopy (SEM),' in *Scanning Microscopy for Nanotechnology: Techniques and Applications*, W. Zhou and Z. L. Wang, Eds., Springer, 2007, pp. 1–40. DOI: `10.1007/978-0-387-39620-0_1`.

[76] 'Scanning Electron Microscopy,' in *Microstructural Characterization of Materials*, John Wiley & Sons, Ltd, 2008. DOI: `10.1002/9780470727133.ch5`.

[77] *Focused Ion Beam Systems: Basics and Applications*. Cambridge University Press, 2007. DOI: `10.1017/CBO9780511600302`.

[78] F. B. Frackowiak Elzbieta, Ed., *Carbons for Electrochemical Energy Storage and Conversion Systems*. CRC Press, 2009. DOI: `10.1201/9781420055405`.

[79] *Investigating battery aging using Differential Capacity Analysis (DCA)*. [Online]. Available: `https://www.biologic.net/topics/investigating-battery-ageing-using-differential-capacity-analysis-dca/` (visited on 05/12/2022).

[80] N. Elgrishi, K. J. Rountree, B. D. McCarthy, E. S. Rountree, T. T. Eisenhart and J. L. Dempsey, 'A Practical Beginner's Guide to Cyclic Voltammetry,' *Journal of Chemical Education*, vol. 95, no. 2, pp. 197–206, 2018, Publisher: American Chemical Society. DOI: `10.1021/acs.jchemed.7b00361`.

[81] W. Hou, H. Li, M. Li and B. Cheng, 'Effects and optimization of ratio of particle size grading on compaction density of calcined coke particles,' *Materials Research Express*, vol. 7, no. 8, p. 085 605, 2020, Publisher: IOP Publishing. DOI: 10.1088/2053-1591/abafcc.

[82] V. Renman, M. V. Blanco, A. N. Norberg, F. Vullum-Bruer and A. M. Svensson, 'Electrochemical activation of a diatom-derived SiO2/C composite anode and its implementation in a lithium ion battery,' *Solid State Ionics*, vol. 371, p. 115 766, 2021. DOI: 10.1016/j.ssi.2021.115766.

[83] D. A. Agyeman, K. Song, G.-H. Lee, M. Park and Y.-M. Kang, 'Carbon-Coated Si Nanoparticles Anchored between Reduced Graphene Oxides as an Extremely Reversible Anode Material for High Energy-Density Li-Ion Battery,' *Advanced Energy Materials*, vol. 6, no. 20, p. 1 600 904, 2016. DOI: 10.1002/aenm.201600904.

[84] C. Gan, X. Ye, S. Zhang, J. Chen, W. Wen, Y. Liu, D.-L. Peng, L. Tang and X. Luo, 'Current density induced growth of Li15Si4 alloy in silicon-carbon anodes during first lithiation process,' *Journal of Energy Storage*, vol. 41, p. 102 930, 2021. DOI: 10.1016/j.est.2021.102930.

[85] B. Jerliu, E. Hüger, L. Dörrer, B. K. Seidlhofer, R. Steitz, M. Horisberger and H. Schmidt, 'Lithium insertion into silicon electrodes studied by cyclic voltammetry and operando neutron reflectometry,' *Physical Chemistry Chemical Physics*, vol. 20, no. 36, pp. 23 480–23 491, 2018, Publisher: Royal Society of Chemistry. DOI: 10.1039/C8CP03540G.

[86] X. Cao, X. Chuan, S. Li, D. Huang and G. Cao, 'Hollow Silica Spheres Embedded in a Porous Carbon Matrix and Its Superior Performance as the Anode for Lithium-Ion Batteries,' *Particle & Particle Systems Characterization*, vol. 33, no. 2, pp. 110–117, 2016. DOI: 10.1002/ppsc.201500218.

[87] W. Wang, Z. Favors, R. Ionescu, R. Ye, H. H. Bay, M. Ozkan and C. S. Ozkan, 'Monodisperse Porous Silicon Spheres as Anode Materials for Lithium Ion Batteries,' *Scientific Reports*, vol. 5, no. 1, p. 8781, 2015, Number: 1 Publisher: Nature Publishing Group. DOI: 10.1038/srep08781.

[88] H. Bryngelsson, M. Stjerndahl, T. Gustafsson and K. Edström, 'How dynamic is the SEI?' *Journal of Power Sources*, vol. 174, no. 2, pp. 970–975, 2007. DOI: 10.1016/j.jpowsour.2007.06.050.

[89] J. Kim, O. B. Chae and B. L. Lucht, 'Perspective—Structure and Stability of the Solid Electrolyte Interphase on Silicon Anodes of Lithium-ion Batteries,' *Journal of The Electrochemical Society*, vol. 168, no. 3, p. 030 521, 2021, Publisher: IOP Publishing. DOI: `10.1149/1945-7111/abe984`.

[90] A. Desrues, E. De Vito, F. Boismain, J. P. Alper, C. Haon, N. Herlin-Boime and S. Franger, 'Electrochemical and X-ray Photoelectron Spectroscopic Study of Early SEI Formation and Evolution on Si and Si@C Nanoparticle-Based Electrodes,' *Materials*, vol. 15, no. 22, p. 7990, 2022, Number: 22 Publisher: Multidisciplinary Digital Publishing Institute. DOI: `10.3390/ma15227990`.

Appendix A

Appendix

A.1 Supplementary notes on experimental work

A.1.1 Actual alginate binder composition

The actual composition of the alginate binder used in the slurry to make electrodes is shown in Table A.1.

Table A.1: Actual composition used in the alginate binder.

Batch date	Sodium Alginate [g]	DI water [g]
27.01.23	0.50200	29.5106

A.1.2 Actual slurry composition

The actual composition of the slurry for casting is found in Table A.2. The Alginate binder used corresponds to the one in Table A.1.

Table A.2: Actual composition of SiO_2 cast.

| Cast date	Active material [g]	Carbon black [g]	Alginate binder [g]
31.01.23	0.2008	0.0402	1.6034

A.1.3   Cells cycled

Table A.3: Overview of cycled cells with active material loading. L and D denote lithiation and delithiation, respectively.
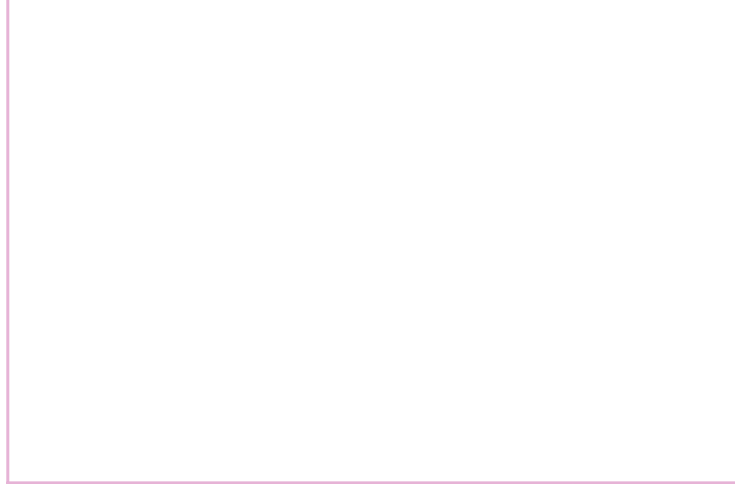
Analyses	Cycle	L/D	Potential (vs Li$^+$/Li) [V]	Scan rate [mVs^{-1}]	AM loading [mg/cm^2]
Activation cycles (DC)	1 - 4	L&D	2.00 - 0.002	-	0.15 (50 wt% AM)
Extended cycles	1 - 200	L&D	2.00 - 0.002	-	0.15 (50 wt% AM)
CV	1 - 4	L&D	2.00 - 0.002	0.10	0.74
CV	1 - 4	L&D	2.00 - 0.002	0.05	0.76
XPS	1	L	1.1	-	0.60
XPS	1	L	0.5	-	0.73
XPS	1	L	0.2	-	0.65
XPS	1	L	0.002	-	0.70
XPS	1	D	0.2	-	0.70
XPS	1	D	0.5	-	0.63
XPS	1	D	1.1	-	0.75
XPS	2	L	0.25	-	0.78
XPS	2	L	0.15	-	0.71
XPS	2	L	0.04	-	0.66
XPS	2	L	0.002	-	0.57
XPS	4	D	2.00	-	0.64

A.2   XPS survey scan redo

Fig. A.1 compares samples stopped during the first lithiation at 0.2 V and 0.002 V with a redo. The survey scan data comes from 0 and 90 seconds etching. Both cells stopped at 0.2 V have a very similar atomic percentage at 0 and 90 seconds etching. This means the composition is likely to be correct. When comparing the two samples stopped at 0.002 V, it is a notable variation in the concentration of the different elements. The carbon amount in the redo sample is 8 % (Etch 0) and ∼7% (Etch 90) lower compared to the first sample. The oxygen amount is much higher for the redo sample, where it has almost the same amount as in the 0.2 V sample. Additionally, the redo sample contains > 6% of lithium compared to the initial sample.
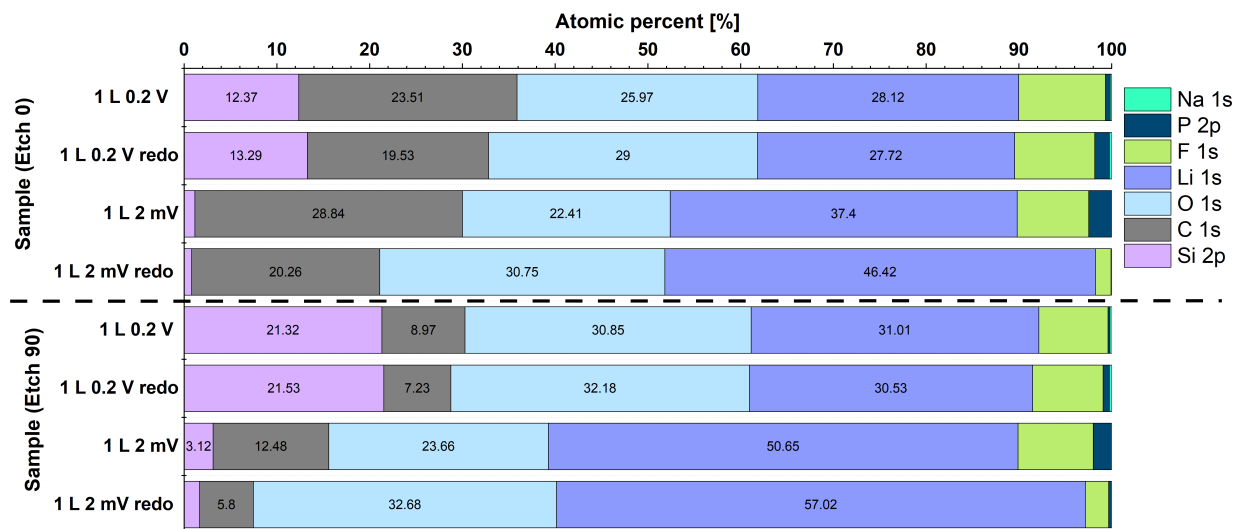
Figure A.1: XPS survey scan plot comparing first lithiation at 0.2 V and 0.002 V with a redo sample at corresponding 0 and 90 seconds etching.